Analysis of Line-Source-Fed Single-Layer Microstrip Reflectarrays

by

Kin Yip Sze

Department of Electrical and Computer Engineering
The University of Manitoba
Winnipeg, Canada R3T 5V6

MAY 2001

A Thesis Submitted to
the Faculty of Graduate Studies of the University of Manitoba
in Partial Fulfillment of the Requirement for the Degree of
Doctor of Philosophy in Electrical Engineering

THE UNIVERSITY OF MANITOBA

FACULTY OF GRADUATE STUDIES

*****

COPYRIGHT PERMISSION

ANALYSIS OF LINE-SOURCE-FED SINGLE-LAYER MICROSTRIP REFLECTARRAYS

BY

KIN YIP SZE

A Thesis/Practicum submitted to the Faculty of Graduate Studies of The University of Manitoba in partial fulfillment of the requirement of the degree

of

DOCTOR OF PHILOSOPHY

To Trisha with Love, and
to My Loving Father & Mother:

When I consider your heavens,
the work of your fingers,
the moon and the stars,
which you have set in place,
what is man that you are mindful of him,
the son of man that you care for him?

-- **Psalm** 8:3,4 (NIV)

EDUCATION & PROFESSIONAL AFFILIATIONS

- M.S.E.E. , December 1991 (The Ohio State University, USA)
- B.S.E.E. (cum laude) , May 1989 (The University of Missouri-Rolla, USA)
- E.I.T. (Province of Manitoba, Canada)
- I.E.E.E. Student Member

ABSTRACT

The analysis of scattering from an infinite periodic array of microstrip patches is used to study line-source-fed single-layer microstrip reflectarrays. An application of these reflectarrays is in high-gain conformal antennas.

Employing rectangular patch geometries in the modelling, reflection phase properties of the reflectarrays are rigorously investigated. Effect of important parameters, such as, patch dimension, substrate permittivity and thickness, are examined. Included in the study is the effect of unattainable reflection phase on phase correction errors and far-field radiation characteristics. A formulation based on phased array and aperture theories is derived for the far-field analysis.

For the analysis of an infinite periodic array of single-layer rectangular microstrip patches, an empirical expression is formulated for approximating the TE-to-z reflection coefficient phase with the incident angle. Also, for computing individual reflectarray far-field terms, simple symmetry formulations are presented.

In addition, multiple patch geometries for the reflectarray are examined. A new hat-shaped patch geometry is introduced in combination with rectangular patch array, for enhanced performance. Far-field radiation characteristics, using tapered distribution schemes for line-source excitations, are compared with those of the uniform distribution. Subsequently, an offset-fed reflectarray is also proposed.

Table of Contents

Acknowledgements

I wish to express my sincere appreciation to my advisor, Prof. Lot Shafai, for his unfailing guidance and insights throughout this research. I also wish to express my sincere thanks to Profs. A. Sebak, Greg Bridges, P. N. Shivakumar (Department of Mathematics) and Ronald Johnston (Department of Electrical and Computer Engineering, University of Calgary) for serving on my thesis committee. Special thanks also go to all my talented colleagues in the department for their helping hands and expertise throughout this research. Indeed, the past is a learning experience and an asset for the future.

Finally, I wish to extend my gratitude to the National Science and Engineering Council of Canada (NSERC) for supporting this research, and to the Faculty of Graduate Studies, Department of Electrical and Computer Engineering, Graduate Student Association and Alumni Association, for their many travel awards which were crucial to funding my conference travels, both within Canada and abroad.

List of Figures

List of Tables

1 Introduction

Planar periodic arrays of conducting patches have many applications, because of their varying reflection and transmission properties with frequency [1]. They are used as frequency-selective surfaces (FSS), also known as dichroic surfaces. They are also utilized extensively as filters in microwave and optical technologies [2][3], dichroic subreflectors in multifrequency antenna systems [4], polarization gratings and diplexers [3][5]. Their analysis techniques are also employed in the design and investigation of microstrip reflectarrays.

1.1 MICROSTRIP REFLECTARRAY

According to Berry *et. al.*, a reflectarray incorporates many desirable features of reflector antennas and planar arrays [6]. Instead of a corporate feed line, a feed antenna is used to illuminate its conducting patch elements, which are designed to scatter the incident field with an appropriate phase necessary to form a co-phasal aperture plane in front of the reflectarray. Thus, through this spatial feeding scheme, losses attributed to the array feed network are avoided. Recently, a similar spatial feeding technique is also employed in spatial power combiners [3].

A common implementation of the reflectarray is in the form of microstrip antenna array, thus, the term *microstrip reflectarray*. A photograph of a microstrip reflectarray is depicted in Fig. 1-1.

Microstrip reflectarrays are alternatives to the more traditional parabolic reflector antennas in certain applications because of their unique properties. In particular, these reflectarrays are aesthethically pleasing in appearance, lightweight and compact, and have good efficiencies and high gains [7].

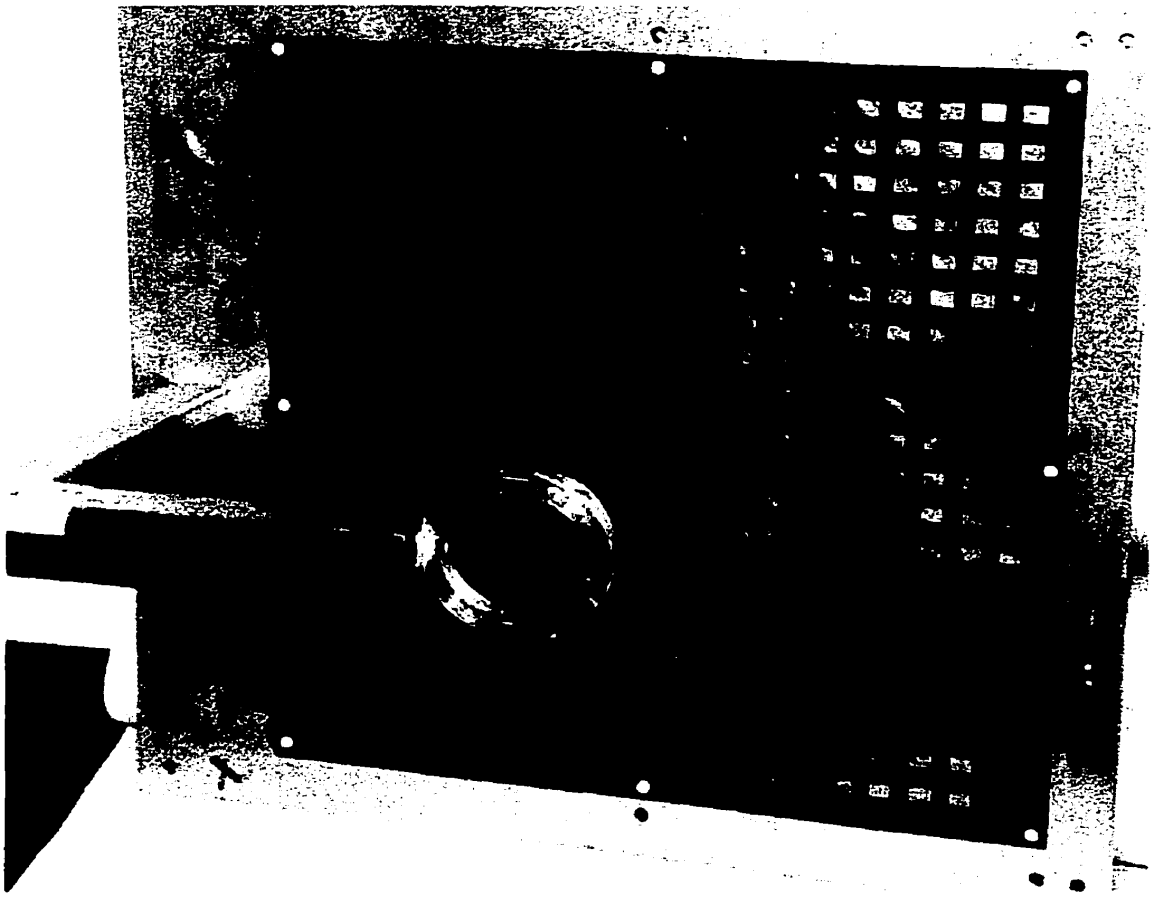

Fig. 1-1: A microstrip reflectarray without the feed antenna. *(Courtesy of C. B. Ravipati, D. Gray and L. Shafai, The University of Manitoba, Canada.)*

Several variations of microstrip reflectarrays have been designed and fabricated. It is believed that each of these different types of reflectarrays has its own merits over the others.

Among the most common ones are the variable-stub-length reflectarrays [8]-[10], the variable-patch-size reflectarrays [7] and the variably-rotated-patch reflectarrays [11]. These designs utilize prudent variations of geometrical parameters of individual array elements for focussing the beam.

Other classes of microstrip reflectarrays also exist. Namely, those that employ a lattice variation [12]-[16], and those that combine both element geometry and lattice variations [17], to achieve the same purpose.

1.2 REFLECTARRAY DEVELOPMENTS

The reflectarray is an old technology that dates back to early 1960s [6][7]. It is only in recent years, with the advent of inexpensive, faster and larger-memory computers, low-cost but highly efficiency software tools, and improved microstrip fabrication techniques, that this antenna technology has gained renewed interests in both terrestrial and space-borne telecommunications systems. Generally, the analysis and design of a microstrip reflectarray requires intense numerical computations before it is fabricated and constructed.

This section presents a brief overview of the historical developments of the microstrip reflectarray and its projected future directions. Also, since an infinite array approach will be utilized extensively in this thesis, for the analysis and design of line-source-fed single-layer microstrip reflectarrays, a short introduction to the concept of infinite periodic array of conducting patches is presented.

1.2.1 Early Developments

The idea of reflectarray was first introduced by Malech in 1962 [7], and its comprehensive description was published by Berry *et. al.* a year later [6]. It utilizes a periodic array of elementary antennas (i.e. elementary antennas configured into a periodic lattice) as the reflecting surface, and was experimentally demonstrated using periodic arrays of rectangular waveguides.

The reflectarray concept was introduced for performing beam scanning, similar to that of a phased array, but without the complexities (such as high fabrication costs, bulkiness and massiveness) and losses of its feed network. A space feeding scheme using a feed antenna for illuminating the reflecting surface was employed in an offset-fed configuration.

In 1978, Malagisi introduced a microstrip implementation of the reflectarray [18], and was patented by Munson *et. al.* in 1987 [19]. In this design, the planar reflecting surface is comprised of an array of microstrip patches, loaded with stubs of varying lengths for adjusting the reflection phase. Presently, this is one of the reflectarray designs that is being investigated and improved by antenna researchers.

Another reflectarray design was conceived by Phelan in 1977 [20]. In this case, large discrete spiral elements, with limited switchable positions, were introduced to control the reflection phase of circularly polarized waves.

1.2.2 Next Generation Reflectarrays

Presently, the term "reflectarray" is commonly referred to as planar reflectors. These antennas can be categorized into periodic arrays or as quasi-periodic arrays. Quasi-periodic arrays are comprised of blazed grating reflectors (which produce higher-order diffraction modes) and Fresnel zone plate planar reflectors. Periodic planar reflectors, on the other hand, are reflectarrays which have varying element geometries arranged in periodic lattices. These elements are either stub-loaded patches, or dipoles and rectangular (or square) patches.

In addition, these next generation reflectarrays may be constructed with single-layered, or stacked-layered elements, and as single-piece, or dual-piece, reflectors. The following sections describe some of these planar reflectors.

1.2.3 Variable-Stub-Length Reflectarrays

Analyses of microstrip reflectarrays that employ variable-stub-length patch elements for reflection phase corrections were first published in the open literature by Huang [22] and Metzler [21]. Subsequently, Chang and Huang reported the first microstrip reflectarray

fabricated using variable-stub-length patch elements, and verified their design through measurements [8].

An infinite periodic array modelling technique was employed by Metzler in his analysis and design of a microstrip reflectarray operating at *5*GHz, which was verified experimentally [21]. In his design, microstrip patch elements are printed in a triangular lattice array, and each patch element is attached a straight stub. These stubbed patches were also employed by Zhuang *et. al.* in a 25-element microstrip reflectarray [23], and in co-linear arrays of indented patches [24], and subsequently, by Javor *et. al.* in a 4×3-element microstrip reflectarray for linear-phased, dual-polarized beam, with added beam-switching capabilities [25].

A microstrip reflectarray with *1656* patch elements consisting of both straight and *90°* bent stubs in rectangular lattice array was designed by Chang and Huang for dual-linear and dual-circular polarization capability in the X-band, but experimentally demonstrated only the linear polarization case [9]. Cross-polarization analysis was also performed in this study, which indicated minimal cross-polarization levels.

1.2.4 Variable-Patch-Size Reflectarray

Another common type of reflectarray is the variable-patch-size microstrip reflectarray. Microstrip crossed-dipoles are the earliest microstrip elements without stubs to be employed as a reflecting patch array in a microstrip reflectarray, and this was patented and

fabricated by Malibu Research Associates [26]. This design utilized varying dipole lengths for reflection phase control, instead of varying stub lengths. Subsequently, Pozar and Metzler presented the first analysis of a variable-patch-length microstrip reflectarray and demonstrated that it performs better than a variable-stub-length patch array [27].

The microstrip reflectarray using variable-patch-length elements was first fabricated and tested at *5*GHz by Targonski and Pozar [28]. Eventually, a full and concise literal discussion on the analysis and design of the variable-patch-length microstrip reflectarray was published by Pozar *et. al.* [7]. Experimental evaluation of four reflectarrays for millimeter-wave applications was also discussed in [7].

More recently, crossed-dipoles microstrip reflectarrays were proposed by Pozar and Targonski for overlaying onto the solar panel of space vehicles, and performances of crossed-dipoles and square patches were compared [29].

1.2.5 Movable and Rotated Element Reflectarray

Position switchable spiral elements were introduced in a reflectarray by Phelan in 1977 [20]. A decade later, a similar idea by Cooley *et. al.* emerged in the form of a reflectarray with movable dielectric rods to vary th effective dielectric constant of the substrate [30]. This design was demonstrated through the use of an array waveguide simulator.

In recent years, Huang and Pogorzelski published their work on a Ka-band microstrip reflectarray with *6924* variably-rotated patch elements [11][31][32]. This is the first pub-

licized circularly-polarized microstrip reflectarray to be fabricated and tested. In this design, circularly-polarized microstrip elements were rotated to varying angles to achieve phase collimation.

1.2.6 Stacked Element Reflectarrays

Due to inherent narrowband characteristics of microstrip reflectarrays, and the high demand for dual-frequency antennas, stacked element configurations with dual-frequency capabilities were proposed [33][34]. Wu *et. al.* presented numerically simulated results of doubly-stacked arrays of variable-stub-length patches, in which mutual coupling between stacked layers were not included in the simulations, but had acknowledged its importance in design considerations [33]. Encinar, on the other hand, numerically simulated doubly-stacked arrays of variable-patch-length patches for a reflectarray using the generalized scattering matrix (GSM) formulations for multilayer periodic structures [34]. The offset-fed reflectarray configuration was employed in this design.

1.2.7 Blazed Gratings and Fresnel Zone Plate Planar Reflectors

These reflectors are generally categorized as quasi-periodic planar reflectors due to their quasi-periodic array lattices utilized as the reflecting surface. Rigorous analyses and design work on blazed gratings (also known as frequency-scanned gratings) planar reflectors were performed by Johansson a decade ago [12]-[15]. A quasi-periodic lattice variation was utilized to achieve blazed reflection, whereby a first higher-order diffraction mode was excited. Microstrip dipoles and annular rings were employed as element grat-

ings in the design. An aperture efficiency of *56%* was achieved for the dipole grating reflector.

A feasibility study was performed by Baruch and Leviatan using line-source illuminated, quasi-periodic, finite echelette gratings [35]. Beam steering through frequency scanning, and radiation sensitivity to grating fabrication errors and improper feed location, were analyzed numerically. Further work is necessary for practical implementation of this design.

Guo and Barton designed and fabricated a Fresnel zone plate planar reflector, which attained phase collimation using circular arrays of conducting ring elements of varied sizes and element spacings [17]. A measured efficiency of only *43%* was reported for this reflector.

1.2.8 Dual-Planar Reflectors

The earliest dual-planar reflector construction was reported by Pozar *et. al.* in 1997, which was in the form of a *77*GHz Cassegrain microstrip reflectarray [7]. A small hyperboloid subreflector was utilized in this design.

Subsequently, a folded reflectarray was fabricated by Pilz and Menzel, and Menzel *et. al.*, for operation at *20*GHz [36]-[38]. In this design, a planar polarizing grid was employed as a subreflector, and a microstrip twist reflector was used as the main reflector.

Yet another type of dual-planar reflector was introduced by Shaker and Cuhaci [16]. It was constructed using two blazed grating planar reflectors, and the concept of beam squint cancellation was employed in an attempt to decrease the frequency-dependent beam squint [39][40] problem.

1.3 MICROSTRIP REFLECTARRAY ANALYSIS TECHNIQUES

As there has been much research on microstrip reflectarrays, various analysis and design techniques have been introduced. The following sections describe several of the most popular techniques.

1.3.1 Waveguide Simulator Technique

Through this technique, the microstrip reflectarray is experimentally simulated and designed [21][30]. Here, the simulator is used to measure the plane wave reflection coefficient of large periodic arrays, which is accomplished by imaging a test element onto the walls of the waveguide simulator. This requires that the test element be symmetrical along the x- and y- axes. In order to simulate periodic arrays with non-symmetric elements, an alternate symmetric element is employed, an example of which is discussed in [21]. However, this experimental technique is accurate only for weak mutual coupling on the reflectarray [30].

1.3.2 Finite Array Approach

A computationally simple technique, the finite array approach, was first discussed by Huang in his microstrip reflectarray analysis [22]. This technique is based on the Fraunhofer aperture field integration on the projected aperture plane of the reflectarray, and was also utilized by Chang and Huang [9]. In this formulation, mutual coupling is assumed to be negligible, and full-wave scattering effects, such as the existence of other propagating modes, are ignored. This modelling approach is well-suited for variably-rotated microstrip reflectarray analyses and designs [11].

1.3.3 Infinite Array Approach

This is an infinite periodic array technique for the design of a microstrip reflectarray, which was first presented by Metzler [21]. In this technique, the unknown current distribution on a single conducting element in the array is first obtained. This requires rigorous computation effort as compared to the simpler finite array approach discussed in [8]-[11] [22][31][32][41][42]. From the current coefficients obtained, the reflection phase and the scattered fields of the reflectarray are then approximated. Mutual coupling between array elements is accounted for through Floquet modal formulations [43].

A similar infinite periodic array approach was employed by Johansson in his analysis and design of quasi-periodic planar reflectors, but with additional formulations included for first-order diffracted fields [12]-[15]. For multilayered microstrip reflectarray, on the other

hand, the generalized scattering matrix for analyzing periodic structures may be utilized, as proposed by Encinar [34].

Furthermore, a Conjugate-Gradient - Fast-Fourier-Transform (CG-FFT) method for infinite periodic array analysis was employed in the analysis of a stubbed microstrip patch reflectarray by Zhuang *et. al.* [23][24]. This method enables a more efficient computation of stubbed patch arrays.

1.4 INFINITE PERIODIC ARRAY OF CONDUCTING PATCHES

Conducting patch elements, or aperture elements on a conducting screen, can be arranged such that they are periodic in two planar directions. These structures, generally known as doubly periodic gratings, or simply, bigratings [44], possess frequency-selective surface (FSS) properties. Some grating geometries may also possess circular-polarization-selective surface (CPSS) properties [45]-[47].

1.4.1 Single-layer Analysis Techniques

In the case of a single-layer infinite periodic patch arrays, numerous methods have been proposed for analyzing its characteristics. Ott *et.al.* [48] utilized an electric field integral equation (EFIE) approach and enforced the point-matching method for solving them. Chen and Montgomery proposed a periodic modal analysis approach in which current densities are represented as orthogonal mode functions and mode-matching them appropriately [49][50]. It is recently used successfully in designing frequency-scanned planar

reflectors by Johansson [12]-[15]. The periodic spectral domain Green's function approach has also been introduced [51]-[56], and its convergence accelerated using Ewald's and lattice-sum methods [57][58].

1.4.2 Analysis Techniques for Complex Geometries

In attempts to overcome difficulties in handling complex periodic array geometries, the Finite-Difference Time-Domain (FDTD) method using Floquet boundary conditions has been employed [59]-[62]. The hybrid finite-element - boundary-integral (FE-BI) techniques are also implemented [63]-[68]. Additional progress were achieved by Reed and Byrne on a modal analysis of multiple apertures within a periodic cell [69], which was further extended by Bozzi and Perregrini recently, for multiple arbitrary planar patch geometries using the Boundary Integral - Resonant Mode Expansion (BI-RME) method [70][71].

1.4.3 Multilayer Structures

Several of the single-layer periodic structures may be cascaded together to form a multilayer periodic structure, which has modified reflective and angular properties [72]. However, for an accurate predictions of these properties, the mutual coupling between the layers must be accounted for in the formulations [72]. The analysis thus becomes more complex. Furthermore, a multilayer structure may be too thick and bulky for certain applications where space and weight are limited.

1.5 RESEARCH MOTIVATIONS, OBJECTIVE AND APPROACH

Among many advantages of microstrip reflectarrays, there are also some serious performance shortcomings that still need to be improved, particularly the issue of limited bandwidth [7][10][41].

1.5.1 Research Motivations

The restricted bandwidth of a microstrip reflectarray is largely attributed to:

(i) the narrow bandwidth of the patch elements and feed,

(ii) the improper design of the frequency dependent lattice geometry of the array,

(iii) the differential spatial phase delay due to an extended path length between the feed and reflectarray [10][41], and

(iv) the inherent phase errors produced as a result of the changes in the patch dimensions which are required to collimate the beam [7].

Furthermore, such restrictions on bandwidth can contribute to the effects of undesired beam squinting [40][72] in offset-fed configurations.

Typically for a single-layer rectangular microstrip patch reflectarray, the reflection coefficient phase is relatively constant for both short and long patch lengths. However, it is highly sensitive to the patch length variation at near resonant lengths, creating a relatively narrow bandwidth for patch lengths in this region [7]. This is especially so, if the incident angle of the incoming beam is relatively large.

In order to improve the bandwidth of these reflectarrays, multilayer microstrip patches are introduced [34][73]. But, multilayer configurations are costly and generally impractical, due to surface wave effects, at millimeter-wave frequencies such as the Ka-bands. With single-layer microstrip reflectarrays, thick substrates are utilized for bandwidth enhancements [7][74]. A thick substrate, however, has a large unattainable reflection phase range [7], which requires further investigations to understand its dependence on the substrate parameters and patch geometries. Surface wave losses can also be excessive in these substrates, which prefer the use of low permittivity foam type substrates.

1.5.2 Research Objective

The primary objective of this research is to investigate the performance of a new line-source-fed single-layer microstrip reflectarray through numerical modelling, and also, to simplify the analysis and design procedures. To achieve this, parameters that govern the performance of the line-source-fed microstrip reflectarray are rigorously examined, and the physical design constraints of the reflectarray explicitly identified.

1.5.3 Research Outline and Approach

The infinite periodic array theory is utilized as a modelling tool [7] [27]-[29] in this study, which would be addressed in Chapter 2. The analysis of an infinite periodic patch array is based on a modal formulation involving the Floquet's theorem [50]. The electric field integral equation (EFIE) based on the Floquet modal formulations, for scattering by an infinite periodic array of thin conductors on a dielectric sheet, is first derived.

Upon enforcing the proper boundary conditions, an eigenvalue equation is then obtained through the Galerkin's method of moment (MoM), where either the entire-domain sinusoidal or subdomain roof-top basis function expansion is employed. Subsequently, the unknown coefficients are determined numerically through solving a linear matrix equation.

Since commercial softwares capable of such simulations are unavailable, customized softwares are built in-house. Very intensive computer programming is therefore performed for approximately 80% of the entire work. The complex computer code was built entirely by the author in the interval of *15* months, and computing resources were spent on producing an accurate, functioning code known as *ARCOF*, from which the infinite periodic array analysis results were eventually published [75]-[78].

Subsequently, a comprehensive postprocessing code, *EFEL*, was developed to post-process data generated by *ARCOF*. Extensive time, in the interval of *10* months, were again taken to develop and debug this postprocessor. Consequently, excellent results were obtained through repeated simulations using these codes for the reflectarray studies, which were also published [79]-[86].

The software package consists of *ARCOF*, a code for the infinite periodic array analysis, and *EFEL*, a code to post-process data generated by *ARCOF*. Further details of this software package are presented in Appendix B.

1.5.4 Chapter Descriptions

The following outlines the objectives and content of each subsequent chapters in this thesis:

- Chapter 2: *Infinite Periodic Patch Arrays*

  This chapter describes the theory of infinite periodic patch arrays, based on the EFIE Floquet modal formulations proposed by Montgomery [50], and the investigation of their numerical convergences. Both entire-domain sinusoidal and subdomain roof-top basis functions are examined and compared.

- Chapter 3: *Single-Layer Analysis*

  This chapter analyzes the reflection properties of a single-layer microstrip patch array and its effects on the array far-field radiation performance. For a center-fed reflectarray configuration, two discriminatively different substrates are utilized, namely, a thin $\varepsilon_r = 2.5$ substrate and a thick foam ($\varepsilon_r = 1.03$) substrate.

- Chapter 4: *Some Essential Design Concepts.*

  As an extension to concepts discussed in Chapter 3. Further line-source-fed microstrip reflectarray concepts are presented in this chapter. Center-fed configurations are utilized for this discussion.

- Chapter 5: *Offset-Fed Configuration*

  In this chapter, an offset-fed configuration is proposed and evaluated, to enhance the far-field radiation performance of a line-source-fed microstrip reflectarray. Also, properties unique to this configuration are compared to

that of the center-fed configuration of Chapter 3 and Chapter 4, and its line-source distribution effects investigated.

- Chapter 6: *Summary and Future Research*

  A summary of this thesis is provided in this chapter, which includes a proposal for future research.

2 Infinite Periodic Patch Array

To gain an insight into the scattering characteristics of an infinite periodic array of rectangular, perfectly conducting patches, an analysis on the scattering properties of the infinite periodic array is performed. The analysis is based on modal formulations involving the Floquet's Theorem.

The analysis is applied through numerical computations in which only the aspect ratios of the patches are varied. Consequently, the effect of changing aspect ratios are then studied. The reflection properties considered in these computations are the variations of reflection coefficients with respect to parameters such as frequencies, TE-to-z incident angles, number of basis functions and number of the Floquet mode terms.

This study also serves to verify the accuracy and robustness of the computer code *ARCOF* developed for microstrip reflectarray simulations. A brief description of this code is presented in Appendix B.

2.1 Floquet Modal Formulations

In this analysis, the modal formulations involving the Floquet's Theorem [50] are utilized. Fig. 2-1 illustrates the schematic of an array of arbitrarily shaped patches attached to the

surface of a dielectric sheet of permittivity ε_d. Each of these patches are assumed to be identical. Furthermore, they are infinitely thin and perfectly conducting. All media, except for the patch elements, are isotropic, homogeneous dielectric materials with zero-conductivity.

In this analysis, a plane wave is taken as the incident wave. As such, the infinite array of conducting patches will be excited uniformly. By exploiting the periodicity of the array, only a single periodic cell has to be analyzed [43]. Such an evaluation is carried out through the application of the Floquet's Theorem, whereby the mutual coupling effects between individual elements are automatically accounted for [43]. The analysis presented here is based upon that proposed in [50]. Throughout this thesis, the time dependence $e^{j\omega t}$ is assumed.

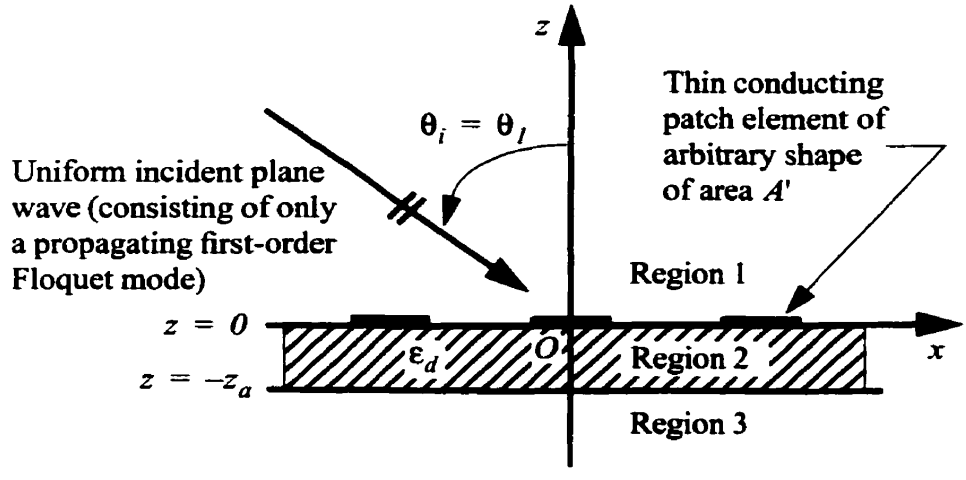

Fig. 2-1: Cross section of an infinite periodic patch array. All media, except for the patch elements, are isotropic, homogeneous dielectric materials with zero-conductivity.

2.1.1 Boundary Conditions

The incident plane wave can be assumed to consist of only the propagating first Floquet mode. Thus, in the absence of the conducting patches, but in the presence of the dielectric sheet, the field equations in different regions can be obtained as described in [50]. That is, with the subscript T denoting the transverse component, m being the index for the transverse modes ($m = 1, 2$ relates to the TM-to-z and TE-to-z modes, respectively) and 00 representing the first-order (00-th) Floquet mode, the total $\vec{E}$ and $\vec{H}$ fields in region 1 (for $z \geq 0$) due to the dielectric sheet alone are given as

$$\vec{E}_T^{(d)}(\vec{r}) = \vec{E}_T^{(i)}(\vec{r}) + \vec{E}_T^{(r)}(\vec{r}) = \sum_m \left\{ B_m^{(i)} \left(e^{j\Gamma_{00}^{(1)} z} + R_{m00}^{(2)} e^{-j\Gamma_{00}^{(1)} z} \right) e^{-j\vec{k}_{T00}^{(1)} \cdot \vec{r}_T} \hat{\kappa}_{m00}^{(1)} \right\} \quad (2\text{-}1)$$

and

$$\begin{aligned} \vec{H}_T^{(d)}(\vec{r}) &= \vec{H}_T^{(i)}(\vec{r}) + \vec{H}_T^{(r)}(\vec{r}) \\ &= \sum_m \left\{ B_m^{(i)} \zeta_{m00}^{(1)} \left(-e^{j\Gamma_{00}^{(1)} z} + R_{m00}^{(2)} e^{-j\Gamma_{00}^{(1)} z} \right) e^{-j\vec{k}_{T00}^{(1)} \cdot \vec{r}_T} \hat{z} \times \hat{\kappa}_{m00}^{(1)} \right\}, \end{aligned} \quad (2\text{-}2)$$

respectively. Here, $R_{m00}^{(2)}$ is the first-order (00-th) Floquet modal, or specular, reflection coefficient due to a dielectric sheet of thickness z_a at boundary $z = 0$. The amplitude of the incident plane wave is denoted by $B_m^{(i)}$, the Floquet modal admittance for region 1 by $\zeta_{m00}^{(1)}$, the transverse Floquet modal propagation vector and unit vector in region 1 by $\vec{k}_{T00}^{(1)}$ and $\hat{\kappa}_{m00}^{(1)}$, respectively, and the z-component of the Floquet modal propagation con-

stant in region 1 by $\Gamma_{00}^{(1)}$. Detailed expressions of these parameters are provided in Appendix A, Section A.1. However, in the presence of the conducting patches only, the fields due to the currents on these patches at $z = 0$ can be expressed as [50]:

In region 1 for $z \geq 0$,

$$\vec{E}_T^{(1)}(\vec{r}) = \sum_{mpq} \left\{ A_{mpq}^{(1)} e^{-j\Gamma_{pq}^{(1)} z} e^{-j\vec{k}_{Tpq}^{(1)} \cdot \vec{r}_T} \hat{\kappa}_{mpq}^{(1)} \right\} \tag{2-3a}$$

$$\vec{H}_T^{(1)}(\vec{r}) = -\sum_{mpq} \left\{ A_{mpq}^{(1)} \zeta_{mpq}^{(1)} e^{-j\Gamma_{pq}^{(1)} z} e^{-j\vec{k}_{Tpq}^{(1)} \cdot \vec{r}_T} \hat{z} \times \hat{\kappa}_{mpq}^{(1)} \right\}. \tag{2-3b}$$

In region 2 for $-z_a \leq z \leq 0$,

$$\vec{E}_T^{(2)}(\vec{r}) = \sum_{mpq} \left\{ \left(B_{mpq}^{(2)} e^{j\Gamma_{pq}^{(2)} z} + A_{mpq}^{(2)} e^{-j\Gamma_{pq}^{(2)} z} \right) e^{-j\vec{k}_{Tpq}^{(2)} \cdot \vec{r}_T} \hat{\kappa}_{mpq}^{(2)} \right\} \tag{2-4a}$$

$$\vec{H}_T^{(2)}(\vec{r}) = \sum_{mpq} \left\{ \zeta_{mpq}^{(2)} \left(-B_{mpq}^{(2)} e^{j\Gamma_{pq}^{(2)} z} + A_{mpq}^{(2)} e^{-j\Gamma_{pq}^{(2)} z} \right) e^{-j\vec{k}_{Tpq}^{(2)} \cdot \vec{r}_T} \hat{z} \times \hat{\kappa}_{mpq}^{(2)} \right\}. \tag{2-4b}$$

In region 3 for $z \leq -z_a$,

$$\vec{E}_T^{(3)}(\vec{r}) = \sum_{mpq} \left\{ B_{mpq}^{(3)} e^{j\Gamma_{pq}^{(3)} z} e^{-j\vec{k}_{Tpq}^{(3)} \cdot \vec{r}_T} \hat{\kappa}_{mpq}^{(3)} \right\} \tag{2-5a}$$

$$\vec{H}_T^{(3)}(\vec{r}) = -\sum_{mpq} \left\{ B_{mpq}^{(3)} \zeta_{mpq}^{(3)} e^{j\Gamma_{pq}^{(3)} z} e^{-j\vec{k}_{Tpq}^{(3)} \cdot \vec{r}_T} \hat{z} \times \hat{\kappa}_{mpq}^{(3)} \right\}. \tag{2-5b}$$

$A_{mpq}^{(\cdot)}$ and $B_{mpq}^{(\cdot)}$ are complex coefficients dependent on the currents $\vec{J}_s(\vec{\rho}'_T)$ on the conducting patches. With these fields defined, there are a total of four boundary conditions associated with this problem. These boundary conditions provide the following relationships:

(a) For fields attributed to the currents on the conducting patches at $z = 0$, we have:

i. At $z = -z_a$, a partial reflection occurs in region 2. This is given as the continuity of tangential $\vec{E}$ in regions 2 and 3, that is,

$$\vec{E}_T^{(2)}(\vec{\rho})\big|_{z=-z_a} = \vec{E}_T^{(3)}(\vec{\rho})\big|_{z=-z_a}; \vec{\rho} = \vec{\rho}_T. \tag{2-6}$$

ii. At $z = 0$, the continuity of tangential $\vec{E}$ in regions 1 and 2 exits outside the perfectly conducting patches, and this provides

$$\vec{E}_T^{(1)}(\vec{\rho})\big|_{z=0} = \vec{E}_T^{(2)}(\vec{\rho})\big|_{z=0} \; ; \vec{\rho} = \vec{\rho}_T \notin A'. \tag{2-7}$$

iii. At $z = 0$, on the perfectly conducting patches, namely on $\vec{\rho} = \vec{\rho}_T \in A'$, there is continuity of tangential $\vec{H}$ between regions 1 and 2. An expression for the induced current on the patches is

$$\hat{z} \times \left[\vec{H}_T^{(1)}(\vec{\rho})\big|_{z=0} - \vec{H}_T^{(2)}(\vec{\rho})\big|_{z=0} \right] = \vec{J}_s(\vec{\rho}_T); \quad \vec{\rho} = \vec{\rho}_T \in A'. \tag{2-8}$$

(b) For fields attributed to the interaction of an incident plane wave on the dielectric sheet, and as well as, to fields due to the currents on the conducting patches at $z = 0$, we observe that the tangential $\vec{E}$ vanishes on the perfectly conducting patches, i.e. where $\vec{\rho} = \vec{\rho}_T \in A'$, and gives

$$\vec{E}_T^{(d)}(\vec{\rho})|_{z=0} + \vec{E}_T^{(I)}(\vec{\rho})|_{z=0} = \vec{0}. \tag{2-9}$$

From the boundary conditions (2-6) through (2-9), and ensuing from some extensive algebraic manipulations, the Floquet modal form of the electric field integral equation (EFIE) is obtained for the scattering by an infinite periodic array of thin conductors on an infinite dielectric sheet as

$$\sum_m \left\{ B_m^{(i)} (1 + R_{m00}^{(2)}) e^{-j\vec{k}_{T00}^{(I)} \cdot \vec{\rho}_T} \hat{\kappa}_{m00}^{(I)} \right\}$$
$$= \frac{1}{A} \sum_{mpq} \left\{ \frac{e^{-j\vec{k}_{Tpq}^{(I)} \cdot \vec{\rho}_T}}{\zeta_{mpq}^{(eq)}} \left[\hat{\kappa}_{mpq}^{(I)} \cdot \int_{A'} e^{j\vec{k}_{Tpq}^{(I)} \cdot \vec{\rho}'_T} \vec{J}_s(\vec{\rho}'_T) dr'_T \right] \hat{\kappa}_{mpq}^{(I)} \right\}, \tag{2-10a}$$

where

$$\zeta_{mpq}^{(eq)} = \zeta_{mpq}^{(I)} + \zeta_{mpq}^{(2)} \left(\frac{1 - R_{mpq}^{(3)}}{1 + R_{mpq}^{(3)}} \right), \tag{2-10b}$$

and

$$A_{mpq}^{(I)} = -\frac{1}{A \zeta_{mpq}^{(eq)}} \left[\hat{\kappa}_{mpq}^{(I)} \cdot \int_{A'} e^{j\vec{k}_{Tpq}^{(I)} \cdot \vec{\rho}'_T} \vec{J}_s(\vec{\rho}'_T) dr'_T \right], \tag{2-11}$$

with $R^{(3)}_{mpq}$ being the Floquet modal reflection coefficient in region 2 due to the boundary at $z = -z_a$, $\zeta^{(l)}_{mpq}$ being the Floquet modal admittance for region l, A being the cell area and A' being the patch area. The complete expressions for these parameters are also appended in Appendix A, Section A.1.

2.1.2 Solution with Entire-Domain Basis Function Expansion

To solve (2-10a), the unknown current density $\vec{J}_s(\vec{r}'_T)$ is expanded using the entire-domain basis functions as

$$\vec{J}_s(\vec{r}_T) = \sum_{m'n'} \{c_{m'n'} \vec{h}_{m'n'}(\vec{r}_T)\}, \tag{2-12}$$

where $\vec{h}_{m'n'}(\vec{r}_T)$ are entire-domain modal basis vectors and $c_{m'n'}$ are their unknown modal coefficients. These parameters are defined in Appendix A, Section A.2. In order to numerically solve for $c_{m'n'}$, the Galerkin's Method of Moment [87] is employed. By substituting (2-12) into (2-10a) and rewriting, an eigenvalue equation is obtained as

$$\vec{\Upsilon}^{(l)}_{f'g'00}{}^{*}(\vec{r}_T) \cdot \sum_{m} \{B^{(i)}_m (1 + R^{(2)}_{m00}) \hat{\kappa}^{(l)}_{m00}\}$$
$$= \sum_{m'n'} \left\{ \frac{c_{m'n'}}{A} \sum_{mpq} \left\{ \frac{1}{\zeta^{(eq)}_{mpq}} [\hat{\kappa}^{(l)}_{mpq} \cdot \vec{\Upsilon}^{(l)}_{m'n'pq}(\vec{r}_T)][\hat{\kappa}^{(l)}_{mpq} \cdot \vec{\Upsilon}^{(l)}_{f'g'pq}(\vec{r}_T)^{*}] \right\} \right\}, \tag{2-13a}$$

where

$$\vec{\Upsilon}^{(l)}_{m'n'pq}(\vec{r}_T) = \int_{A'} \vec{h}_{m'n'}(\vec{r}_T) e^{j\vec{k}^{(l)}_{Tpq} \cdot \vec{r}_T} dr_T \tag{2-13b}$$

is the orthogonal mode function associated with the current density $\vec{J}_s(\vec{r}'_T)$.

Using the index mapping $n' \rightarrow (n_1,n_2)$, the modal basis vector $\vec{h}_{m'n'}(\vec{r}_T)$ becomes $\vec{h}_{m'n_1n_2}(x, y)$ with the entire-domain basis vectors defined as [49]

$$\vec{h}_{1n_1n_2}(x, y) = F_{n_1n_2}\left[\frac{n_2\pi}{b}h_{n_1n_2x}(x, y)\hat{x} - \frac{n_1\pi}{a}h_{n_1n_2y}(x, y)\hat{y}\right], \text{ for TM mode,} \quad (2\text{-}14a)$$

$$\vec{h}_{2n_1n_2}(x, y) = F_{n_1n_2}\left[\frac{n_1\pi}{a}h_{n_1n_2x}(x, y)\hat{x} + \frac{n_2\pi}{b}h_{n_1n_2y}(x, y)\hat{y}\right], \text{ for TE mode,} \quad (2\text{-}14b)$$

where $h_{n_1n_2x}(x, y)$ and $h_{n_1n_2y}(x, y)$ are the entire-domain sinusoidal basis functions in x- and y- directions, respectively, a and b are the patch dimensions in the x- and y- directions, respectively, and $F_{n_1n_2}$ is the normalization factor for the basis vectors. Detailed expressions of these basis functions and parameters are presented in Appendix A, Section A.2. Utilizing (2-14), the integral equation (2-13b) is evaluated through closed-form integration.

The eigenvalue equation (2-13a) is reduced to a linear matrix equation consisting of a square matrix, in which its size is dependent on the number of modal terms used. This equation is solved for the unknown coefficients $c_{m'n'}$ using the various existing numerical methods available.

Subsequently, for a reference plane $z = z_p$, the first-order (00-th) Floquet modal, or specular, reflection coefficient is obtained as

$$R_{m00}^{(m00)} = \left. \frac{E_{T_{(m00)}}^{(r)} + E_{T_{(m00)}}^{(l)}}{E_{T_{m00}}^{(i)}} \right|_{z = z_p}, \tag{2-15}$$

where $E_{T_{m00}}^{(i)}$ and $E_{T_{(m00)}}^{(r)}$ are first-order (00-th) Floquet modes of the incident and reflected fields in region 1, respectively, and $E_{T_{(m00)}}^{(l)}$ is the first-order (00-th) Floquet mode of the field in region 1 due to currents on the conducting patches.

2.2 INFINITE PERIODIC PATCH ARRAY IN FREE SPACE

Using these derivations, a numerical code *ARCOF* is developed for analyzing the reflection properties of an infinite periodic array of rectangular patches in free space, as illustrated in Fig. 2-2. For this investigation, the relative permittivity of the dielectric sheet is set to unity, and the patches are assumed to be perfectly conducting and infinitely thin.

Assuming a TE-to-z incident plane wave, the analysis is performed by varying only the aspect ratio b/a of the patches so that its effects can be studied. The properties considered in these computations are the variations of reflection coefficient magnitudes for a TE-to-z incident plane wave, denoted as $\left|R_{200}^{(200)}\right|$, with respect to parameters such as the frequencies f, TE incident angles θ, number of basis function terms $n_{l\max}$ (x-directed) and

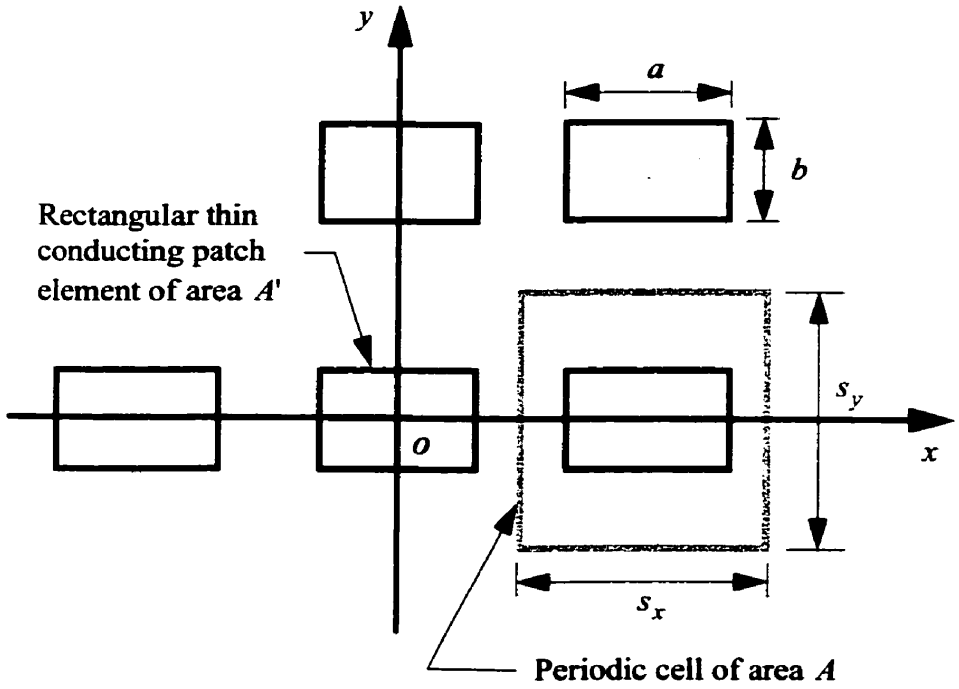

(a)

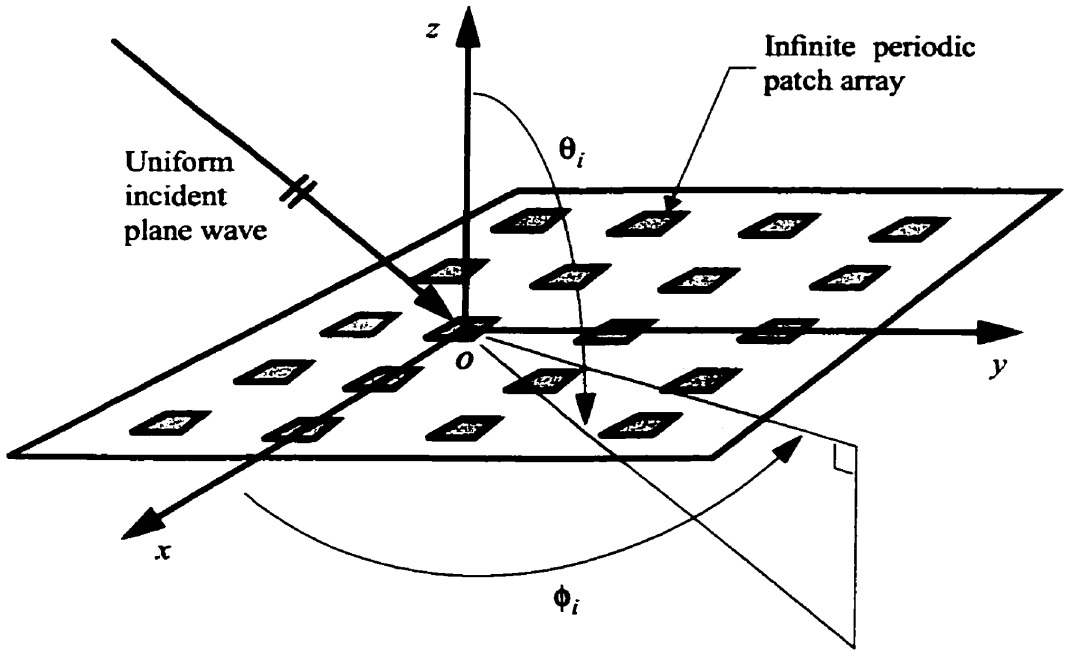

(b)

Fig. 2-2: Schematics of an infinite periodic patch array in free-space: (a) top-view, and (b) coordinate system of a uniform incident plane wave employed in the analysis.

$n_{2\max}$ (y-directed), and number of Floquet mode terms $p_{\max}$ (x-directed) and $q_{\max}$ (y-directed). In order to verify the validity of the numerical code developed in this study, results from Fig. 2 of [49] (which had been verified through experimental data and from [48]) were reproduced.

For this study, several periodic arrays having different patch aspect ratios, b/a, are studied. A normal incidence TE-to-z (i.e. $\phi_i = 90^o$) plane wave is assumed. As such, the $\hat{E}$ vector is x-directed. In all cases, a fixed length of $a = 1.0$cm is utilized for the perfectly conducting patches. Also, each cell size in the array is set constant at $s_x = s_y = 2.0$cm.

2.2.1 Resonant Patch Current and Reflection Coefficient

Initially, the reflection coefficient $\left|R_{200}^{(200)}\right|$ is computed for a number of cases. They are compared with the existing data in the literature, to further validate the computer code. A set of results are shown in Fig. 2-3, for different patch aspect ratios, and they agree well with those in [56]. Note that for $a = 1.0$cm and an x-polarized plane wave, a single patch is resonant at 15.00GHz, regardless of its aspect ratio. This also manifest in the infinite array, where the reflection coefficient becomes zero at 15.00GHz. But, it peaks to about unity just before 15.00GHz. This peak, however, is somewhat frequency dependent, being at 13.11GHz for b/a = 1.00, decreasing to 12.45GHz for b/a = 0.50, and increasing again to 12.63GHz for b/a = 0.25. Also, since the patch dimension a is con-

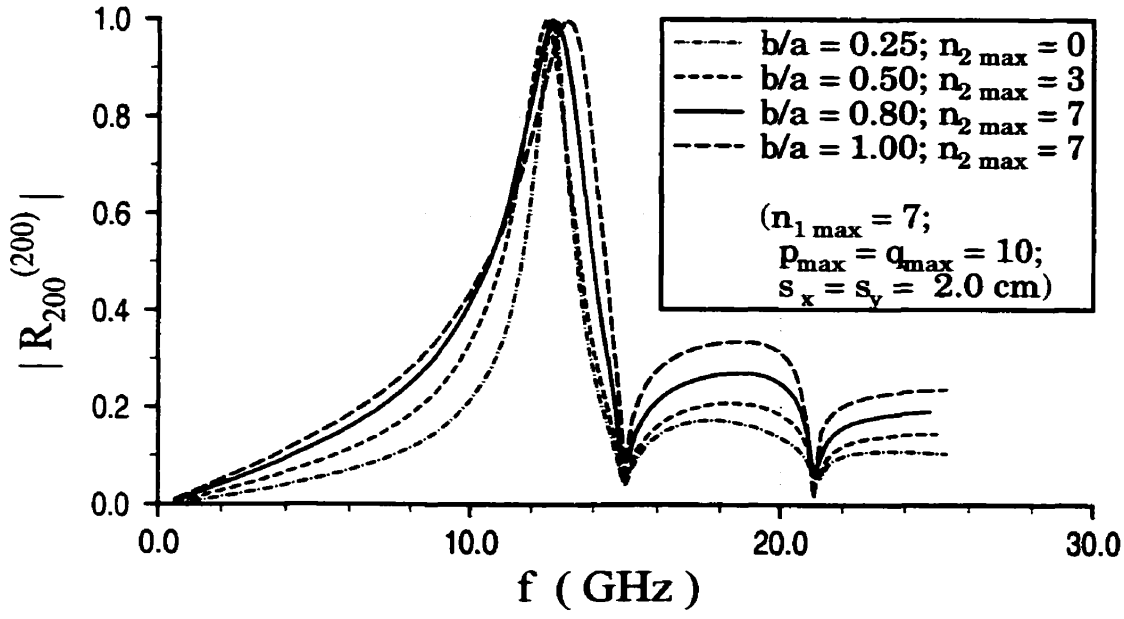

Fig. 2-3: TE-to-z reflection coefficient due to frequency, evaluated using the entire-domain basis function expansion, for different patch aspect ratios b/a. $a = 1.0$cm and incident plane wave at $\theta_i = 0^o$ and $\phi_i = 90^o$.

stant, the number of basis functions along the x-direction is maintained at $n_{1\max} = 7$. But the number $n_{2\max}$, along the y-direction, is reduced from 7 to 0 as the aspect ratio b/a decreases from unity to 0.25. The number of Floquet modes, however, are kept constant at 10, i.e. $p_{\max} = q_{\max} = 10$.

Fig. 2-4 illustrates the current distributions on the perfectly conducting patches for the case of b/a = 0.80 at $f = f_o = 12.65$GHz with parameters $n_{1\max} = n_{2\max} = 7$ and $p_{\max} = q_{\max} = 10$. Since the patch is resonant along the x-direction and the incident

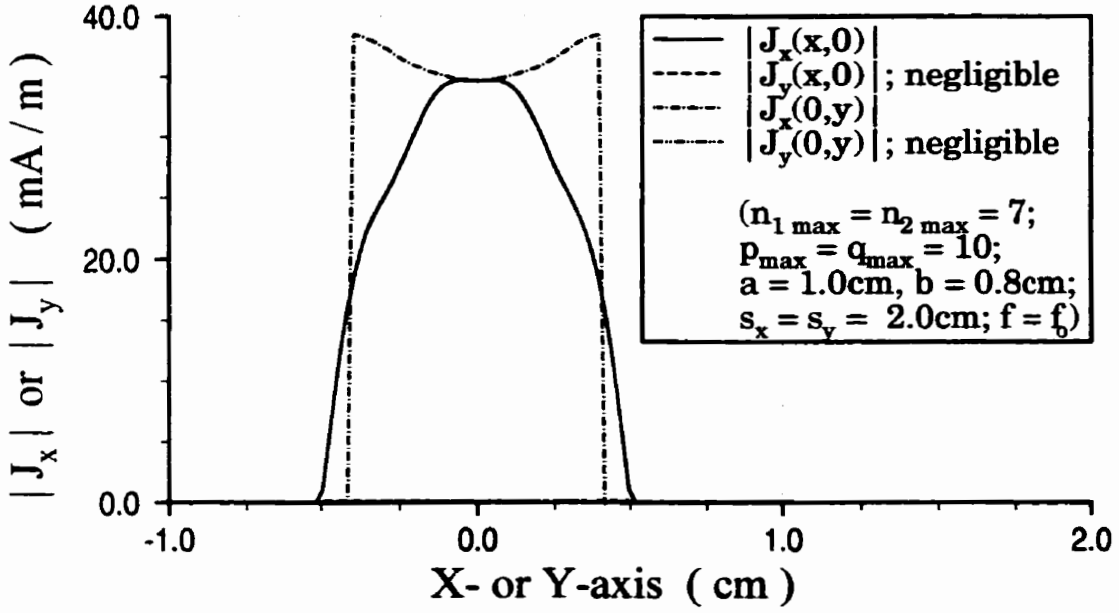

Fig. 2-4: Current distribution of patches in free-space, evaluated using the entire-domain basis function expansion, for $b/a = 0.80$ at $f = f_o = 12.65$GHz. TE-to-z plane wave at $\theta_i = 0°$ and $\phi_i = 90°$.

wave is x-polarized, the magnitude of the x-directed current distribution $|J_x|$ assumes a sinusoidal curve along the x-axis. Along the y-axis, it is a U-shaped curve approximating the current singularity at the edges, as shown in the figure. However, the y-directed current distribution $|J_y|$ is negligible along both the axes.

Similar observations can be made of the current distribution depicted in Fig. 2-5, which is for the case of b/a = 0.25 at $f = f_o = 12.63$GHz. In this case, the modal truncation parameters discussed earlier are $n_{1\max} = 7$, $n_{2\max} = 0$ and $p_{\max} = q_{\max} = 10$. Since

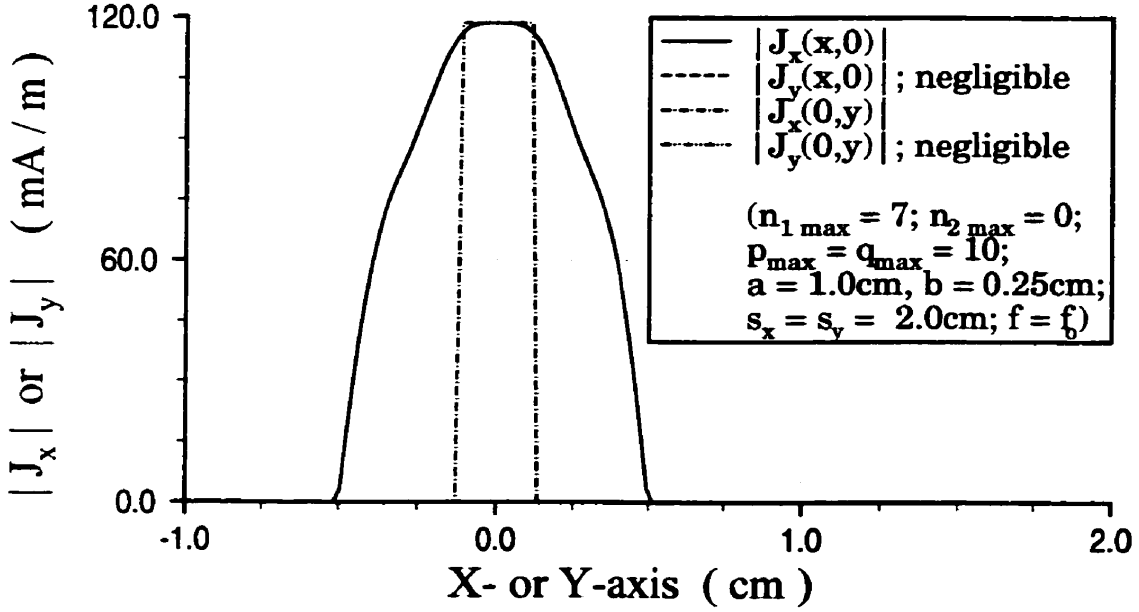

Fig. 2-5: Current distribution of patches in free-space, evaluated using the entire-domain basis function expansion, for $b/a = 0.25$ at $f = f_o = 12.63$GHz. TE-to-z plane wave at $\theta_i = 0°$ and $\phi_i = 90°$.

$n_{2\max} = 0$, the current distribution $|J_x|$ is constant along the y-axis, as is illustrated in the figure. The shape along the x-axis is very similar to that for the case of b/a $= 0.80$. Again, the current distribution $|J_y|$ is negligible along both the axes.

In Fig. 2-6, the variation of $|R_{200}^{(200)}|$ with patch dimension b is plotted for different frequencies. It illustrates that the curves peak to unity at certain values of b which correspond to the resonance phenomena at their respective frequencies. Particularly, for $f = 12.00$GHz, the solution is unity at $b = 0.49$cm, and moves to $b = 1.31$cm for

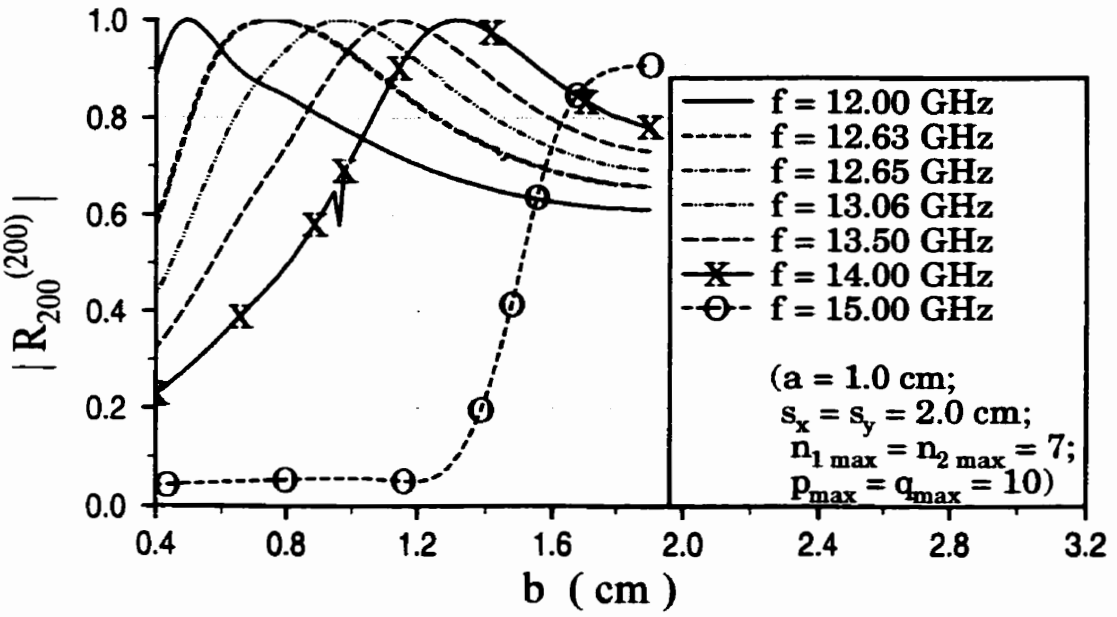

Fig. 2-6: TE-to-z reflection coefficient due to patch dimension b, evaluated using the entire-domain basis function expansion for different frequencies f. $\theta_i = 0^o$ and $\phi_i = 90^o$.

$f = 14.00$GHz. These peaks also tend to become wideband. In this analysis, it should be pointed out, that, the fixed modal parameters are $n_{1\max} = n_{2\max} = 7$ and $p_{\max} = q_{\max} = 10$. Since the modal parameter $n_{1\max} = n_{2\max} = 7$ is employed, the solutions are presumed to be well converged when b is close to 1.00cm, but become less so as b gets smaller.

The relations between the aspect ratios b/a and the various array dimensions in terms of their respective resonance wavelengths λ_o are as tabulated in Table 2-1.

Table 2-1: Array dimensions in terms of wavelengths for TE-to-z incident plane wave with $\theta_i = 0^o$ and $\phi_i = 90^o$. The parameters with fixed values are $a = 1.0$cm and $s_x = s_y = 2.0$cm.

Aspect ratio, b/a	Resonance frequency, f_o(GHz)	Resonance wavelength, λ_o(cm)	Dimension a, a/λ_o	Dimension b, b/λ_o	Cell size, $s_x/\lambda_o = s_y/\lambda_o$
0.25	12.63	2.3753	0.42100	0.10525	0.84200
0.50	12.45	2.4096	0.41501	0.20750	0.83001
0.80	12.65	2.3715	0.42167	0.33734	0.84335
1.00	13.11	2.2883	0.43701	0.43701	0.87401

2.2.2 Convergence of Solution with Entire-Domain Basis Function Expansion

Fig. 2-7 shows the convergence of the solution with $n_{1\max}$. It is seen that the magnitude reflection coefficient $\left|R_{200}^{(200)}\right|$ for b/a = *0.8* and b/a = *1.0* converged well for $n_{1\max} = n_{2\max} = 7$, given that $p_{\max} = q_{\max} = 10$. For b/a = *0.8*, the solution becomes converged from $n_{1\max} = 3$ to $n_{1\max} = 9$. For higher values of $n_{1\max}$, the solution diverges. This divergence behavior for larger $n_{1\max}$ is commonly known as the phenomenon of relative convergence (RC) [88]-[90]. As for the case of b/a = *1.0*, the domain is from $n_{1\max} = 3$ to $n_{1\max} = 11$, which is a greater domain than the former. This implies that the increasing aspect ratio provides an improved convergence stability, given equal Floquet mode numbers.

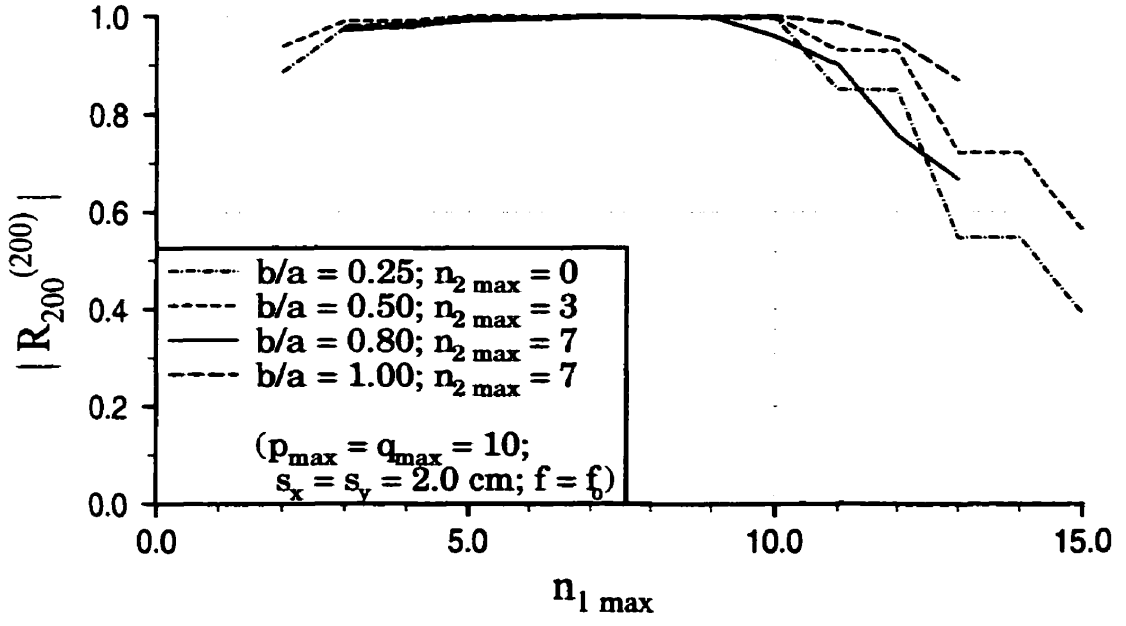

Fig. 2-7: Convergence of TE-to-z reflection coefficient due to $n_{1\max}$, evaluated using the entire-domain basis function expansion for different patch aspect ratios b/a. $\theta_i = 0^o$, $\phi_i = 90^o$, $f = f_o = 12.63$GHz for $b/a = 0.25$, $f = f_o = 12.45$GHz for $b/a = 0.50$, $f = f_o = 12.65$GHz for $b/a = 0.80$, $f = f_o = 13.11$GHz for $b/a = 1.00$, and $a_o = 1.0$cm.

From Fig. 2-7, the convergence domains for cases b/a = *0.25* and b/a = *0.5* are both from $n_{1\max} = 3$ to $n_{1\max} = 11$, respectively, given that $p_{\max} = q_{\max} = 10$. For both of these cases, the RC phenomenon is also present. It is noted that with the assigned modal truncation parameters, the solution beyond the critical point of the RC phenomenon diverges rapidly as the aspect ratio b/a decreases.

On the convergence of Floquet modes, the results are well converged at values of $p_{\max} = q_{\max} = 10$ for all cases of aspect ratio tested, as shown in Fig. 2-8. In this analysis, $n_{1\max} = 7$ is fixed for all cases. From the figure, the solutions converged well with $p_{\max} = q_{\max} = 8$ for all cases, with the exception of b/a = *1.0*, in which the result is well converged for $p_{\max} = q_{\max} = 7$. The solution for the case b/a = *0.25* improves at the quickest rate prior to convergence, whereas, that for the case of b/a = *1.0* improves the least. This implies that the case of b/a = *1.0* is more stable as compared to the rest.

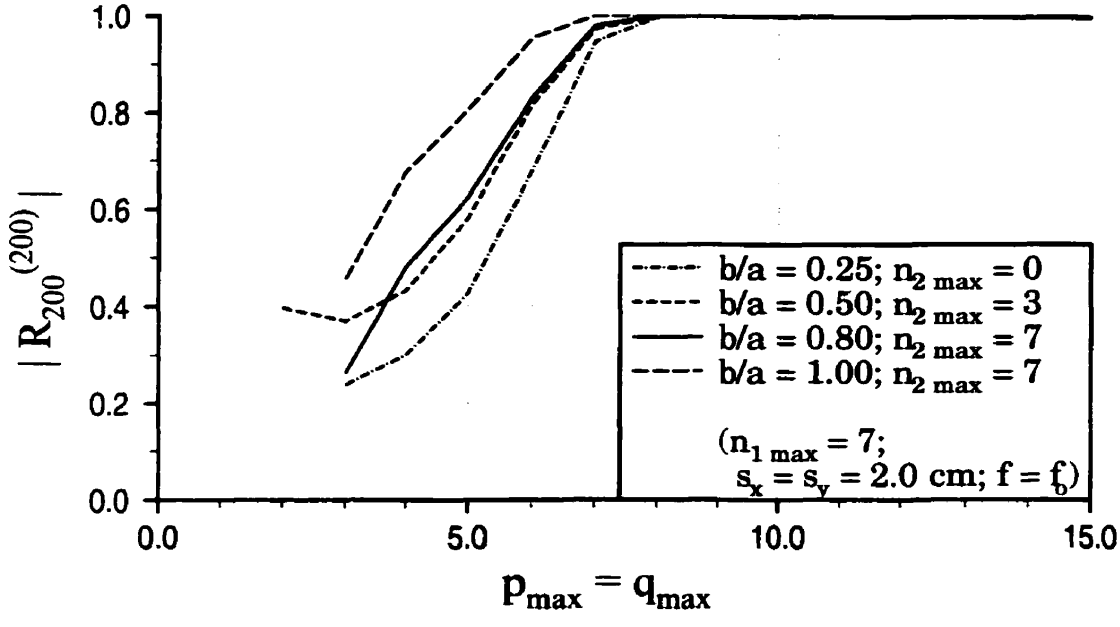

Fig. 2-8: Convergence of TE-to-z reflection coefficient due to Floquet modes $p_{\max}$ and $q_{\max}$, evaluated using the entire-domain basis function expansion for different patch aspect ratios *b/a*. $\theta_i = 0^o$, $\phi_i = 90^o$, $f = f_o = 12.63$GHz for *b/a = 0.25*, $f = f_o = 12.45$GHz for *b/a = 0.50*, $f = f_o = 12.65$GHz for *b/a = 0.80*, $f = f_o = 13.11$GHz for *b/a = 1.00*, and $a_o = 1.0$cm.

The $n_{1\max}$ convergence studies for b/a = *0.25* are shown in Fig. 2-9, where $p_{\max} = q_{\max} = 10$ is held constant. In the figure, the domain for which the solution is converged, when $n_{2\max} = 0$, ranges from $n_{1\max} = 3$ to $n_{1\max} = 10$, after which the solution diverges due to the occurrence of the RC phenomenon. In general, the domain of $n_{1\max}$ is less sensitive to variation in $n_{2\max}$.

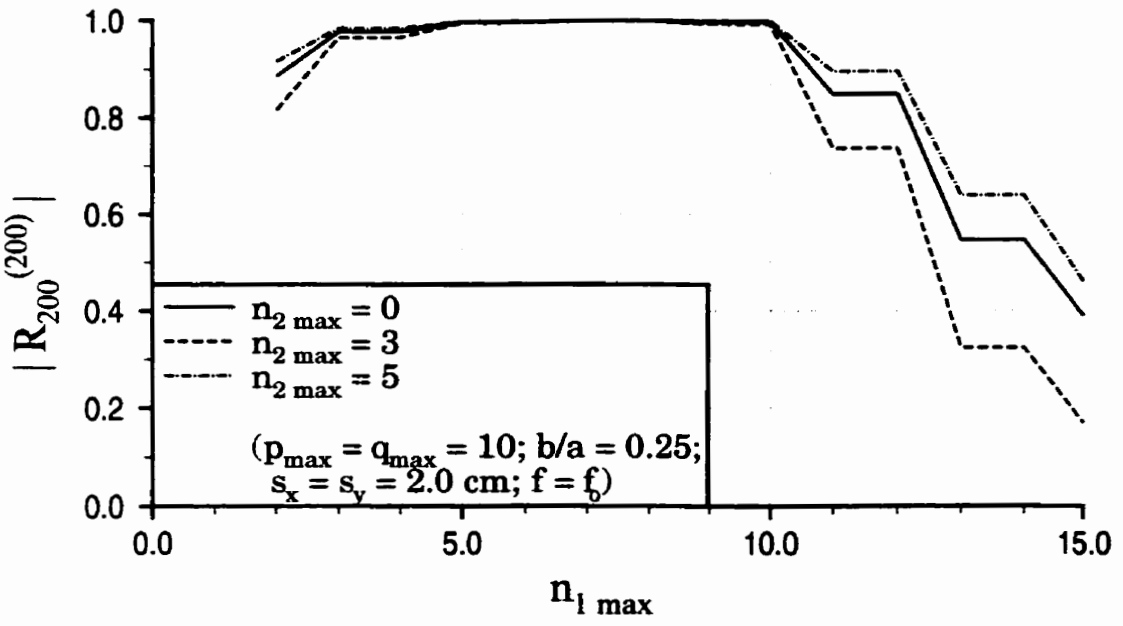

Fig. 2-9: Convergence of TE-to-z reflection coefficient due to n_{1max}, evaluated using the entire-domain basis function expansion for $b/a = 0.25$. $\theta_i = 0^o$, $\phi_i = 90^o$, $f = f_o = 12.63$GHz, and $a_o = 1.0$cm.

The convergence of the Floquet modes are presented in Fig. 2-10. For b/a = *0.25*, stable solutions are obtained with $n_{1\max} = 7$ and $n_{2\max} = 0$, when $p_{\max} = q_{\max} \geq 8$. For larger values of $n_{2\max}$, the convergence is not stable.

For the next analysis, $n_{1\max} = 7$ and $p_{\max} = q_{\max} = 10$ are fixed. From Fig. 2-11, the magnitudes of reflection coefficient $\left|R_{200}^{(200)}\right|$ for all cases are approximately unity for near normal (i.e. for $\theta < 5.0°$) incidences. For other incident angles, results are dependent on the aspect ratio b/a.

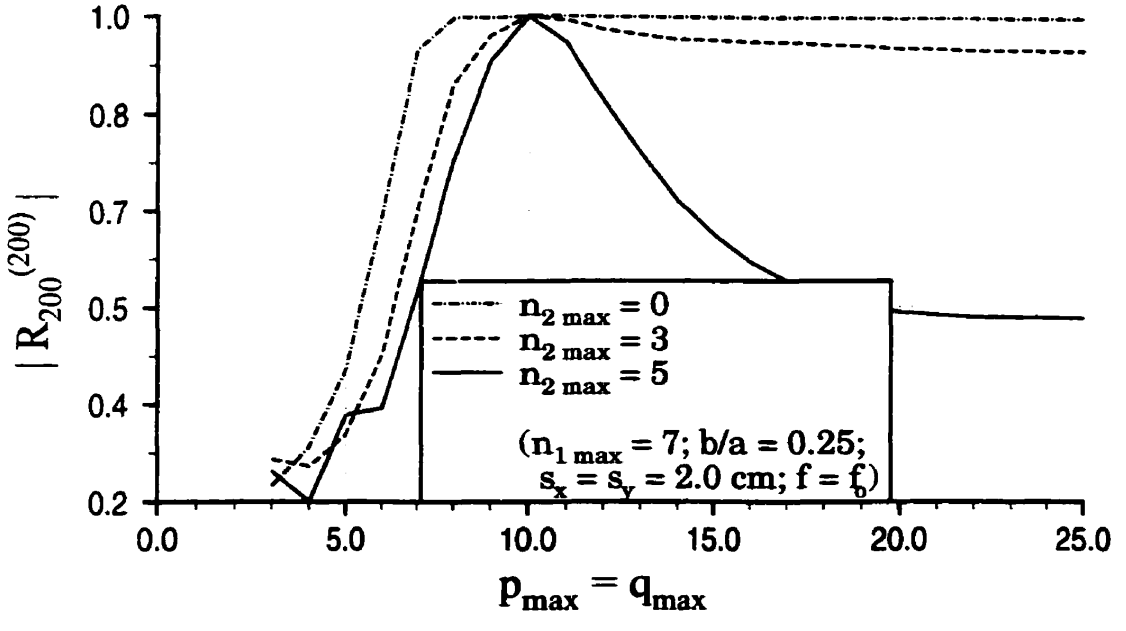

Fig. 2-10: Convergence of TE-to-z reflection coefficient due to Floquet modes $p_{\max}$ and $q_{\max}$, evaluated using the entire-domain basis function expansion for $b/a = 0.25$. $\theta_i = 0^o$, $\phi_i = 90^o$, $f = f_o = 12.63$GHz, and $a_o = 1.0$cm.

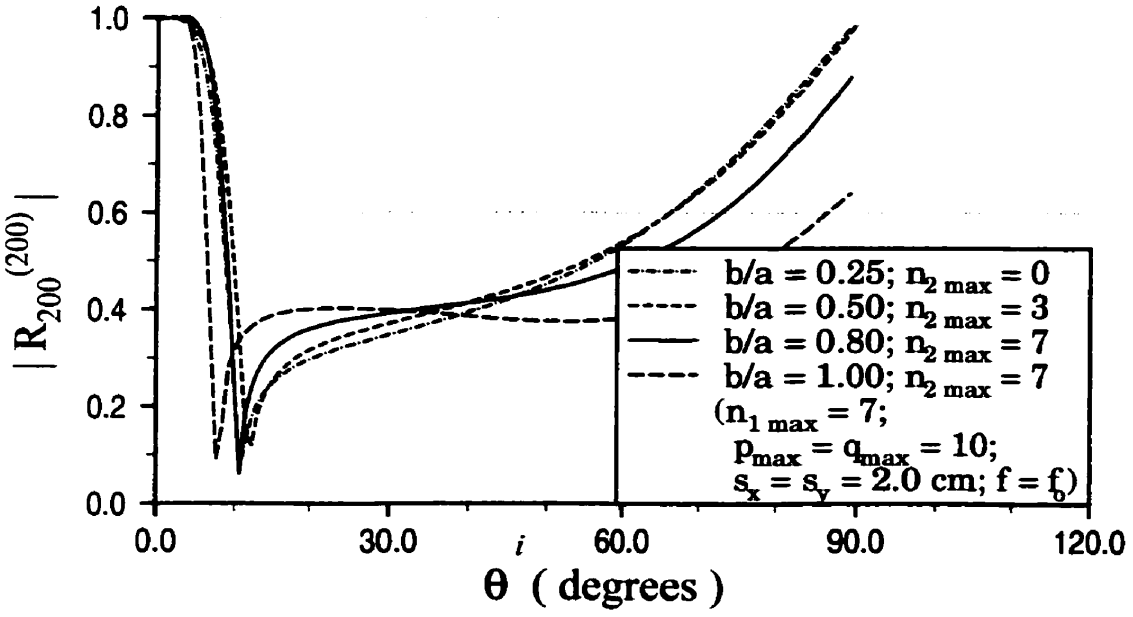

Fig. 2-11: TE-to-z reflection coefficient due to incident angle θ_i, evaluated using the entire-domain basis function expansion for different patch aspect ratios b/a. $\phi_i = 90^o$, $f = f_o = 12.63$GHz for $b/a = 0.25$, $f = f_o = 12.45$GHz for $b/a = 0.50$, $f = f_o = 12.65$GHz for $b/a = 0.80$, $f = f_o = 13.11$GHz for $b/a = 1.00$, and $a_o = 1.0$cm.

To verify the null in Fig. 2-11, the convergence analysis of Fig. 2-12 is plotted for the patch aspect ratio b/a = 0.8, with a TE-to-z incidence angle $\theta_i = 10.6°$. Two cases are illustrated: The first being $n_{1\max} = n_{2\max}$, and the next being $n_{1\max} = 7$, with the fixed modal parameter being $p_{\max} = q_{\max} = 10$. The magnitude reflection coefficient $\left|R_{200}^{(200)}\right|$ is 0.01 and is relatively constant from $n_{2\max} = 3$ through $n_{2\max} = 10$ for both cases. This small value is consistent with the null at $\theta = 10.66°$ for b/a = 0.8 shown in

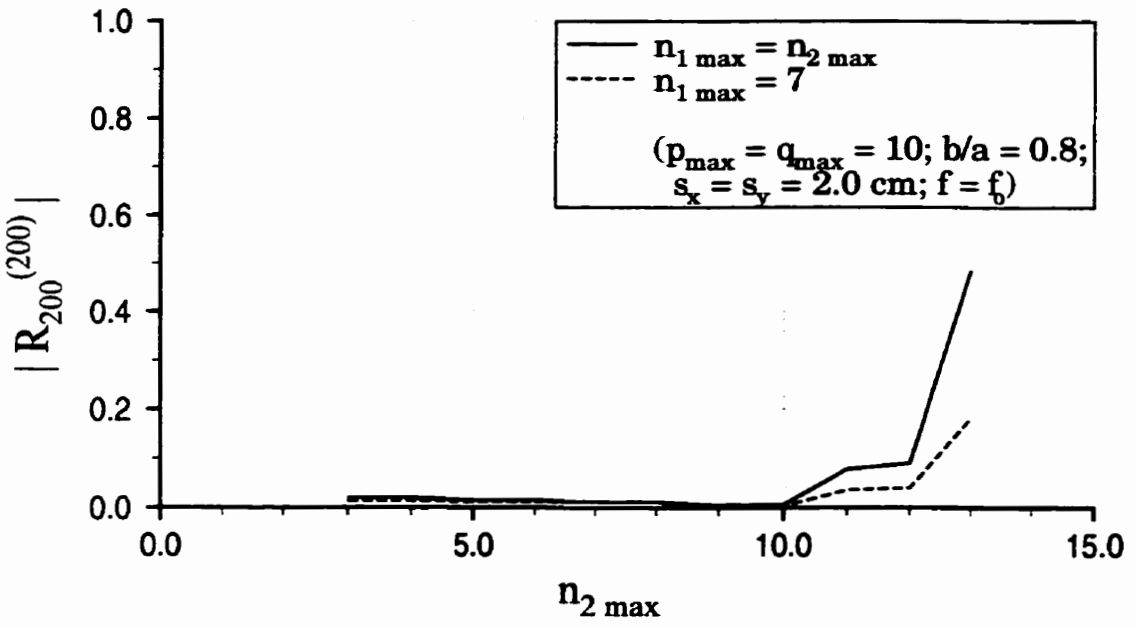

Fig. 2-12: Convergence of TE-to-z reflection coefficient due to n_{2max}, evaluated using the entire-domain basis function expansion for $b/a = 0.80$ at reflection coefficient null. $\theta_i = 10.6^o$, $\phi_i = 90^o$, $f = f_o = 12.65$GHz and $a_o = 1.0$cm.

Fig. 2-11. For larger $n_{2\max}$, the solutions become divergent due to the onset of the RC phenomenon. Here, the former has the worst divergence of the two. For the Floquet modal sweep for this case, the solution achieved stability at $p_{\max} = q_{\max} = 9$ for which the solution $\left|R_{200}^{(200)}\right| = 0.01$ is relatively constant. That is, this relatively small value also indicates a null occurrence at that incidence angle.

2.3 EXTENSION TO SUBDOMAIN BASIS FUNCTION EXPANSION

In the numerical modelling of these infinite periodic patch arrays using modal formulations involving the Floquet's Theorem, the subdomain basis functions can easily be utilized for complex geometries, but may require large number of terms to represent the current distribution on the patch surface. Entire-domain basis functions, on the other hand, are more suitable for simple patch geometries, and require smaller number of terms to converge.

Numerical convergences of the subdomain roof-top basis functions are compared with those of the entire-domain sinusoidal basis functions in this investigation. Particularly, current distributions and various reflection properties obtained through these basis functions are studied.

2.3.1 Subdomain Basis Function Expansion

For the subdomain basis function expansion, the unknown current densities $\hat{J}_s(\hat{\rho}'_T)$ of (2-10a) and (2-11) are expanded into the modal expression

$$\hat{J}_s(\hat{\rho}_T) = \sum_{n'_x}\left\{c_{n'_x}\hat{h}_{n'_x}(\hat{\rho}_T)\right\} + \sum_{n'_y}\left\{c_{n'_y}\hat{h}_{n'_y}(\hat{\rho}_T)\right\}, \tag{2-16}$$

where $\hat{h}_{n'_x}(\vec{r}_T)$ and $\hat{h}_{n'_y}(\vec{r}_T)$ are subdomain modal basis vectors in the x- and y- directions, respectively, and, $c_{n'_x}$ and $c_{n'_y}$ are unknown modal coefficients to be solved, for currents in the x- and y- directions, respectively.

The eigenvalue equations for x- and y- components, using the subdomain basis function expansion, are

$$\begin{aligned}
&\vec{\Upsilon}^{(l)}_{g'_x 00}{}^{*}(\vec{r}_T)\cdot\sum_m\{B_m^{(i)}(1+R^{(2)}_{m00})\hat{\kappa}^{(l)}_{m00}\} \\
&\quad=\sum_{n'_x}\left\{\frac{c_{n'_x}}{A}\sum_{mpq}\left\{\frac{1}{\zeta^{(eq)}_{mpq}}[\hat{\kappa}^{(l)}_{mpq}\cdot\vec{\Upsilon}^{(l)}_{n'_x pq}(\vec{r}_T)][\hat{\kappa}^{(l)}_{mpq}\cdot\vec{\Upsilon}^{(l)}_{g'_x pq}(\vec{r}_T)^{*}]\right\}\right\} \\
&\qquad+\sum_{n'_y}\left\{\frac{c_{n'_y}}{A}\sum_{mpq}\left\{\frac{1}{\zeta^{(eq)}_{mpq}}[\hat{\kappa}^{(l)}_{mpq}\cdot\vec{\Upsilon}^{(l)}_{n'_y pq}(\vec{r}_T)][\hat{\kappa}^{(l)}_{mpq}\cdot\vec{\Upsilon}^{(l)}_{g'_x pq}(\vec{r}_T)^{*}]\right\}\right\}
\end{aligned} \tag{2-17a}$$

and

$$\begin{aligned}
&\vec{\Upsilon}^{(l)}_{g'_y 00}{}^{*}(\vec{r}_T)\cdot\sum_m\{B_m^{(i)}(1+R^{(2)}_{m00})\hat{\kappa}^{(l)}_{m00}\} \\
&\quad=\sum_{n'_x}\left\{\frac{c_{n'_x}}{A}\sum_{mpq}\left\{\frac{1}{\zeta^{(eq)}_{mpq}}[\hat{\kappa}^{(l)}_{mpq}\cdot\vec{\Upsilon}^{(l)}_{n'_x pq}(\vec{r}_T)][\hat{\kappa}^{(l)}_{mpq}\cdot\vec{\Upsilon}^{(l)}_{g'_y pq}(\vec{r}_T)^{*}]\right\}\right\} \\
&\qquad+\sum_{n'_y}\left\{\frac{c_{n'_y}}{A}\sum_{mpq}\left\{\frac{1}{\zeta^{(eq)}_{mpq}}[\hat{\kappa}^{(l)}_{mpq}\cdot\vec{\Upsilon}^{(l)}_{n'_y pq}(\vec{r}_T)][\hat{\kappa}^{(l)}_{mpq}\cdot\vec{\Upsilon}^{(l)}_{g'_y pq}(\vec{r}_T)^{*}]\right\}\right\},
\end{aligned} \tag{2-17b}$$

respectively, where

$$\vec{\Upsilon}^{(l)}_{n'_x pq}(\vec{r}_T)=\int_{A'}\hat{h}_{n'_x}(\vec{r}_T)e^{j\vec{k}^{(l)}_{Tpq}\cdot\vec{r}_T}dr_T \tag{2-17c}$$

and

$$\vec{\Upsilon}^{(l)}_{n'_y pq}(\vec{r}_T) = \int_{A'} \vec{h}_{n'_y}(\vec{r}_T) e^{j\vec{k}^{(l)}_{Tpq} \cdot \vec{r}_T} dr_T \qquad \text{(2-17d)}$$

are their corresponding orthogonal mode functions associated with the current density $\vec{J}_s(\vec{r}'_T)$, respectively.

Using the index mapping $n'_x \rightarrow (n_1, n_2, x)$ and $n'_y \rightarrow (n_1, n_2, y)$, the modal basis vectors $\vec{h}_{n'_x}(\vec{r}_T)$ and $\vec{h}_{n'_y}(\vec{r}_T)$ become $h_{n_1 n_2 x}(x, y)\,\hat{x}$ and $h_{n_1 n_2 y}(x, y)\,\hat{y}$, respectively. The scalar functions $h_{n_1 n_2 x}(x, y)$ and $h_{n_1 n_2 y}(x, y)$ are subdomain roof-top basis functions in the x- and y- directions, respectively [51], and are defined in Appendix A, Section A.3.

In addition, because of the roof-top basis functions, (2-17c) and (2-17d) are evaluated by closed-form integrations. The first-order (*00*-th) Floquet modal reflection coefficient is easily determined from (2-15).

2.3.2 Comparisons Between Subdomain and Entire-Domain Basis Functions

A normal incidence ($\theta_i = 0°$) TE-to-z plane wave at $\phi_i = 90°$ is again assumed, where $\vec{E}$ is x-polarized, as in Section 2.2. For the conductive patch in free-space, its length is again fixed as $a = 1.0$cm, with a constant cell size of $s_x = s_y = 2.0$cm, while its width b is varied.

To obtain a converged solution using the subdomain basis function expansion for aspect ratio $b/a = 0.8$, at frequency $f = 13.26$GHz, optimal truncations of basis function and Floquet mode terms are determined. That is, $n_{1\max} = 3$ and $n_{2\max} = 2$ for the basis function terms, and $p_{\max} = 10$ and $q_{\max} = 9$ for the Floquet mode terms. This requires a total of *58* basis function terms, and *399* Floquet mode terms, respectively.

Although the solution has converged, the patch current distribution along the y-axis in Fig. 2-13(a) appears not smooth due to subdomain segmentations. As the number of segmentations is increased to $n_{1\max} = 5$ and $n_{2\max} = 4$ for the basis function terms, and $p_{\max} = 14$ and $q_{\max} = 19$ for the Floquet mode terms, the distribution appears smoother, as in Fig. 2-13(b). This involves a total of *178* basis function terms and *1131* Floquet mode terms, respectively, which is a significant increase.

The TE-to-z reflection coefficient magnitude $\left|R_{200}^{(200)}\right|$ due to frequency, corresponding to Fig. 2-4 and Fig. 2-13(a), is illustrated in Fig. 2-14(a). This figure indicates that the resonance frequency for the subdomain basis function expansion is $f_o = 13.24$GHz, agreeing well with the periodic spectral Green's function technique in [56], for the same free-standing array geometry. That for the entire-domain basis function expansion in the figure is $f_o = 12.78$GHz. The percentage difference for these frequencies is *1.77%*. To improved this, additional basis functions for representing edge-current effects may be incorporated into the entire-domain basis function expansion formulation.

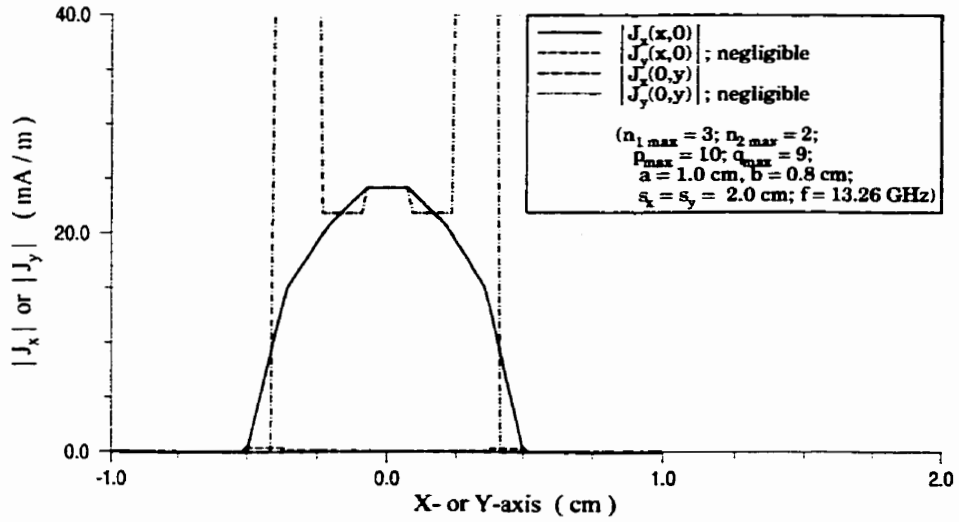

(a)

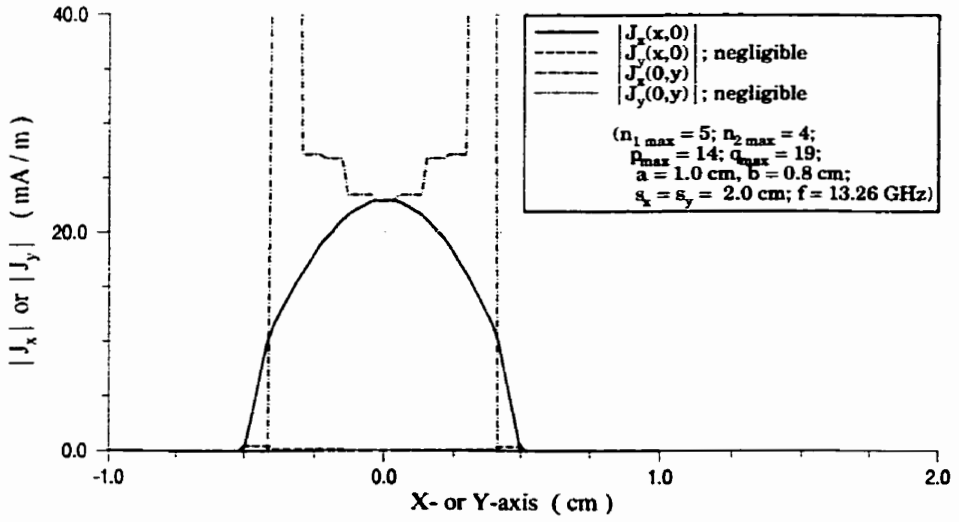

(b)

Fig. 2-13: Current distributions of patches in free-space, evaluated using the subdomain basis function expansion, for aspect ratio $b/a = 0.8$: (a) $n_{1\max} = 3$, $n_{2\max} = 2$, $p_{\max} = 10$ and $q_{\max} = 9$, and (b) $n_{1\max} = 5$, $n_{2\max} = 4$, $p_{\max} = 14$ and $q_{\max} = 19$. TE-to-z plane wave at $\theta_i = 0°$ and $\phi_i = 90°$.

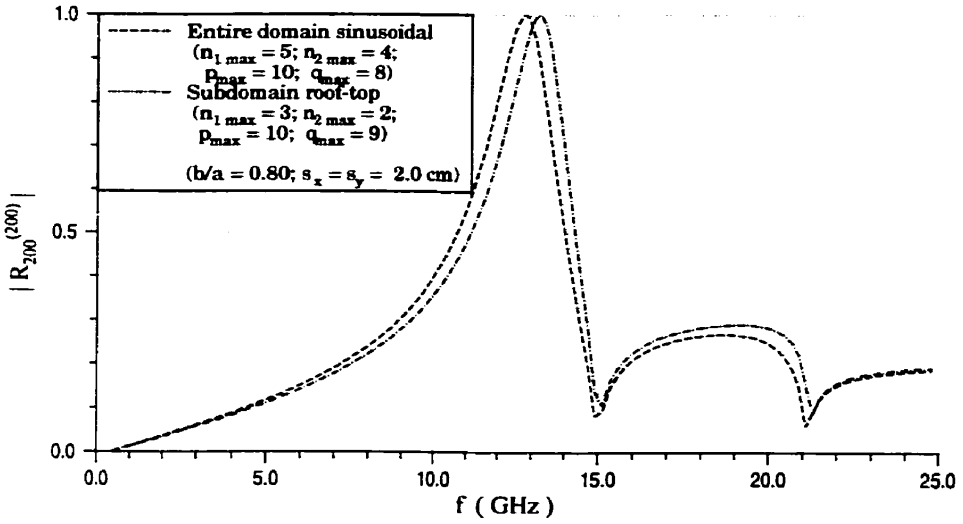

(a)

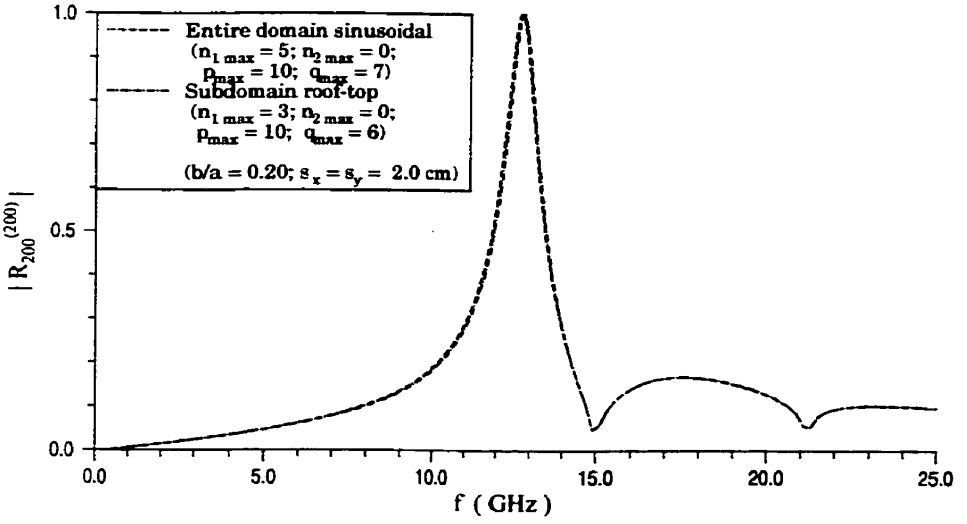

(b)

Fig. 2-14: Comparisons of TE-to-z reflection coefficients due to frequency, evaluated using entire-domain and subdomain basis function expansions: (a) aspect ratio $b/a = 0.8$, and (b) aspect ratio $b/a = 0.2$. $a = 1.0$cm, $s_x = s_y = 2.0$cm. $\theta_i = 0°$ and $\phi_i = 90°$.

The patch current distribution for aspect ratio $b/a = 0.2$, evaluated using the subdomain basis function expansion at frequency $f = 12.85$GHz, is depicted in Fig. 2-15. For its

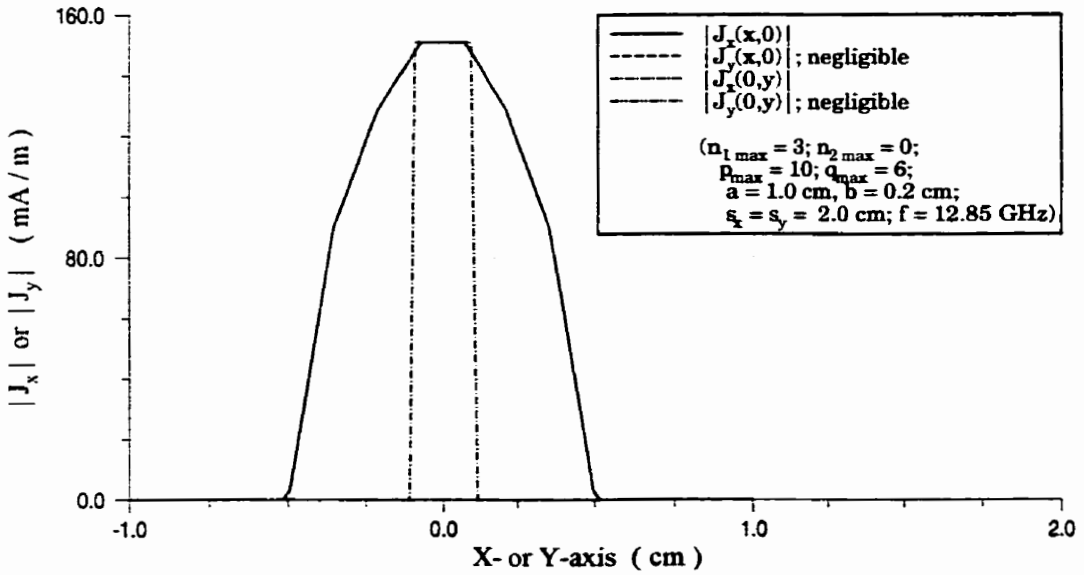

Fig. 2-15: Current distribution of patches in free-space, evaluated using the subdomain basis function expansion, for aspect ratio $b/a = 0.2$. TE-to-z plane wave at $\theta_i = 0°$ and $\phi_i = 90°$.

corresponding frequency variations depicted in Fig. 2-14(b), its resonance frequency is $f_o = 12.79$GHz. That corresponding to Fig. 2-5, shown in Fig. 2-14(b) for the entire-domain basis function expansion, is $f_o = 12.74$GHz. The percentage difference for these frequencies is *0.20%*.

In Fig. 2-16, for aspect ratio $b/a = 0.8$ with the specified truncations shown, the range where $\left|R_{200}^{(200)}\right|$ is well converged runs from $n_{1\max} = 2$ to $n_{1\max} = 5$, and from $n_{2\max} = 1$ to $n_{2\max} = 4$. For aspect ratio $b/a = 0.2$, the range is smaller, that is, from $n_{1\max} = 2$ to $n_{1\max} = 4$, since the cross-polarized current component $\mathcal{J}_y$ is negligibly small.

Fig. 2-17 illustrates the convergences of $\left|R_{200}^{(200)}\right|$ due to $p_{\max}$ and $q_{\max}$, evaluated using the subdomain basis function expansion, for aspect ratios $b/a = 0.8$ and $b/a = 0.2$.

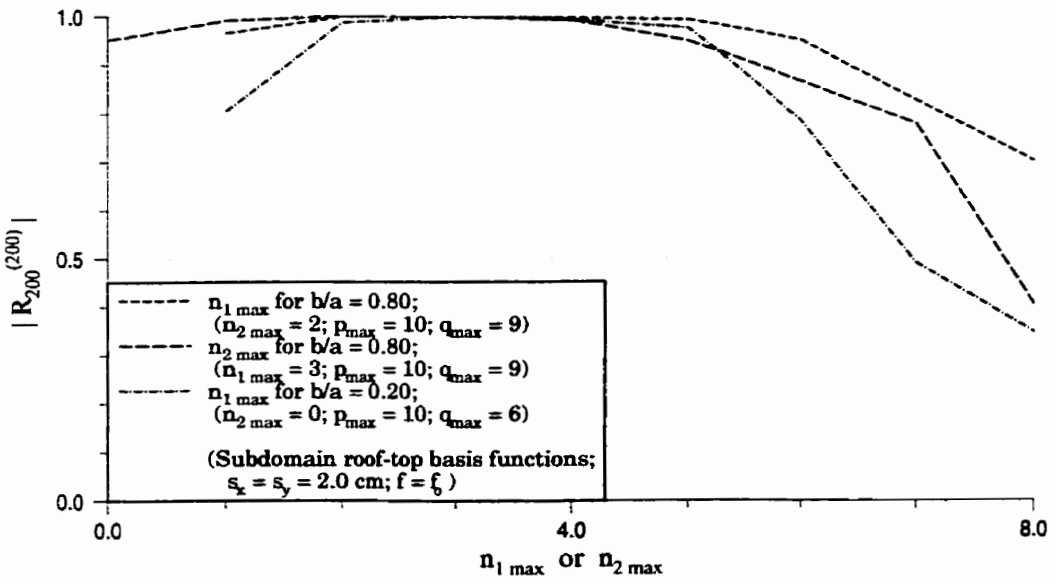

Fig. 2-16: Convergence of TE-to-z reflection coefficient due to $n_{1\max}$ and $n_{2\max}$, evaluated using the subdomain basis function expansion for different patch aspect ratios b/a. $\theta_i = 0^o$, $\phi_i = 90^o$, $f = f_o = 12.79$GHz for $b/a = 0.2$, $f = f_o = 13.24$GHz for $b/a = 0.80$, and $a_o = 1.0$cm.

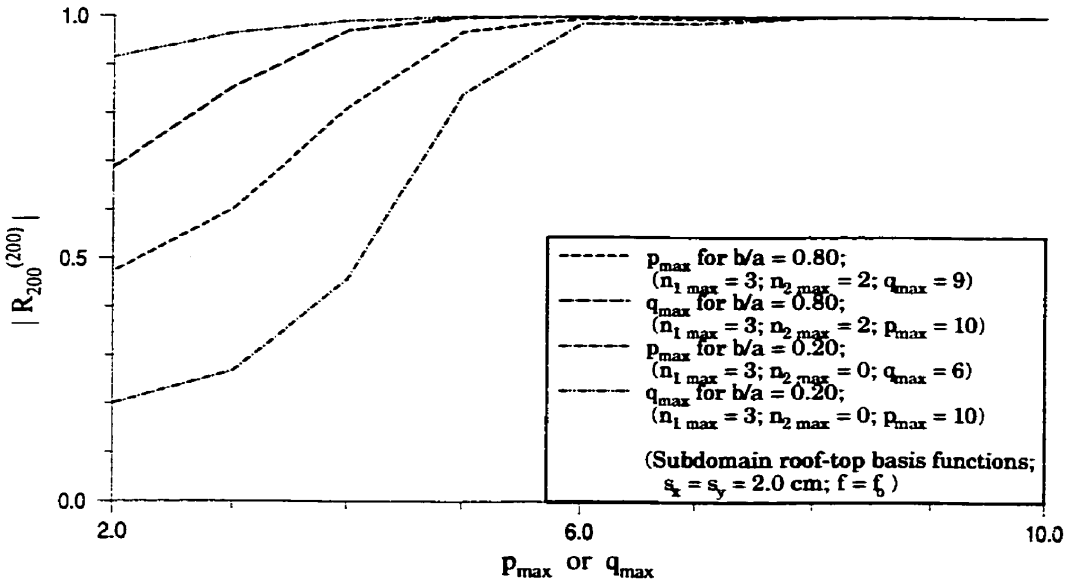

Fig. 2-17: Convergence of TE-to-z reflection coefficient due to Floquet modes $p_{\max}$ and $q_{\max}$, evaluated using the subdomain basis function expansion for different patch aspect ratios b/a. $\theta_i = 0^o$, $\phi_i = 90^o$, $f = f_o = 12.79$GHz for $b/a = 0.2$, $f = f_o = 13.24$GHz for $b/a = 0.80$, and $a_o = 1.0$cm.

The computations require smaller $q_{\max}$ to converge, compared to $p_{\max}$, for both aspect ratios.

These convergence results of Fig. 2-16 and Fig. 2-17 verify that $\left|R_{200}^{(200)}\right|$ is well converged for the specified $n_{1\max}$, $n_{2\max}$, $p_{\max}$ and $q_{\max}$ employed in the evaluations of patch current distributions of Fig. 2-13.

In general, given a fixed Floquet mode truncations $p_{\max}$ and $q_{\max}$, $\left|R_{200}^{(200)}\right|$ decays as $n_{1\max}$ exceeds a certain critical value. A similar behavior is also observed for $n_{2\max}$. This is the phenomenon of relative convergence (RC) [88]-[90], which has also been observed in results of Section 2.2.2.

For $\left|R_{200}^{(200)}\right|$ due to incident angle θ_i, as illustrated in Fig. 2-18, both entire-domain and subdomain basis function expansions utilized disagree at nulls. For the subdomain case, with $f_o = 13.24$GHz, the null occurs at $\theta_i = 7.6°$, agreeing well [56]. For the entire-

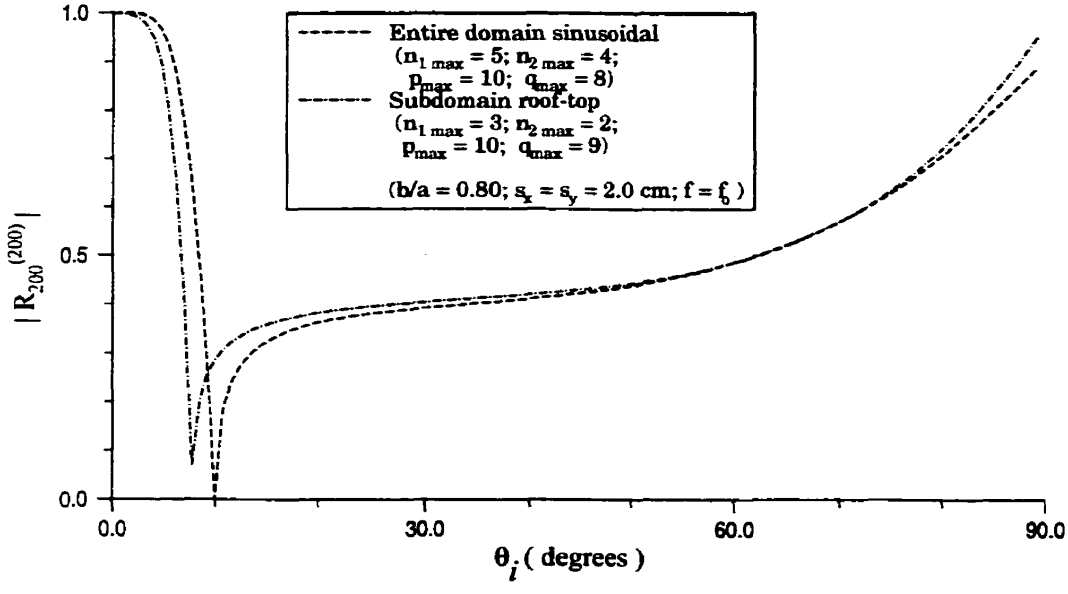

Fig. 2-18: TE-to-z reflection coefficient due to incident angle θ_i, evaluated using the entire-domain and subdomain basis function expansions for patch aspect ratio $b/a = 0.80$. $\phi_i = 90^o$, $f = f_o = 12.65$GHz for the entire-domain basis function expansion, $f = f_o = 13.24$GHz for the subdomain basis function expansion, and $a_o = 1.0$cm.

domain case, with $f_o = 12.78\text{GHz}$, the null occurs at $\theta_i = 9.9°$. This discrepancy may be attributed to the same patch being evaluated at two distinct frequencies.

2.4 APPLICATION TO MICROSTRIP PATCH ARRAYS

Fig. 2-19 illustrates the schematics for the infinite periodic array modelling of microstrip patches. For this application, the Floquet modal reflection coefficient $R^{(3)}_{mpq}$ of (2-10b), for both the TM- and TE- to-z cases, is provided as [91][92]

$$R^{(3)}_{mpq} = -e^{-j2\Gamma^{(2)}_{pq} z_a}; \quad m = 1, 2. \tag{2-18}$$

To solve (2-10a) for this case, the unknown current density $\vec{J}_s(\vec{r}'_T)$ is expanded into modal basis vectors and unknown modal coefficients, using the subdomain basis function expansion.

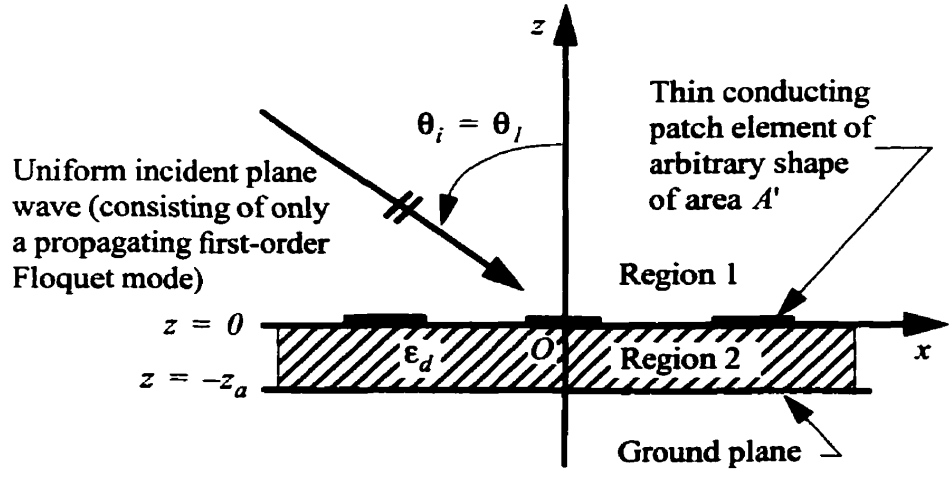

Fig. 2-19: Cross section of an infinite periodic array of microstrip patches.All media, except for the patch elements, are isotropic, homogeneous dielectric materials with zero-conductivity.

For evaluating more complex patch geometries, a subsectional patch segmentation scheme [93] is implemented into the computer code *ARCOF*, along with the subdomain roof-top basis function formulations. The Galerkin's Method of Moment [87] is utilized for the numerical evaluation of unknown modal coefficients, from which the first-order (*00*-th) Floquet modal, or specular, reflection coefficient is computed. This approach would be utilized for the reflection coefficient phase analysis of microstrip reflectarrays in subsequent chapters.

2.5 CONCLUSION

In this analysis, numerous reflection properties of an infinite periodic array of rectangular patches in free space is investigated using the Floquet modal analysis technique, formulated with entire-domain and subdomain basis function expansions. Furthermore, an extension of this technique to microstrip patch arrays is presented.

Effects of varying patch aspect ratio and element separation are also studied. These include convergence behaviors of basis functions and Floquet modes. The phenomenon of relative convergence (RC) is observed when the number of basis function employed exceeds a certain critical value, at a given Floquet mode truncation.

In general, the patch current distribution is more sensitive to modal truncations, whereas, the reflection coefficient magnitude is less sensitive to such truncations. The patch current distribution also is more sensitive to basis function truncations, than to Floquet mode trun-

cations. The sensitivity is generally higher for cross polarization (y-directed current) computation than for the co-polarization (x-directed current).

3 Single-Layer Analysis

The analysis of scattering from an infinite periodic array of microstrip patches is employed to study line-source-fed single-layer microstrip reflectarrays [84][85]. Utilizing rectangular patch geometries in the modelling, the reflection phase properties of the reflectarray are rigorously examined. Important parameters, such as, patch length, and substrate permittivity and thickness, are investigated. Included in the study are the effects of unattainable reflection phase on phase correction errors and radiation characteristics. Multiple patch geometries, implemented in the patch array for enhanced performance, are also examined.

In general, a thick substrate has potential for improving both bandwidth and far-field radiation characteristics of the reflectarray. These two issues are investigated in this chapter through numerical modelling, using two different substrates, namely, a thin $\varepsilon_r = 2.5$ substrate and a thick foam ($\varepsilon_r = 1.03$) substrate. This includes a study of the effects of unattainable reflection phase, which produces phase correction errors, on the directivities, side-lobe levels (SLL) and bandwidths. A combination of multiple patch geometries, implemented into the patch array for enhanced performance, is also explored.

For the microstrip reflectarray, a line-source-fed configuration is selected. Although a line-source-fed configuration has been used for a quasi-periodic echelette reflector antenna [35], a line-source-fed configuration for a microstrip reflectarray is new, and it possesses a unique property. That is, phase corrections are necessary only in one plane, and as such, the influence of the substrate and patch parameters on the far-field radiation characteristics can be investigated accurately.

3.1 MODELLING CONJECTURE

In a conventional reflectarray fed by a point source and having an adequately large "focal" length F, the incident wave from the feed approximates a uniform plane wave. Thus, as a first approximation, the analysis for scattering from an infinite periodic array of single-layer microstrip patches may be employed as a modelling tool [7]. An analysis similar to those in [2][91], discussed in detailed in Chapter 2, may be used to determine the scattered field due to the array of microstrip patches. In this method, it is assumed that a plane wave is incident upon a uniform array of microstrip patches at an angle $\theta_i = \theta_{mn}$, where θ_i is the plane wave incident angle, and θ_{mn} is the subtended angle from the feed to the (m, n)-th patch in the array.

3.1.1 Line-Source-Fed Design

In a reflectarray fed by a line-source, the situation is somewhat different. There is no field variation along an ideal line-source, as its length is infinite. However, in a practical

design, the line-source length is finite and the field uniformity is maintained at short distances, where the field collimation has not commenced. Also, a line-source radiates a cylindrical wave. The reflectarray must therefore be placed in the near-field (Fresnel) zone of the line-source. That is, referring to Fig. 3-1 and Fig. 3-2, no variation in amplitude and phase occurs along the x-axis, which is the line-source axis. Variations occur only in the

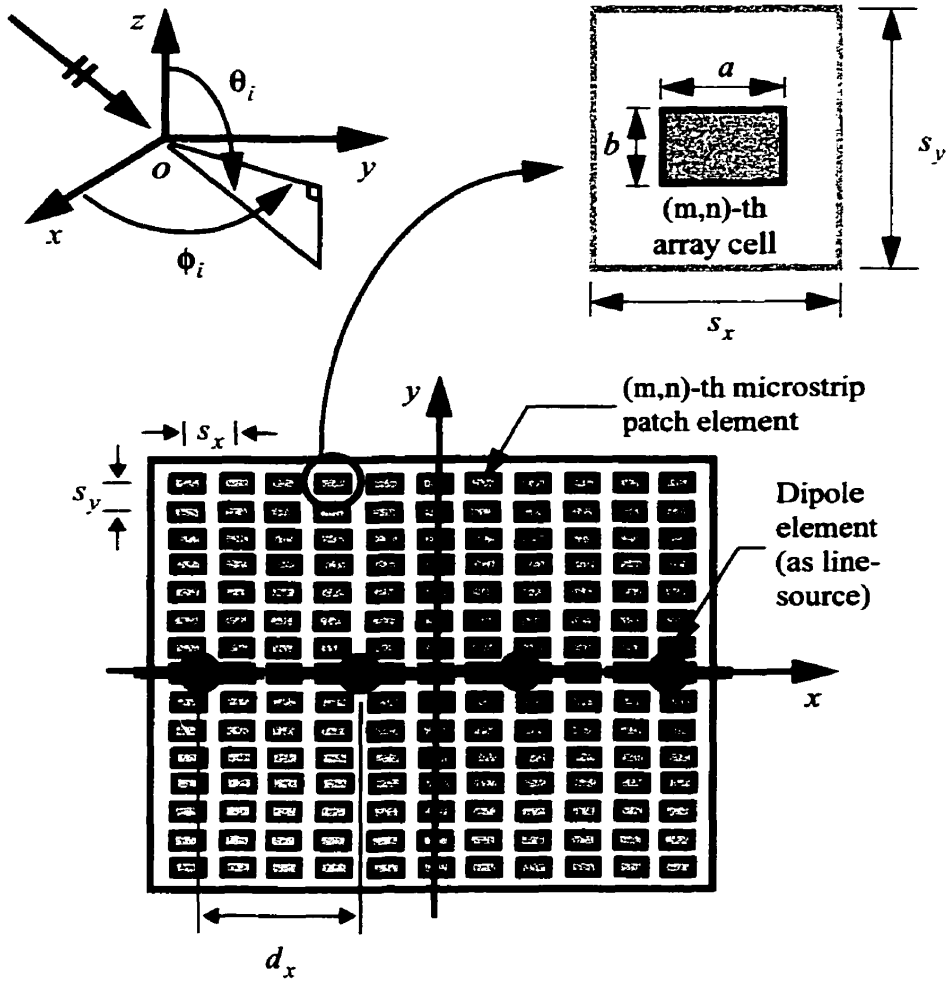

Fig. 3-1: Front view schematics of a line-source-fed microstrip reflectarray with an x-polarized $\hat{E}$ field from the line-source. The patch array is consist of single-layer rectangular microstrip patches, and $\theta_n = \theta_i$ for the infinite periodic array simulations.

transverse direction, which is the yz-plane, and are governed by the asymptotic form of the cylindrical Hankel function of zero order. The phase variation is that of a two-dimensional plane wave, depending on the y and z variables. Furthermore, the amplitude decay is slow, as the square-root of the distance from the line-source.

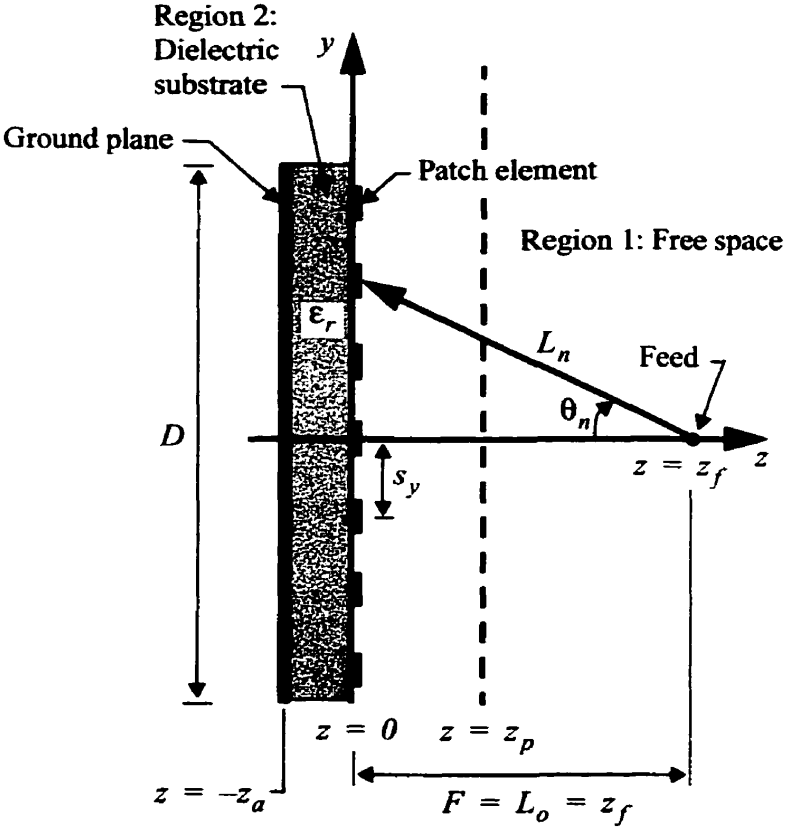

Fig. 3-2: Cross-section schematic of a line-source-fed single-layer microstrip reflectarray with an x-polarized $\hat{E}$ field from the line-source. $\theta_n = \theta_i$ for the infinite periodic array simulations.

3.1.2 Phase Formulation

For a given beam direction, the line-source-fed microstrip reflectarray has a constant phase Ψ_c at a projected aperture plane in front of it, which is stated as

$$\Psi_c = -\psi_i + \psi_R + \beta_o = 2\pi\aleph + \beta_o\,; \qquad \aleph = 0, \pm 1, \pm 2, \ldots \tag{3-19}$$

where, with reference to Fig. 3-1 and Fig. 3-2, ψ_i is the phase delay due to the extension of the path length L_n, from the feed position $z = z_f$ on the z-axis to the n-th patch on an array column, ψ_R is the reflection coefficient phase of the pertaining n-th patch, and β_o is the progressive element phase difference along the y-direction, as required for the array to reflect an off-broadside beam. That is, for a broadside beam, $\beta_o = 0$.

3.1.3 Field Formulation

With the feed blockage neglected, and assuming that the aperture phase error is negligibly small, a scalar rectangular component (either x-, y- or z- component) of the far-field $\vec{E}$ at an observation point $P(r, \theta, \phi)$ for the reflectarray is derived from the aperture field formulations of [94] as

$$E^{(\mathrm{ra})}_{\mathrm{comp}}(r, \theta, \phi) \approx \frac{jk_o}{4\pi r} e^{-jk_o r}(1 + \cos\theta)\, s_x\, s_y\, E^{(\mathrm{ap})}_{MN,\,\mathrm{comp}}(\theta, \phi), \tag{3-20}$$

where

$$E^{(ap)}_{MN,\,comp}(\theta,\phi) = \sum_m \sum_n R_{n,\,comp}\, E^{(fd)}_{mn,\,comp}\, e^{j[\psi_{mn}(\theta,\phi)+\beta_o]} \tag{3-21}$$

for an $M \times N$-element patch array, assuming an adequately large array size. M and N are the number of elements in each column and row in the array, respectively, with the (m, n) indices representing the (m, n)-th patch on the array. $R_{n,\,comp}$ is the reflection coefficient, corresponding to the $\hat{E}$ field component, of the n-th patch along each column, which is approximated through the infinite periodic array modelling similar to [2][91]. $E^{(fd)}_{mn,\,comp}$ is the corresponding scalar component of the $\hat{E}$ field feed illumination of the (m, n)-th patch, $\psi_{mn}(\theta, \phi)$ is the phase of the planar array factor for the patch array to reflect a broadside beam, β_o is as defined in (3-19), k_o is the free-space propagation constant, and, s_x and s_y are the array element spacings in the x- and y- directions, respectively. Relating (3-19) to (3-20) and (3-21), $-\psi_i$ and ψ_R of (3-19) are the phases of $E^{(fd)}_{mn,\,comp}$ and $R_{n,\,comp}$, respectively.

The far-field radiation patterns of the reflectarray are obtained through a rectangular-to-spherical coordinate transformation of (3-20), as

$$\begin{bmatrix} E^{(ra)}_{\theta} \\ E^{(ra)}_{\phi} \end{bmatrix} = \begin{bmatrix} cos\theta cos\phi & cos\theta sin\phi & -sin\theta \\ -sin\theta & cos\phi & 0 \end{bmatrix} \begin{bmatrix} E^{(ra)}_{x} \\ E^{(ra)}_{y} \\ E^{(ra)}_{z} \end{bmatrix}, \tag{3-22}$$

where $E_{\theta}^{(ra)}$ and $E_{\phi}^{(ra)}$ are spherical components of the reflectarray far-field, while $E_{x}^{(ra)}$, $E_{y}^{(ra)}$ and $E_{z}^{(ra)}$ are rectangular components evaluated from (3-20). The directive gain, D_g, and the HPBW, are then easily computed from (3-22).

3.1.4 Patch Array Symmetry

For a center-fed reflectarray configuration, computations are necessary only for a quarter section of the $M \times N$-element patch array due to symmetry. This enhances computation speed and efficiency.

So, with reference to (3-21),

$$e^{j[\psi_{mn}(\theta,\phi)+\beta_o]} = e^{j\psi_m(\theta,\phi)} e^{j\psi_n(\theta,\phi)} e^{j\beta_o}, \tag{3-23}$$

where $\psi_m(\theta, \phi)$ and $\psi_n(\theta, \phi)$ are phases of the planar array factor in the x- and y- directions, respectively, for a broadside beam. Then, (3-21) is simplified to

$$E_{MN,\,\mathrm{comp}}^{(ap)}(\theta, \phi) = \sum_m \sum_n I_{mn} f_m f_n, \tag{3-24}$$

where

$$f_n = \begin{cases} e^{j\psi_n(\theta,\phi)} & ; \text{ for } n = 0 \\ 2\cos[\psi_n(\theta, \phi)] & ; \text{ for } n = 1, 2, 3, \ldots \end{cases} \tag{3-24a}$$

and

$$I_{mn} = R_n E_{mn}^{(fd)} e^{j\beta_o} \quad ; \quad \text{for } m, n = 0, 1, 2, \ldots . \tag{3-24b}$$

These formulations are implemented into the computer code for reflectarray far-field radiation analysis.

3.2 REFLECTION PHASE PROPERTIES

For the purpose of this study, the line-source is assumed to possess adequate frequency band, so that the bandwidth characteristics of the reflectarray is not affected by its feed. However, its size, being constant, influences its radiation patterns, and thus, the spillover losses of the reflectarray.

The feed is a 24-element co-linear array of uniformly excited, x-polarized, half-wavelength dipoles, which are placed a quarter-wavelength from a finite ground plane. The element separation of this co-linear array is $d_x = 2.16$cm (i.e. $d_x = 0.848\lambda$ at frequency $f = 11.761$GHz). The feed is centered at location $(x, y, z) = (0, 0, 15)$cm, parallel to the x-axis illustrated in Fig. 3-1 and Fig. 3-2. Here, $z = z_f = 15$cm is assumed to be the "focal" length F of the reflectarray. For the sake of simplicity, however, no feed blockage is included in the analysis.

The patch array is symmetrically centered at the origin on the xy-plane shown in Fig. 3-1. It consists of a 41×31 -element array of single-layer rectangular microstrip patches. The patch widths and element separations are fixed as $b = 0.75$cm and $s_x = s_y = 1.25$cm, respectively, while the patch lengths, a, within a column are individually varied to achieve a collimated beam at broadside. Because of the line-source feed, all 41 columns are identical.

Therefore, with reflectarray dimension in the y-direction $D = 40.0$cm, the reflectarray F/D ratio is 0.375.

3.2.1 General Simulation Parameters

In determining the phase delay ψ_i, a uniform TE-to-z two-dimensional incident plane wave is assumed. An incident angle $\theta_i = \theta_n$ is also assumed, where θ_i and θ_n are schematically defined in Fig. 3-1 and Fig. 3-2. For the reflection coefficient computations, the reflection reference plane is chosen as $z = z_p = 0.5\lambda_o$, where λ_o is the free space wavelength.

Two arrays are designed using single-layer rectangular microstrip patches on two different substrates, namely, a thin $\varepsilon_r = 2.5$ substrate with a thickness of $z_a = 0.0798$cm, and a thick foam substrate ($\varepsilon_r = 1.03$) with a thickness of $z_a = 0.5$cm. Appropriate patch lengths are selected for a given incident angle $\theta_n = \theta_i$, such that a constant phase Ψ_c is

achieved, satisfying (3-19), with $\beta_o = 0$ for a broadside beam. This requires that the patch length a be deviated from its resonant length a_o, so that a corresponding phase ψ_{Rn} is achieved [7]. The resulting corrected patch length is a_n. The length deviation from the resonant length, designated as $\delta = a - a_o$, is employed as a normalized resonant patch length deviation δ / a_o.

In an infinite periodic array, the resonant patch length at center frequency $f_o = 11.761$GHz for the thin substrate ($\varepsilon_r = 2.5$ and $z_a = 0.0798$cm) is $a_o = 0.75$cm. For the thick substrate ($\varepsilon_r = 1.03$ and $z_a = 0.5$cm), it is $a_o = 1.08$cm. The array dimensional parameters for these substrates are summarized in Table 3-1.

Table 3-1: Infinite periodic array dimensional parameters for two selected substrates, with $f_o = 11.761$GHz, $\lambda_o = 2.5508$cm and $\lambda_d = \lambda_o / \sqrt{\varepsilon_r}$.

Substrate case	z_a (cm)	z_a/λ_d	a_o (cm)	a_o/λ_d	s_x (cm)	s_x/λ_d
$\varepsilon_r = 2.5$ ($\lambda_d = 1.6133$cm)	0.0798	0.0495	0.75	0.4649	1.25	0.7748
$\varepsilon_r = 1.03$ ($\lambda_d = 2.5134$cm)	0.5000	0.1989	1.08	0.4297	1.25	0.4973

3.2.2 Reflection Phase Curves

For both thin and thick substrates, through the infinite periodic array analysis, Fig. 3-3 indicates that their TE-to-z reflection coefficient phases ψ_R increase with increasing incident angle θ_i. From Fig. 3-3(a), ψ_R for the thin substrate varies rapidly in the vicinity of its resonant length a_o. This is even more rapid when the incident angle is larger. Consequently, the bandwidth for this case is relatively narrow as compared to that for the case of the thick substrate, depicted in Fig. 3-3(b). For the latter case, the patch length can be increased only slightly from its resonant length $a_o = 1.08\text{cm}$, as it is close to the unit cell size $s_x = 1.25\text{cm}$.

In designing a microstrip reflectarray, the normalized resonant patch length deviation δ/a_o may be obtained directly from Fig. 3-3, from which the required patch length a_n can be determined.

3.2.3 Unattainable Reflection Phase Range

The reflection phase curves of Fig. 3-3(a), for the thin substrate, span almost the entire $360°$ phase range. On the contrary, at small incident angles θ_i, the phase curves of Fig. 3-3(b), for the thick substrate, cover only approximately one half of the entire phase range. As such, the rest of the phase range remains unattainable at these small angles.

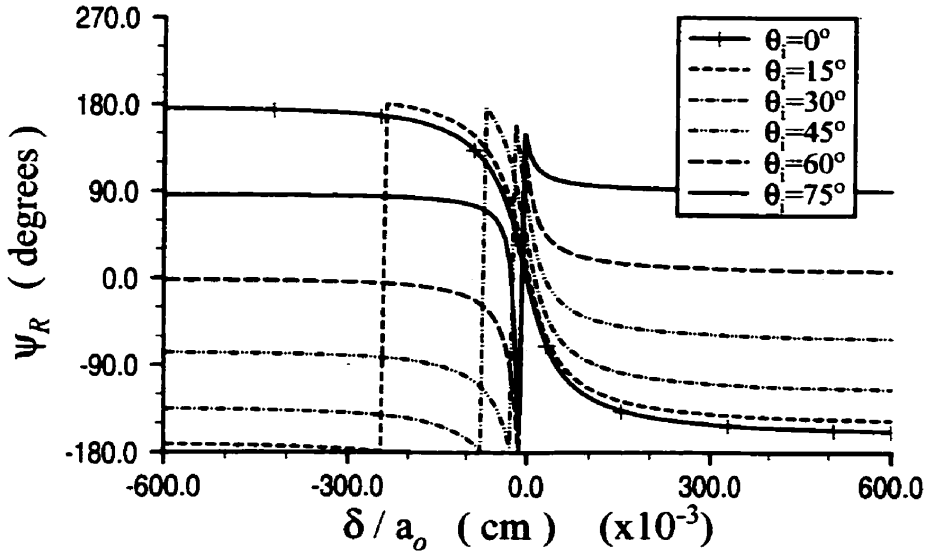

(a)

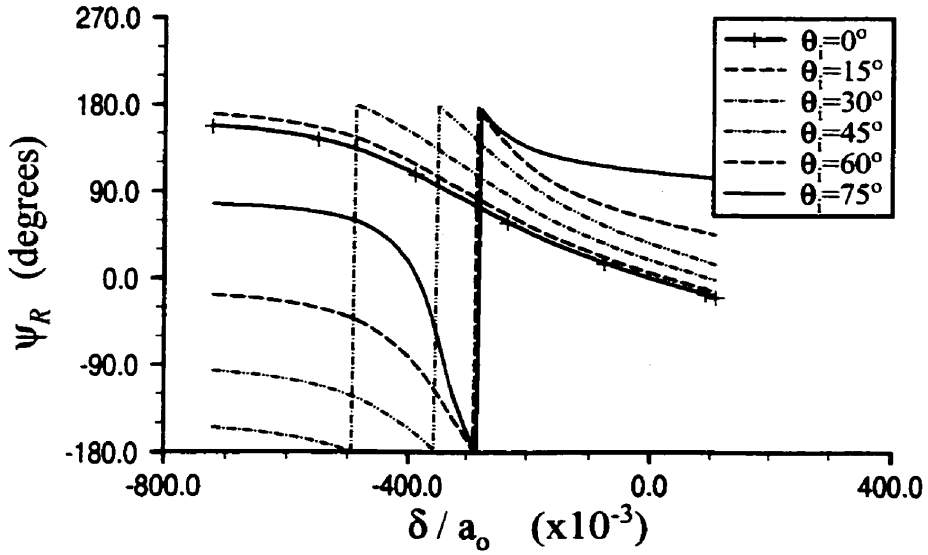

(b)

Fig. 3-3: TE-to-z reflection phase curves due to patch length and incident angle, for rectangular microstrip patch at f = *11.761*GHz: (a) ε_r = *2.5*, z_a = *0.0798*cm and a_o = *0.75*cm, and (b) ε_r = *1.03*, z_a = *0.5*cm and a_o = *1.08*cm. b = *0.75*cm for both cases.

The physical sizes of the microstrip patches, for the purpose of this study, are limited to the dimensions $0.3\text{cm} \leq a \leq 1.2\text{cm}$, for both thin and thick substrates. By selecting δ/a_o values at both ends of the curves in Fig. 3-3(a), i.e. at $a = 0.3\text{cm}$ and $a = 1.2\text{cm}$, the phase curves are replotted as a function of incident angle θ_i, defining the unattainable reflection phase range in Fig. 3-4(a). Similarly, the curves in Fig. 3-3(b) are used to obtain those in Fig. 3-4(b), which define a large unattainable reflection phase range. These unattainable reflection phase ranges are only asymptotic values based on the smallest and largest patch lengths utilized. Fig. 3-3 and Fig. 3-4 also indicate that ψ_R for very small δ/a_o generally lags that for which δ/a_o is very large.

For simplicity, the size of the unattainable reflection phase range, also known as the reflection phase gap, is denoted by $\Delta\psi_R$. Fig. 3-5 compares the reflection phase gaps for a number of substrate cases. Also for comparisons, the reflection phase gap is approximated [7] using the path length expression $2\Gamma^{(I)}z_a$, which represents the electrical path length due to substrate thickness, where $\Gamma^{(I)} = k_o \cos\theta_i$, and k_o is the propagation constant in free space.

Fig. 3-5 demonstrates, that, $\Delta\psi_R$ is generally larger for a thick substrate with low permittivity. Moreover, the patch size for each of these thick substrates is practically restricted by the available space within the unit cell of the array, thus, limiting its attainable reflection phase range.

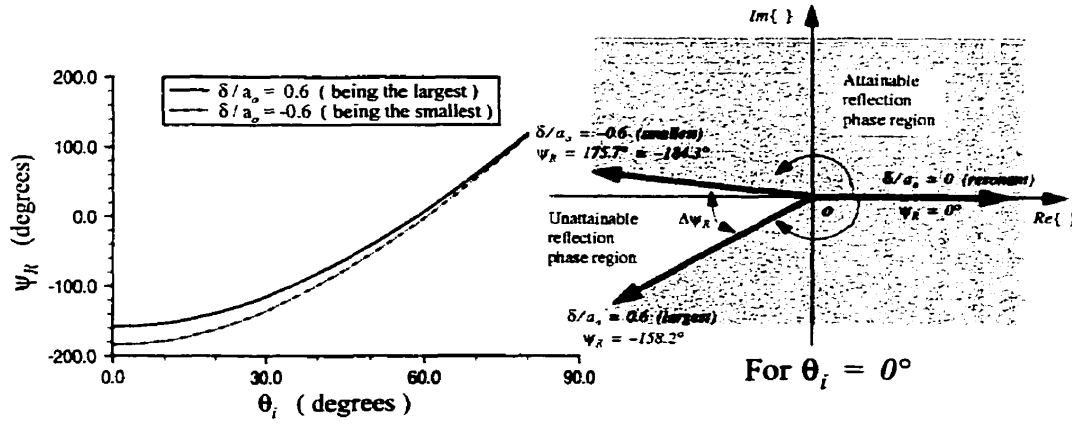

(a)

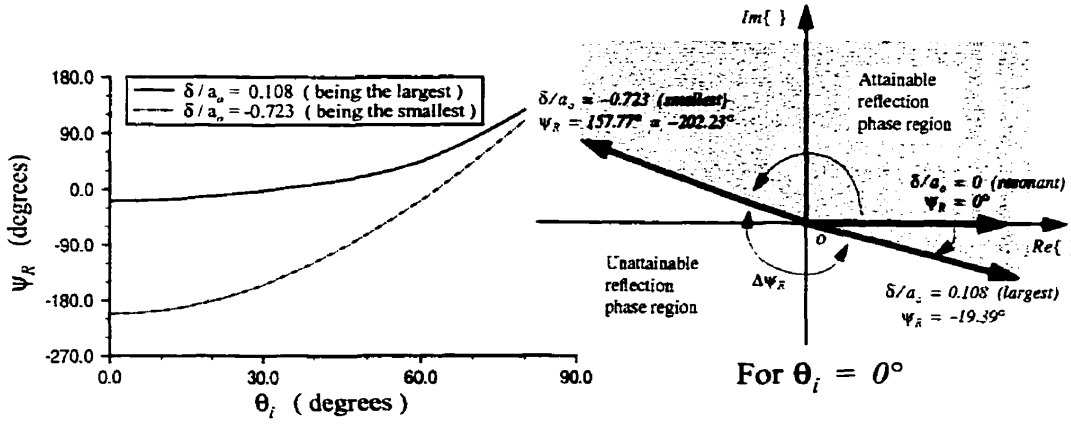

(b)

Fig. 3-4: Unattainable phase ranges due to incident angle, for rectangular microstrip patches at $f = 11.761$GHz, and their corresponding phase diagrams: (a) $\varepsilon_r = 2.5$, $z_a = 0.0798$cm and $a_o = 0.75$cm, and (b) $\varepsilon_r = 1.03$, $z_a = 0.5$cm and $a_o = 1.08$cm. $b = 0.75$cm for both cases.

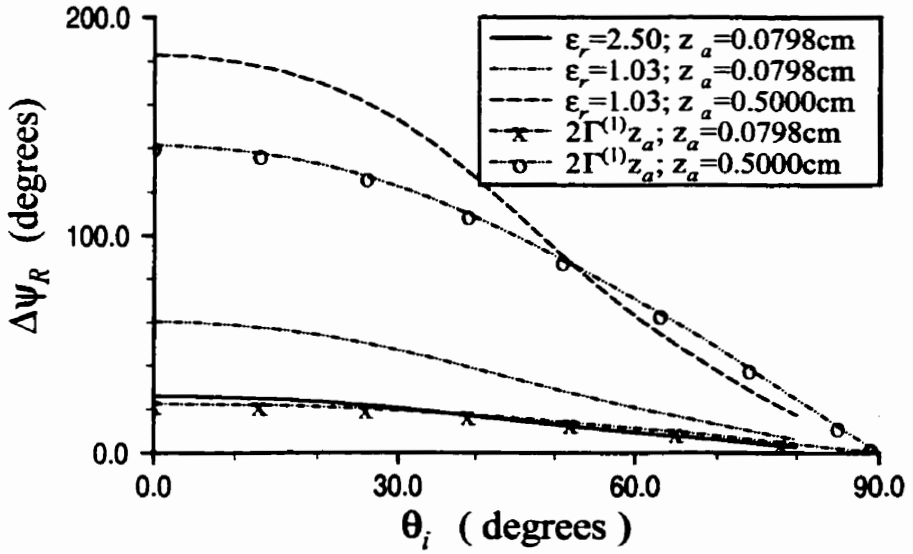

(a)

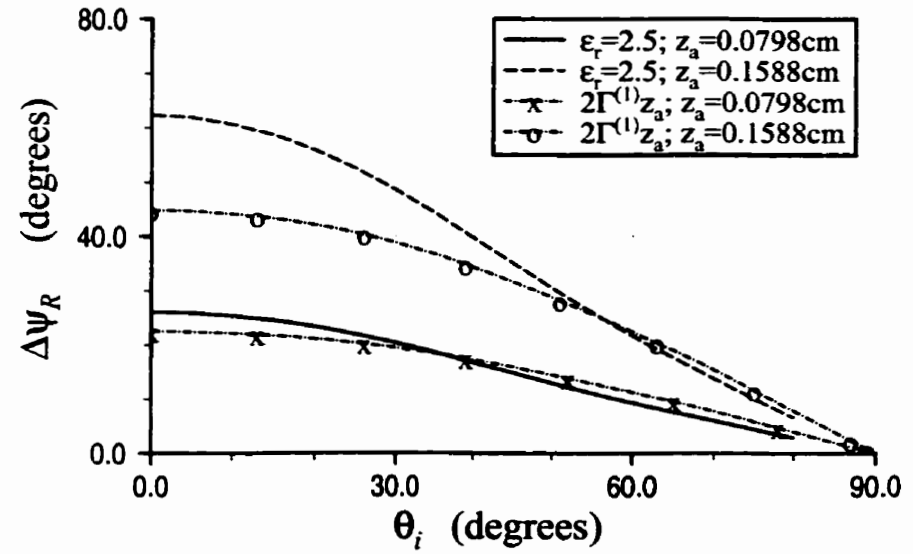

(b)

Fig. 3-5: Comparisons of the reflection phase gaps for various substrates at f = *11.761*GHz, for rectangular microstrip patch: (a) between two different substrate permittivities, and (b) between two different substrate thicknesses. The last two curves are evaluated from an empirical approximation [7].

From these results, the reflection coefficient phase appears less sensitive to patch length at normal incidence, thus, resulting in the widest bandwidth. Unfortunately, this also appears to result in the largest reflection phase gap. Nonetheless, the reflection phase gap can be decreased by reducing substrate thickness, and increasing substrate permittivity. Consequently, its bandwidth is also decreased.

It should be noted, that, with the exception of the $\varepsilon_r = 2.5$ substrate, where $z_a = 0.0798$cm, the reflection phase curves for all the cases shown in Fig. 3-5 are shifted towards either side of the $\delta/a_o = 0$ value, similar to that in Fig. 3-3(b). These "asymmetric" reflection phase curves generally produce large reflection phase gaps, resembling those in Fig. 3-5.

3.3 Effects of Phase Correction Errors

The problem of phase errors is a primary concern in the design of a microstrip reflectarray. Large phase errors would significantly degrade the performance of the reflectarray. In general, these phase errors emerge as a result of several factors, namely, (i) the existence of unattainable reflection phase range [7], (ii) frequency scanning within the required band, and (iii) finite sizes of microstrip patches, which introduce phase quantization errors that increase with increasing subtended angle θ_n [83].

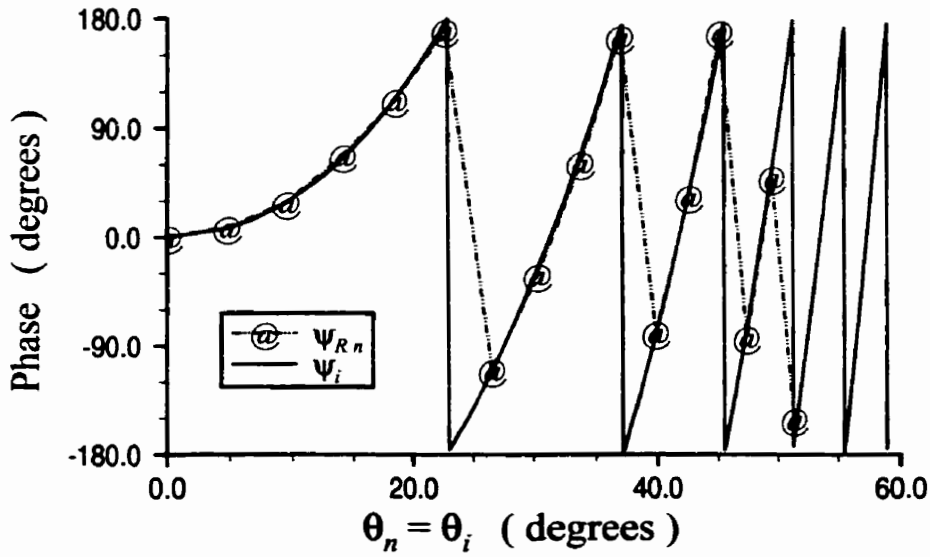

(a)

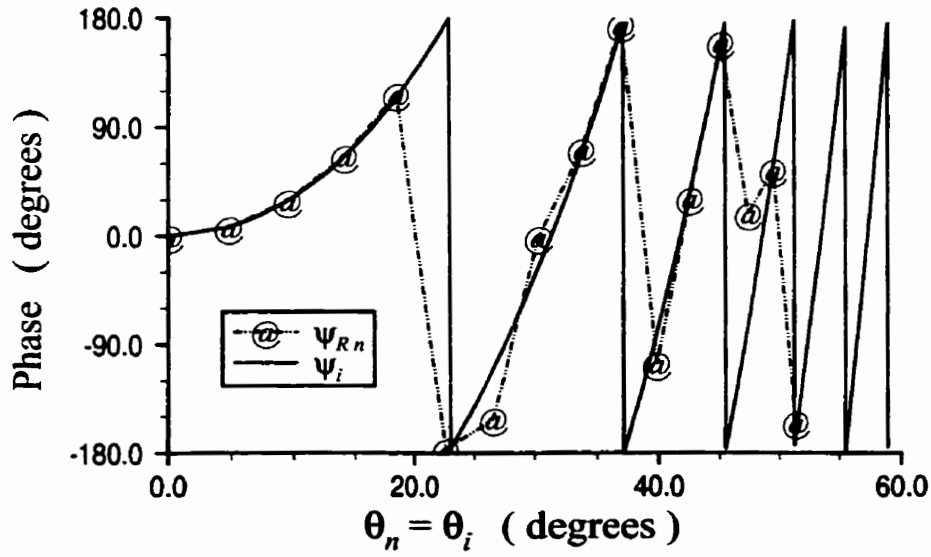

(b)

Fig. 3-6: Phase delays ψ_i and achieved phases ψ_{Rn}, evaluated at $f = 11.761$GHz, at respective patch locations in a column, for rectangular microstrip patches: (a) for thin substrate, with $\varepsilon_r = 2.5$ and $z_a = 0.0798$cm, and (b) for thick substrate, with $\varepsilon_r = 1.03$ and $z_a = 0.5$cm. $b = 0.75$cm for all cases.

3.3.1 Phase Correction Errors

Fig. 3-6 (a) and (b) compares the required reflectarray phase correction $\psi_n = \psi_i$, where ψ_i is as previously defined for (3-19), with the achieved phase ψ_{Rn}, for the thin and thick substrates of Fig. 3-4. The phase correction errors and patch lengths, at some selected locations for both substrates, are listed in Table 3-2. In this table, the corrected patch length a_n is obtainable from Fig. 3-7, i.e. through $a_n = a_o(1 + \delta_n/a_o)$.

Table 3-2: A sample of corrected patch lengths (for rectangular patches only), a_n, and their corresponding phases, ψ_{Rn}, achieved at their respective patch locations within a column. ψ_n is the required phase correction, $|\Delta\psi_{Rn}| = |\psi_{Rn} - \psi_n|$ is the phase correction error and $f = 11.761$GHz.

n-th patch ($\theta_n = \theta_i$)	$\psi_n = \psi_i$	$\varepsilon_r = 2.5$ with $z_a = 0.0798$cm			$\varepsilon_r = 1.03$ with $z_a = 0.5000$cm		
		ψ_{Rn}	a_n (cm)	$\lvert\Delta\psi_{Rn}\rvert$	ψ_{Rn}	a_n (cm)	$\lvert\Delta\psi_{Rn}\rvert$
0 (0.00^o)	0.00^o	-0.01^o	0.7500	0.01^o	-0.17^o	1.0830	0.17^o
±1 (4.76^o)	7.34^o	7.97^o	0.7480	0.63^o	7.04^o	1.0470	0.30^o
±2 (9.46^o)	29.22^o	28.67^o	0.7430	0.55^o	28.93^o	0.9540	0.29^o
±6 (26.57^o)	-109.95^o	-109.80^o	0.8810	0.15^o	-151.83^o	0.3000	41.88^o
±7 (30.26^o)	-25.91^o	-31.21^o	0.7710	5.30^o	-1.11^o	1.1920	24.80^o
±10 (39.81^o)	-80.84^o	-78.96^o	1.0000	1.88^o	-106.04^o	0.3000	25.20^o
±13 (47.29^o)	-75.18^o	-82.91^o	0.6600	7.73^o	17.88^o	1.1920	93.06^o

The phase correction errors for the thick substrate, shown in both Fig. 3-6(b) and Table 3-2, are particularly large at subtended angles $\theta_n = 26.57°, 30.26°, 39.81°$ and $47.29°$. At each of these discrete patch locations, $\psi_n = \psi_i$ falls within the unattainable reflection phase range of Fig. 3-4(b).

For the thin substrate in Fig. 3-6(a), however, none of the $\psi_n = \psi_i$ values at the same discrete locations lies within its corresponding unattainable reflection phase range shown in Fig. 3-4(a). Thus, the phases achieved through the corrected patch lengths a_n are relatively accurate, and phase correction errors are negligible. Also, for this case, the patch array consists of mostly near-resonant patches.

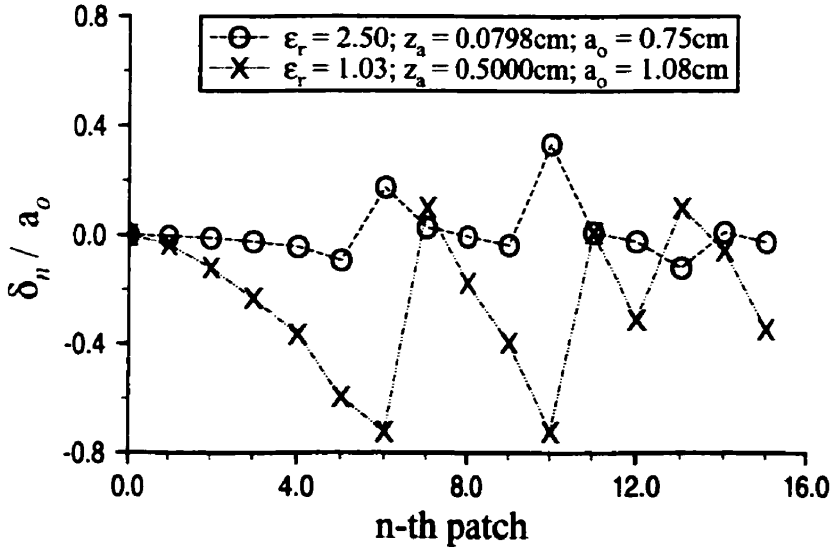

Fig. 3-7: Normalized resonant patch length deviations δ_n/a_o for both thin and thick substrates, evaluated at $f = 11.761$GHz, at respective patch locations in a column, for rectangular microstrip patches. $b = 0.75$cm for all cases.

3.3.2 Far-field Radiation Characteristics

For simplicity, the line-source is assumed to have larger bandwidths than the patch array of the reflectarray. Radiation characteristics of the reflectarray are then investigated independently. For a 41×31 -element patch array, the ideal directivity without phase correction error, and the spillover loss, are shown in Table 3-3. The spillover loss in the table is computed, in percentage, as the total power radiated from feed, less the total power radiated by the ideal patch array for no phase correction error. As expected, the directivity increases, and the spillover loss decreases, with increasing frequency.

Table 3-3: Patch array dimensions for 41×31 elements, ideal directivities without phase correction errors, and reflectarray spillover losses, over a *10.2%* frequency bandwidth for a constant feed size.

	Frequency, f (GHz)				
	11.161	*11.561*	*11.761*	*11.961*	*12.361*
Patch array dimension along the x-direction, $41s_x$ (λ)	*19.067*	*19.750*	*20.092*	*20.433*	*21.117*
Patch array dimension along the y-direction, $31s_y$ (λ)	*14.933*	*14.675*	*15.191*	*15.450*	*15.708*
Ideal D_o (dBi)	*34.76*	*35.12*	*35.28*	*35.43*	*35.72*
Spillover loss (percent)	*12.58*	*10.99*	*10.41*	*9.83*	*9.02*

Based on these assumptions, the reflectarray far-field patterns are computed using (3-20)-(3-24) and illustrated in Fig. 3-8. The thick substrate produces relatively stable H-plane($\phi = 90^o$) directive gains D_g over a *3.4%* frequency bandwidth, as compared to the thin substrate. However, for very narrowband applications (for bandwidths of less than *3.4%*), the thin substrate provides a better radiation performance, due to its minimal phase correction errors.

Table 3-4 summarizes the radiation properties of these reflectarrays, while Fig. 3-9 graphically shows their directivities D_o, over a selected *10.2%* frequency bandwidth. These designs also produce negligibly low cross-polarization levels in both E- and H- planes ($\phi = 0^o$ and $\phi = 90^o$, respectively), i.e. more than *45* dB down.

Large phase correction errors in the thick substrate reflectarray, shown in both Fig. 3-6(b) and Table 3-2, contribute to its degradation in directivity and side-lobe levels (SLL) in the H-plane ($\phi = 90^o$), at center frequency $f_o = 11.761$GHz, as observed in both Fig. 3-8(b) and Table 3-4. These high SLL, attributed to the large phase correction errors, are in accordance with [95].

For the thin substrate, however, as the frequency scans away from the center frequency f_o, the phase correction errors increase rapidly. Hence, as illustrated in Fig. 3-8(a), both directivity and SLL in the H-plane ($\phi = 90^o$) for this case are degraded significantly over

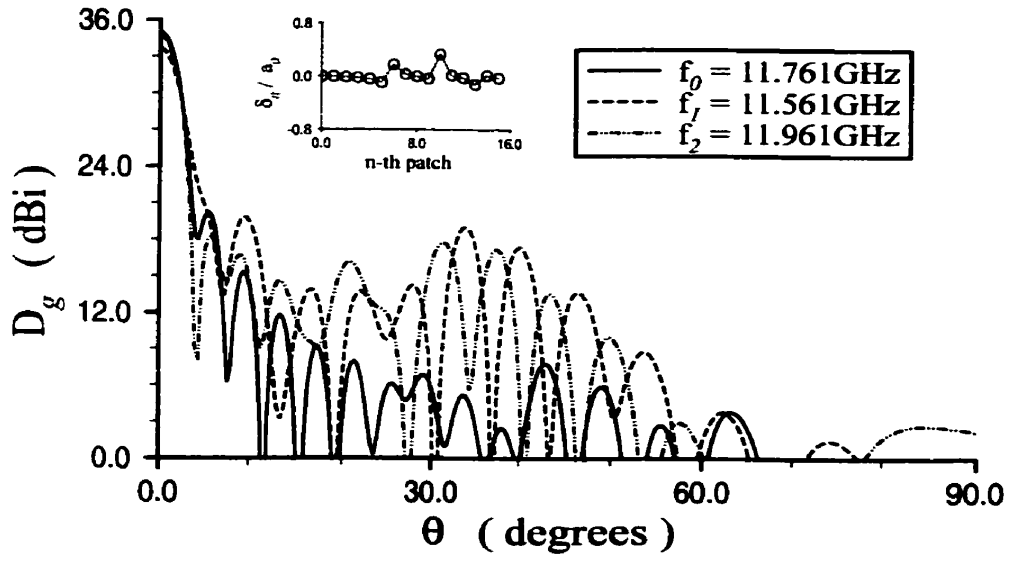

(a)

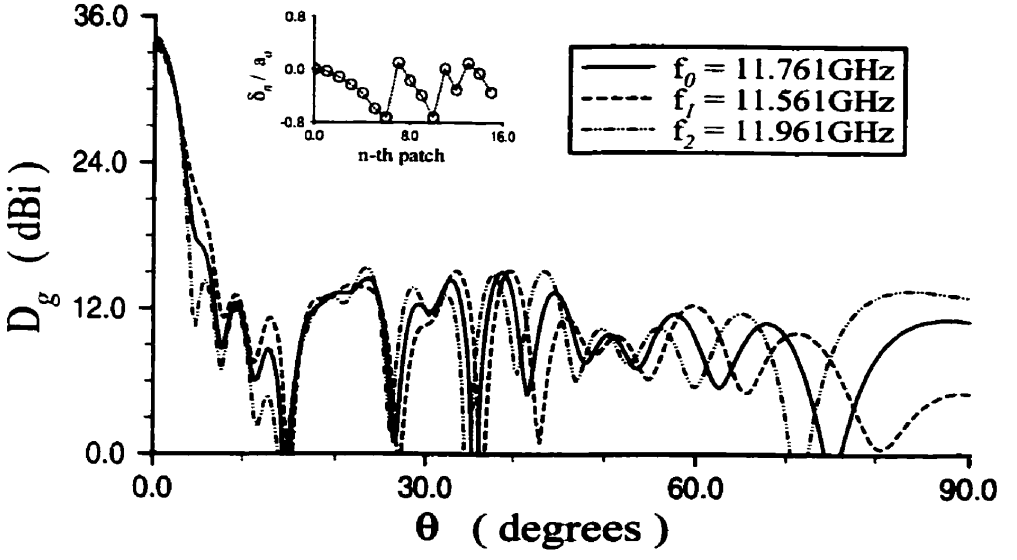

(b)

Fig. 3-8: Reflectarray directive gain patterns D_g in the H-plane ($\phi = 90^o$), evaluated over a *3.4%* frequency bandwidth, for the 41×31 -element rectangular microstrip patch arrays: (a) thin substrate, with $\varepsilon_r = 2.5$, $z_a = 0.0798$cm and $a_o = 0.75$cm, and (b) thick substrate, with $\varepsilon_r = 1.03$, $z_a = 0.5$cm and $a_o = 1.08$cm. $b = 0.75$cm for both cases.

Table 3-4: Reflectarray H-plane ($\phi = 90^o$) radiation properties over a *10.2%* frequency bandwidth for the thin and thick substrates. Patch arrays are consist of 41×31 elements, and the ideal patch array for no phase correction error is evaluated at $f = 11.761$GHz.

Substrate case	Radiation properties	Ideal patch array	Frequency, f (GHz)				
			11.161	*11.561*	*11.761*	*11.961*	*12.361*
$\varepsilon_r = 2.5$, $z_a = 0.0798$cm (rectangular patches only)	D_o (dBi)	*35.28*	*28.49*	*33.65*	*35.02*	*34.78*	*31.31*
	HPBW ($\phi = 90^o$)	*3.55°*	*6.92°*	*3.99°*	*3.61°*	*3.54°*	*4.11°*
	Max. SLL ($\phi = 90^o$) (dB)	*−16.16*	*−5.13*	*−13.76*	*−14.80*	*−16.46*	*−7.93*
	Loss in directivity (dB)	*0.0*	*6.27*	*1.46*	*0.26*	*0.65*	*4.41*
$\varepsilon_r = 1.03$, $z_a = 0.5000$cm (rectangular patches only)	D_o (dBi)	*35.28*	*31.84*	*33.39*	*33.92*	*34.26*	*34.37*
	HPBW ($\phi = 90^o$)	*3.55°*	*5.11°*	*4.09°*	*3.86°*	*3.72°*	*3.64°*
	Max. SLL ($\phi = 90^o$) (dB)	*−16.16*	*−16.38*	*−18.26*	*−18.89*	*−18.96*	*−16.71*
	Loss in directivity (dB)	*0.0*	*2.91*	*1.72*	*1.36*	*1.17*	*1.35*
$\varepsilon_r = 1.03$, $z_a = 0.5000$cm (combination of rectangular and hat-shaped patches)	D_o (dBi)	*35.28*	*32.87*	*34.36*	*34.86*	*35.17*	*35.20*
	HPBW ($\phi = 90^o$)	*3.55°*	*4.36°*	*3.77°*	*3.61°*	*3.50°*	*3.45°*
	Max. SLL ($\phi = 90^o$) (dB)	*−16.16*	*−13.62*	*−15.75*	*−16.29*	*−16.65*	*−14.48*
	Loss in directivity (dB)	*0.0*	*1.88*	*0.75*	*0.42*	*0.26*	*0.52*

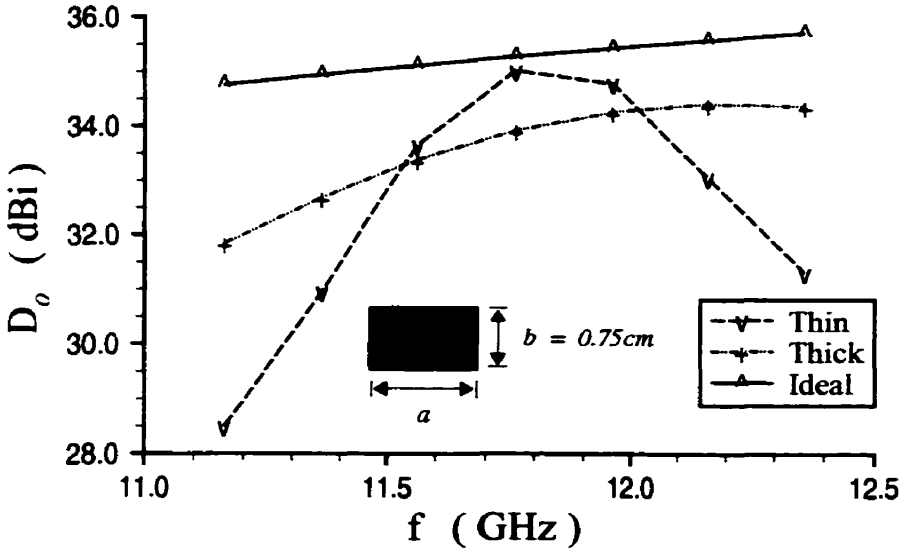

Fig. 3-9: Reflectarray directivities D_o over a *10.2%* frequency bandwidth, for the 41×31-element rectangular microstrip patch arrays on thin and thick substrates. $\varepsilon_r = 2.5$ and $z_a = 0.0798$cm for thin substrate, $\varepsilon_r = 1.03$ and $z_a = 0.5$cm for thick substrate, whereas the ideal patch array has no phase correction error.

the *3.4%* frequency bandwidth. On the other hand, for the thick substrate, due to its wide-band properties, both directivity and SLL in the H-plane ($\phi = 90^o$) remain relatively stable throughout the bandwidth, as evident in Fig. 3-8(b). These radiation characteristics are illustrated in Fig. 3-9 for the directivity.

3.3.3 Multiple Patch Geometries for Enhanced Performance

Fig. 3-10 shows the average current distributions (in full color) of both single-element rectangular and single-element hat-shaped microstrip patches, as simulated using a commercially available Method of Moment (MoM) software, the *Zeland IE3D* version 6.0 [96]. Since $\hat{E}$ is x-directed, these are also approximately the x-directed current distributions. The rectangular patch is resonant at frequency $f = 11.761\text{GHz}$. For the new hat-shaped patch, there is a slight difference in current intensities between the top and bottom edges. This creates the wideband characteristics similar to the concept of producing two near equal-magnitude resonant modes at adjacent frequencies, as investigated in [97]-[99].

To include the analysis of stub attachments at the edge of rectangular patches using the infinite periodic array analysis presented in Chapter 2, an additional subsectional patch segmentation scheme [93] is implemented into the computer code, in conjunction with roof-top basis functions already utilized. This is particularly essential for analyzing the reflection phase properties of the hat-shaped patch for the reflectarray.

Fig. 3-11(a) compares the TE-to-z reflection coefficient phase behaviors of different infinite array microstrip patch geometries on the thick substrate ($\varepsilon_r = 1.03$ and $z_a = 0.5\text{cm}$) at normal incidence. Of all the geometrical dimensions shown in the figure, only patch length a is varied. This produces a reflection phase curve for the hat-shaped

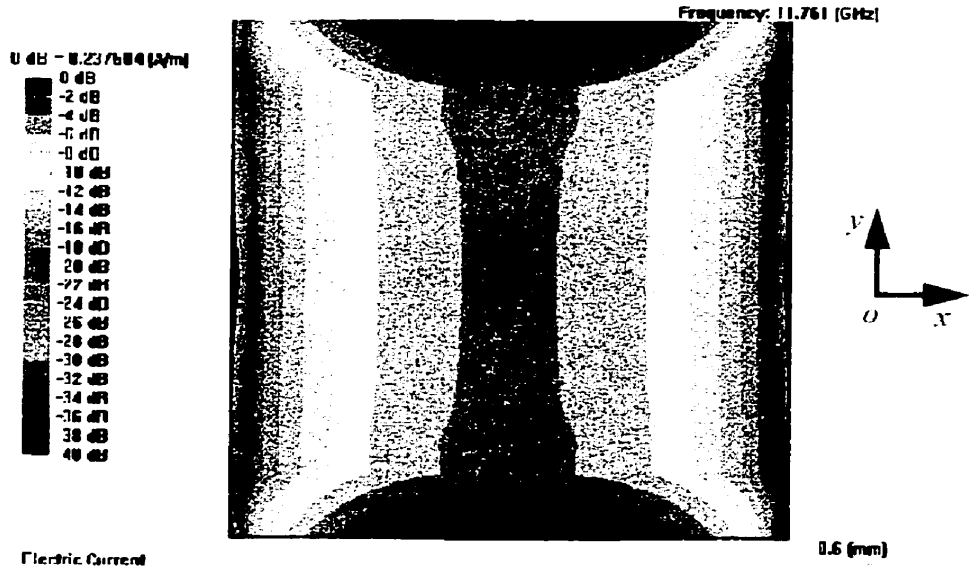

(a)

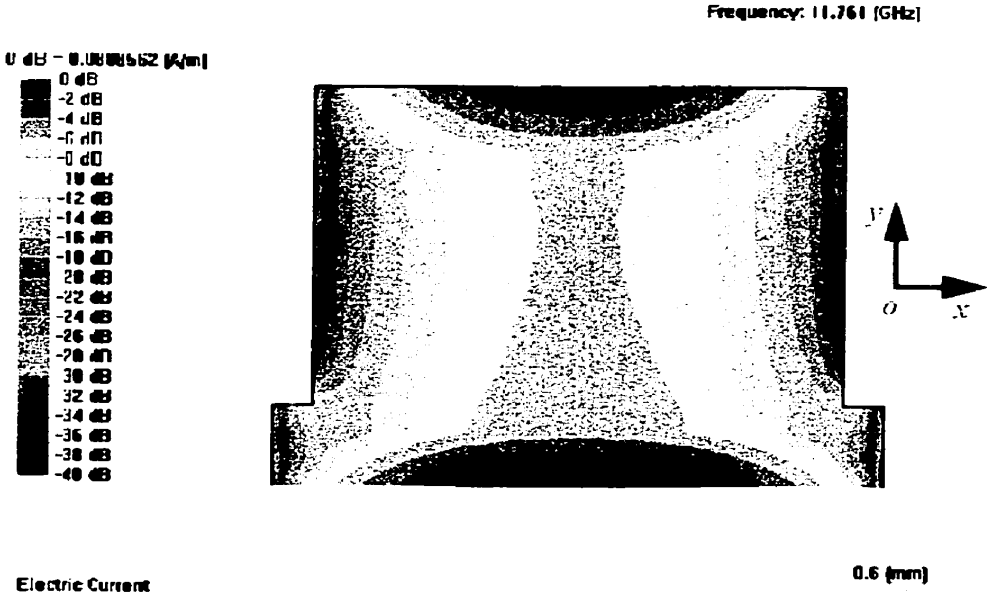

(b)

Fig. 3-10: Average current distributions of single-element microstrip patches for a normal incidence TE-to-z plane wave: (a) resonant rectangular patch, with $a = b = 0.75$cm, and (b) hat-shaped patch, with $a = 0.75$cm, $b = 0.54$cm, $l_s = 0.05$cm and $w_s = 0.11$cm. The $\hat{E}$ field is x-directed, with $f = 11.761$GHz, $\varepsilon_r = 2.5$ and $z_a = 0.0798$cm.

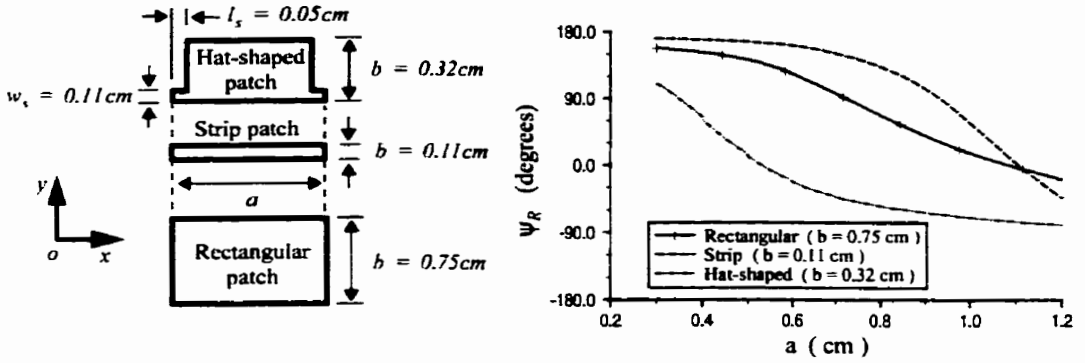

(a)

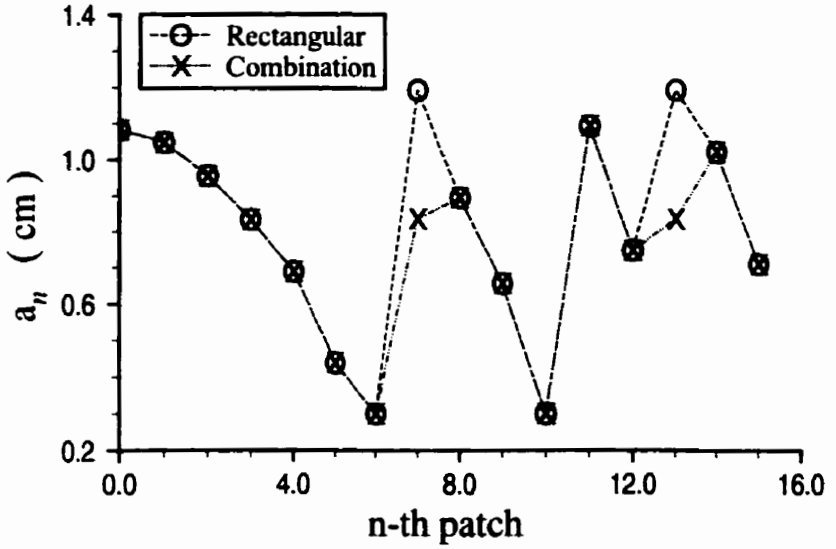

(b)

Fig. 3-11: Effects of different microstrip patch geometries for thick substrate, $\varepsilon_r = 1.03$ and $z_a = 0.5$cm, evaluated at $f = 11.761$GHz: (a) TE-to-z reflection phase curves due to patch length a, at normal incidence ($\theta_i = 0^o$), and (b) patch lengths a_n in a column for rectangular and combination patch arrays. The combination array consists of rectangular and hat-shaped patches mentioned in Table 3-5.

patch that encompasses part of the unattainable phase range of the rectangular and strip patches.

In a single-layer microstrip reflectarray, a hat-shaped patch can thus substitute a rectangular patch at a location where the required phase correction ψ_n coincides with its unattainable phase range, as mentioned in [85], resulting in a combination patch array. For these locations, the infinite periodic arrays utilized in the modelling comprise entirely of hat-shaped patches. Results thus obtained does not properly account for mutual coupling between patches of different geometrical shapes in the combination array. Nevertheless, they are generally accurate for the majority of array elements which are rectangular patches.

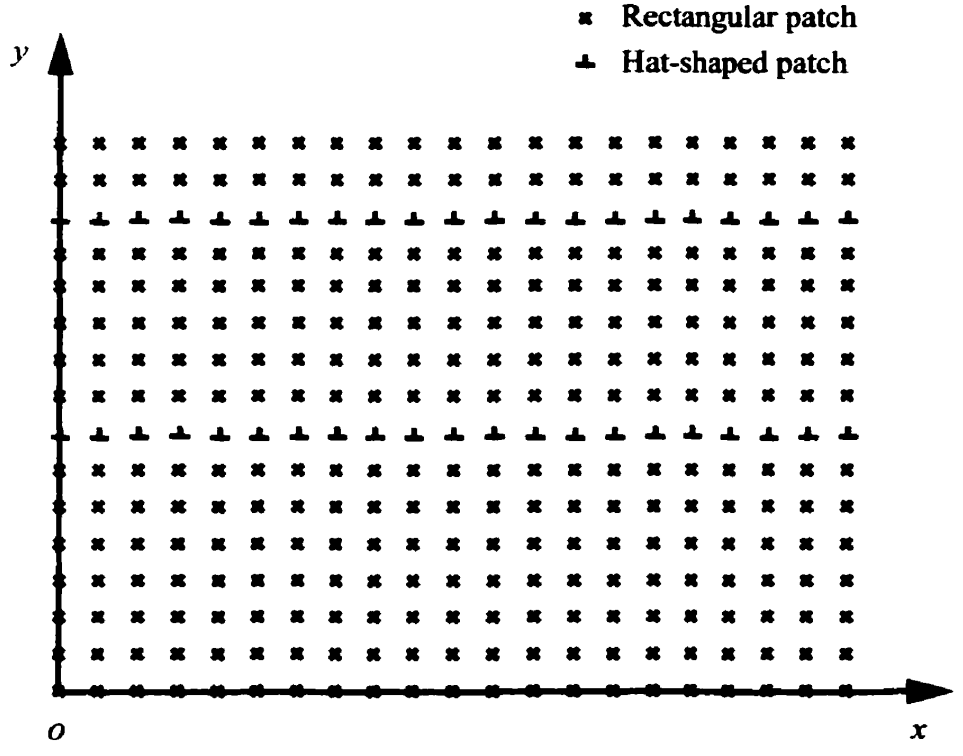

Fig. 3-12: Relative locations of rectangular and hat-shaped microstrip patches in the first quadrant of the combination array.

Fig. 3-12 depicts the relative locations of different patch geometries in the first quadrant of the combination array. Comparisons for the best achieved phases ψ_{Rn} between rectangular and hat-shaped patches, and their corresponding corrected patch lengths a_n, are presented in Table 3-5.

Table 3-5: Comparisons for the best achieved phases ψ_{Rn} between rectangular and hat-shaped patches at the unattainable phase range locations. ψ_n is the required phase correction, a_n is the corrected patch length, $|\Delta\psi_{Rn}| = |\psi_{Rn} - \psi_n|$ is the phase correction error and $f = 11.761$GHz.

n-th patch ($\theta_n = \theta_i$)	$\psi_n = \psi_i$	$\varepsilon_r = 1.03$ with $z_a = 0.5000$cm					
		Rectangular patches, $b = 0.75$cm			Hat-shaped patches, $b = 0.32$cm, $w_s = 0.11$cm and $l_s = 0.05$cm		
		ψ_{Rn}	a_n (cm)	$\lvert\Delta\psi_{Rn}\rvert$	ψ_{Rn}	a_n (cm)	$\lvert\Delta\psi_{Rn}\rvert$
± 6 (26.57^o)	-109.95^o	-151.83^o (Utilized)	0.3000	41.88^o	-53.84^o (Not utilized)	1.1924	56.11^o
± 7 (30.26^o)	-25.91^o	-1.11^o (Not utilized)	1.1920	24.80^o	-25.80^o (Utilized)	0.8348	0.11^o
± 10 (39.81^o)	-80.84^o	-106.04^o (Utilized)	0.3000	25.20^o	-25.10^o (Not utilized)	1.1924	55.74^o
± 13 (47.29^o)	-75.18^o	17.88^o (Not utilized)	1.1920	93.06^o	-11.83^o (Utilized)	1.1924	63.35^o

That is, the ± 7th and ± 13th rectangular patches, listed in Table 3-5, are replaced by hat-shaped patches, which produce more accurate phase corrections. The corrected patch lengths a_n are already graphically depicted in Fig. 3-11(b). The strip geometry, however,

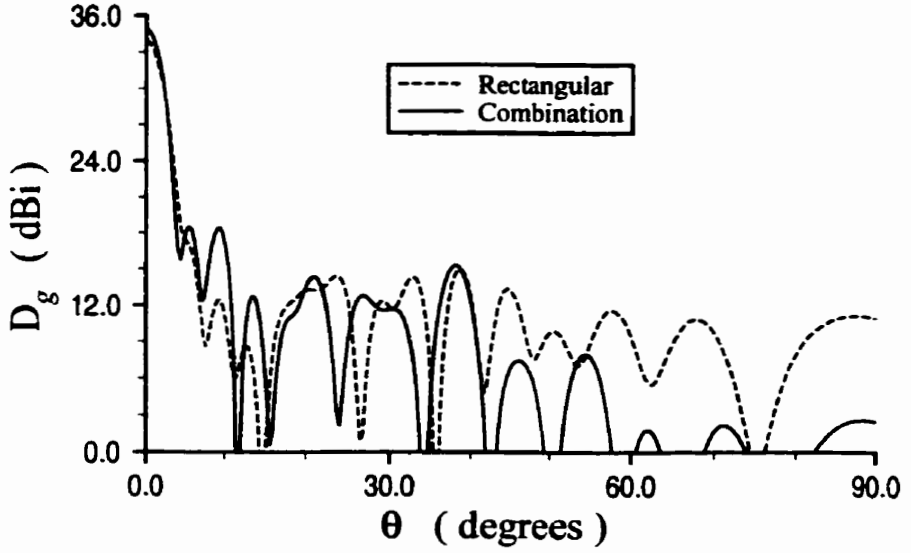

(a)

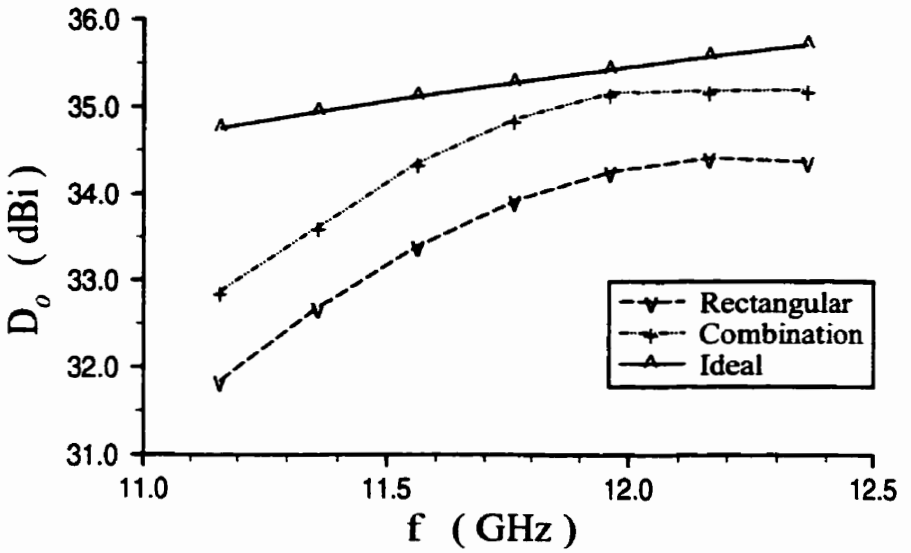

(b)

Fig. 3-13: Radiation characteristics of the 41×31-element rectangular and combination microstrip patch arrays on thick substrates, $\varepsilon_r = 1.03$ and $z_g = 0.5$cm: (a) reflectarray directive gain patterns D_g in the H-plane ($\phi = 90^0$) at center frequency $f_o = 11.761$GHz, and (b) reflectarray directivities D_o over a 10.2% frequency bandwidth. Patch dimensions are as shown in Table 3-5, and the ideal patch array has no phase correction error.

is not implemented, since it does not provide adequate phase correction, as compared to the hat-shaped geometry.

Reflectarray far-field patterns for both rectangular and combination patch arrays are illustrated in Fig. 3-13(a). The combination array shows improved SLL at large angles away from the main-lobe at the expense of initial SLL, which are slightly higher. These are also shown in Table 3-4, which also indicates an approximately *1*dB improvement in directivities over the selected *10.2%* frequency bandwidth. Fig. 3-13(b) illustrates these improved directivities over the bandwidth. Such results demonstrate closer similarities of the combination patch array to the ideal case for no phase correction error.

3.4 CONCLUSION

Reflection phase properties of single-layer microstrip reflectarrays are rigorously analyzed through the study of reflection phase curves obtained from the infinite periodic array analysis. The reflection phase dependence on substrate parameters and patch dimensions for the rectangular microstrip patches are also discussed in detail.

Phase correction errors, due to large unattainable reflection phase ranges, contribute to the degradation of directivity and SLL of the reflectarray. To remedy this, alternative patch geometries, such as the hat-shaped patches, are used to generate the required phase corrections in the unattainable reflection phase ranges. The resulting geometry, thus, becomes a combination of multiple patch geometries in the array. Although the infinite

periodic array modelling does not accurately account for mutual coupling between patches of different geometrical shapes, it is generally accurate for the combination array, since it consists mostly of rectangular patches.

Also, this study demonstrates how each selected substrate can generate the required phase corrections over a selected frequency band, such that a good radiation performance is achieved. In general, the reflectarray H-plane ($\phi = 90^o$) far-field radiation characteristics are more significantly affected by the reflection phase properties of its patch array. Therefore, careful array parameter selection is necessary for its superior performance.

The reflectarray with the thick substrate, considered here, causes poorer phase corrections due to its larger unattainable phase range, as compared to the thin substrate. However, the former exhibits more stable radiation characteristics over a wide bandwidth, as compared to the latter, which performs relatively well for very narrowband applications.

4 Some Essential Design Concepts

This chapter provides a further analysis of line-source-fed single-layer microstrip reflectarray discussed in Chapter 3. These include:

(i) novel formulations for simplications of the reflectarray modelling [86],

(ii) design restrictions by phase quantization errors [83], substrate thickness and permittivity [82],

(iii) properties of variable-stub-length patch arrays [81], and

(iv) line-source distribution schemes for improved reflectarray far-field radiation characteristics [84].

4.1 Empirical Formulation of Reflection Coefficient Phase

In the design of a microstrip reflectarray, the analysis for scattering from an infinite periodic array of microstrip patches is often utilized for determining the reflection coefficient phase angles [7]. The variation of this phase, due to variation in the patch size, is then used to compensate for the phase change in the incident wave, which is attributed to the change in its incident angle at discrete locations on the patch array. This phase correction results in a scattered field with a uniform phase front over the aperture of the reflectarray. A collimated beam is thus created.

In turn, a table of phase variation data, with respect to incident angles and patch sizes, is generally employed to determine the required patch size for proper phase correction. Since the problem must be solved individually for each patch, this can be costly for large reflectarrays. However, for symmetric reflectarrays, the geometrical symmetry for one quadrant of the array can be used to reduce computation. In fact, line-source feeds can simplify the problem to one dimension [84], i.e. for a column of the array. But for large arrays, the computation cost can still be significant.

This section proposes an empirical formulation for approximating the TE-to-z reflection coefficient phase with incident angle, for an infinite periodic array of single-layer rectangular microstrip patches. To verify the accuracy of this formulation, results are compared with those computed through the full wave analysis. Particularly, these results demonstrate the feasibility of implementing this formulation into the infinite array modelling of a line-source-fed reflectarray, which consists of single-layer rectangular microstrip patches, to avoid extensive CPU time. Furthermore, due to the simplicity of the empirical formulation, the reflection coefficient phase values can also be computed manually.

4.1.1 Novel Empirical Formulation

The geometry of an infinite periodic array of single-layer rectangular microstrip patches, illuminated by a TE-to-z plane wave, is illustrated in Fig. 4-1. For a given set of rectangular patch and cell dimensions, and constant azimuth angle ϕ, the empirical expression for approximating the TE-to-z reflection coefficient phase for this structure is given as

$$\psi_R(\theta_i) = K\tan^P\left(\frac{\theta_i}{2}\right) + \psi_R(0°); \quad 0 \le \theta_i < \pi/2, \quad -\pi \le \psi_R(0°) \le \pi \tag{4-1}$$

where ψ_R is the TE-to-z reflection coefficient phase, K is a gradient coefficient, P is a power factor, and θ_i is the plane wave incident angle. The constants K and P can be determined from the knowledge of ψ_R for three incident angles, as

$$P = \frac{log\left[\dfrac{\psi_R(\theta_{i_1}) - \psi_R(0°)}{\psi_R(\theta_{i_2}) - \psi_R(0°)}\right]}{log\left[\tan\left(\dfrac{\theta_{i_1}}{2}\right) / \tan\left(\dfrac{\theta_{i_2}}{2}\right)\right]}, \tag{4-2}$$

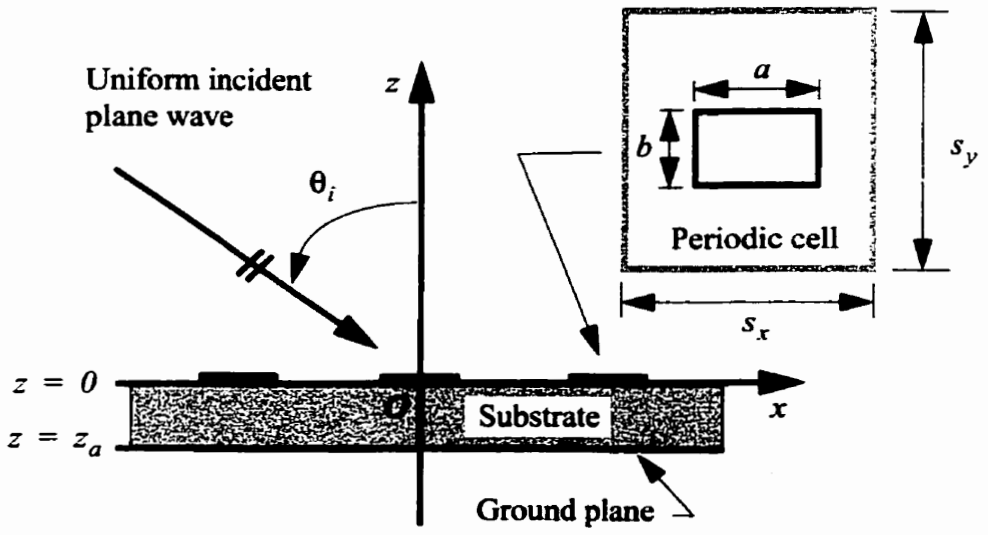

Fig. 4-1: An infinite periodic array of single-layer rectangular microstrip patches.

and

$$K = \frac{\psi_R(\theta_{i_1}) - \psi_R(0°)}{\tan^P\left(\frac{\theta_{i_1}}{2}\right)} = \frac{\psi_R(\theta_{i_2}) - \psi_R(0°)}{\tan^P\left(\frac{\theta_{i_2}}{2}\right)}, \tag{4-3}$$

where $0 < \theta_{i_1} < \theta_{i_2} < \pi/2$. The parameters $\psi_R(0°)$, $\psi_R(\theta_{i_1})$ and $\psi_R(\theta_{i_2})$ in (4-2) and (4-3) can be computed from the full wave analysis of the infinite periodic array.

4.1.2 Verification of Empirical Formulation with Full Wave Analysis

In principle, the two constants K and P of (4-1) can be determined using two incidence angles, in addition to $\psi_R(0°)$, as given in (4-2) and (4-3). However, (4-1) being an empirical equation, influences the accuracy of the results through θ_{i_1} and θ_{i_2}, which are the two incident angles selected for determining K and P. To investigate the dependence and sensitivity of the results on θ_{i_1} and θ_{i_2}, a study is conducted using different sets of values for these angles. The accuracy of the empirical formulation is also investigated for different patch sizes.

The empirical results are compared with those of the full wave infinite periodic array analysis obtained through formulations mentioned in Chapter 3. Care is taken to ensure good convergence and accuracy of the full wave solutions. Results for the resonant patch array are shown in Table 4-1. Three sets of incident angles are selected, which are ($\theta_{i_1} = 30°$,

$\theta_{i_2} = 60°$), ($\theta_{i_1} = 30°$, $\theta_{i_2} = 75°$) and ($\theta_{i_1} = 15°$, $\theta_{i_2} = 45°$). An examination of these results, and additional ones for the non-resonant patch arrays, indicates that, for all angles less than θ_{i_2}, the phase error due to the empirical formulation is always less than $2°$. The error increases rapidly for incidence angles beyond θ_{i_2}. In practice, the reflectarray focal length is generally assumed to be large, to reduce the phase quantization error. Thus, its edge angle is usually less than $60°$, and phase computation for large angles is unnecessary.

Fig. 4-2 through Fig. 4-4 compare graphically the empirical formulation data with the full wave solutions. Although the non-resonant patch arrays exhibit slightly larger phase errors, good agreement is evident for all angles less than θ_{i_2}, for both resonant and non-resonant patch arrays.

Table 4-1: TE-to-z reflection coefficient phase values for an infinite periodic array of single-layer, resonant, rectangular microstrip patches. $f = 11.761$GHz, $a = 0.731$cm, $b = 0.45$cm, $s_x = s_y = 1.25$cm, $\varepsilon_r = 2.2$, $z_a = 0.317$cm, $\phi_i = 90°$, x-polarization, and $|\Delta\psi_R| = |\psi_{R,\text{ full wave}} - \psi_{R,\text{ empirical}}|$.

Plane wave incident angle, θ_i	Phase of the TE-to-z reflection coefficient, ψ_R				
	Full wave analysis, $\psi_{R,\text{ full wave}}$	Empirical analysis, $\psi_{R,\text{ empirical}}$ ($\theta_{i_1} = 30°$, $\theta_{i_2} = 60°$)	Phase error, $\lvert\Delta\psi_R\rvert$ ($\theta_{i_1} = 30°$, $\theta_{i_2} = 60°$)	Phase error, $\lvert\Delta\psi_R\rvert$ ($\theta_{i_1} = 30°$, $\theta_{i_2} = 75°$)	Phase error, $\lvert\Delta\psi_R\rvert$ ($\theta_{i_1} = 15°$, $\theta_{i_2} = 45°$)
0°	*–0.08°*	—	—	—	—
10°	*2.93°*	*4.68°*	*1.75°*	*1.68°*	*0.28°*
20°	*11.59°*	*13.31°*	*1.72°*	*1.64°*	*0.55°*
30°	*24.72°*	—	—	—	*1.79°*
40°	*40.56°*	*38.87°*	*1.69°*	*1.52°*	*1.45°*
50°	*57.63°*	*56.04°*	*1.59°*	*1.16°*	*2.57°*
60°	*76.80°*	—	—	*0.82°*	*10.50°*
70°	*102.23°*	*102.09°*	*0.14°*	*1.22°*	*19.88°*
80°	*137.31°*	*133.31°*	*4.00°*	*1.89°*	*29.95°*

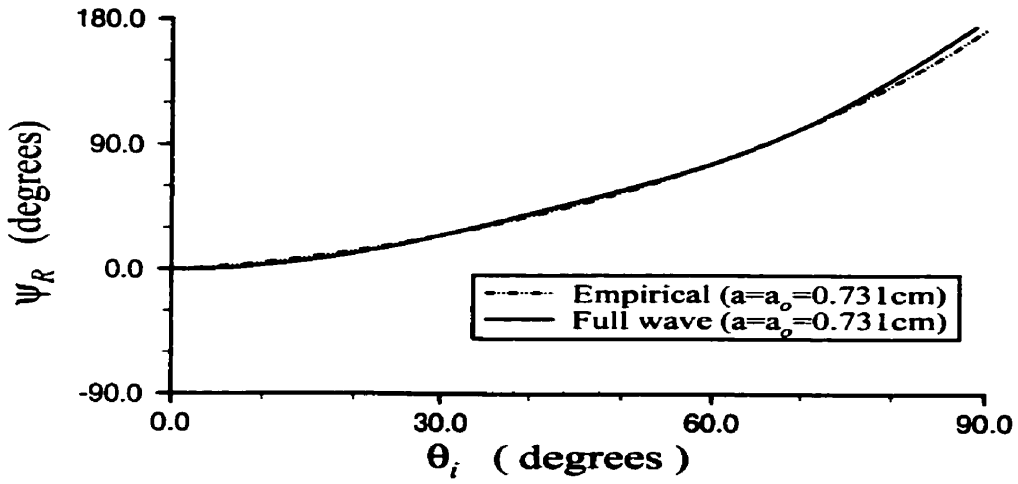

(a)

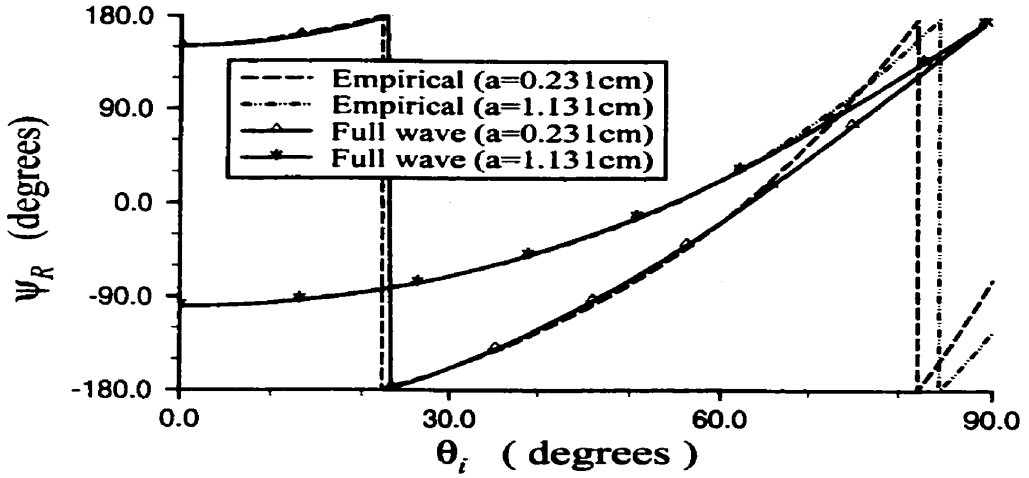

(b)

Fig. 4-2: Comparison of the TE-to-z reflection coefficient phase computed by empirical formulation and full wave analysis, with $\theta_{i_1} = 30°$ and $\theta_{i_2} = 60°$: (a) resonant patches, where a_o is the resonant length, and (b) non-resonant patches. Other parameters are the same as in Table 4-1.

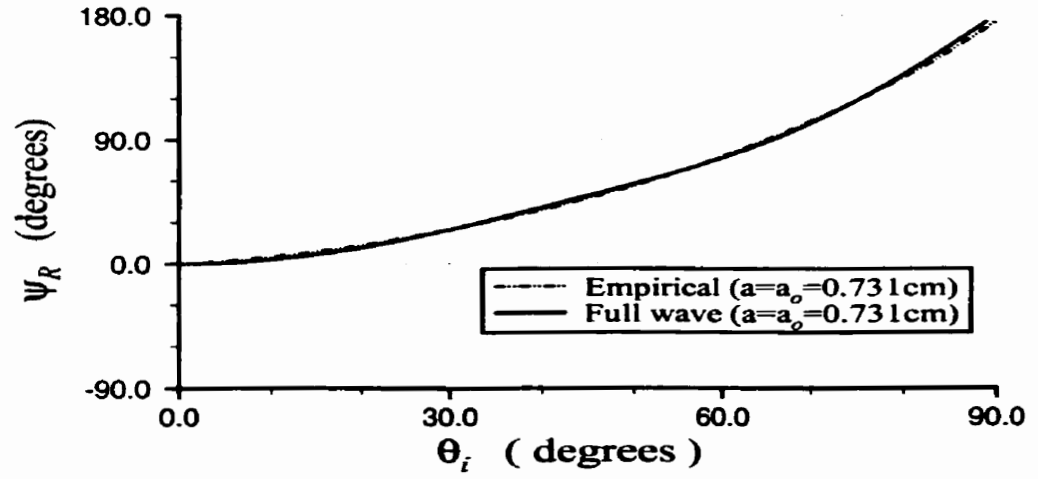

(a)

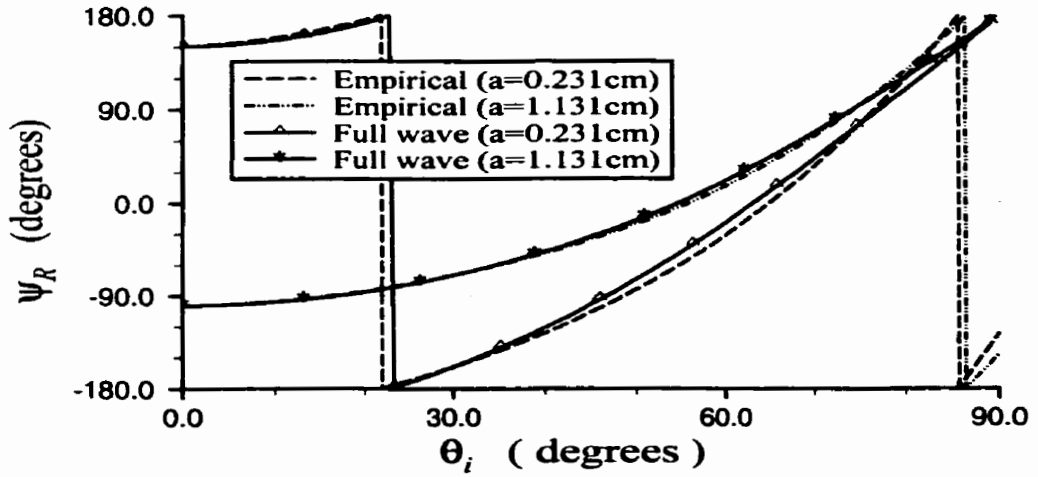

(b)

Fig. 4-3: Comparison of the TE-to-z reflection coefficient phase computed by empirical formulation and full wave analysis, with $\theta_{i_1} = 30°$ and $\theta_{i_2} = 75°$: (a) resonant patches, where a_o is the resonant length, and (b) non-resonant patches. Other parameters are the same as in Table 4-1.

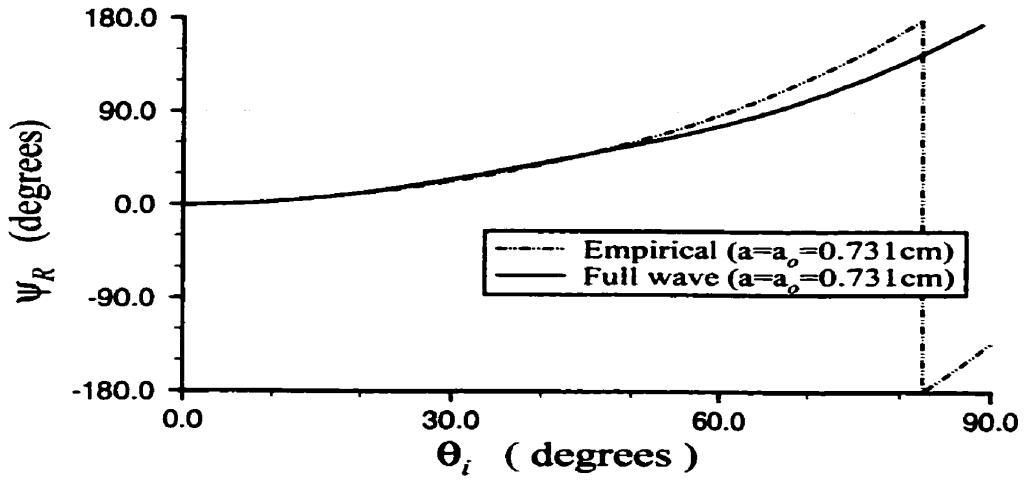

(a)

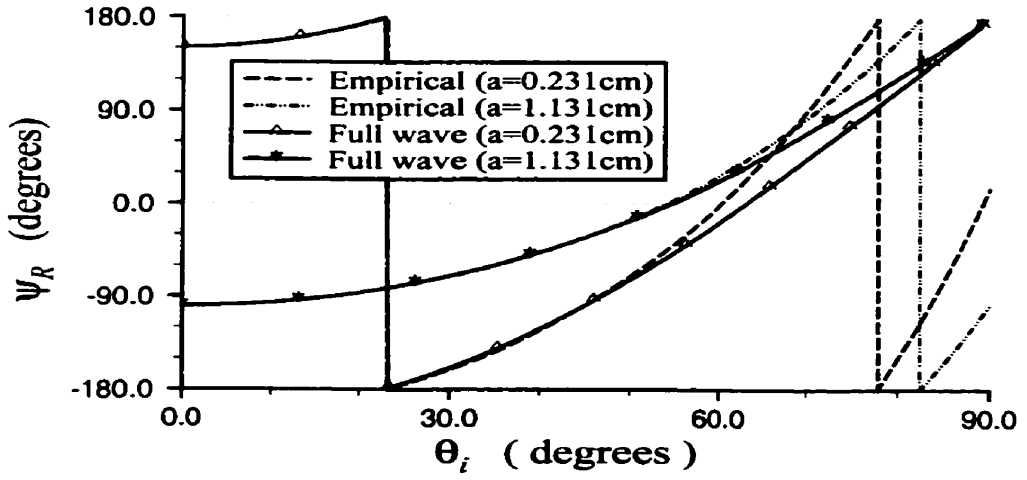

(b)

Fig. 4-4: Comparison of the TE-to-z reflection coefficient phase computed by empirical formulation and full wave analysis, with $\theta_{i_1} = 15°$ and $\theta_{i_2} = 45°$: (a) resonant patches, where a_o is the resonant length, and (b) non-resonant patches. Other parameters are the same as in Table 4-1.

4.2 PHASE QUANTIZATION ERRORS DUE TO FINITE PATCH SIZES

The phase quantization errors attributed to finite patch sizes, and also, to the continually varying phase of the incident field from the feed as the subtended feed angle increases, are investigated. Particular attention is given to sensitivity of phase to the feed-to-patch-element subtended angles and reflectarray F/D ratios for a given patch dimension and geometry.

4.2.1 Finite Patch Size and Phase Errors

For the purpose of this study, patches on the y-axis of the patch array are utilized as samples in the phase error analysis, where the element separation in the y-direction is s_y. The feed is assumed to be an infinite line-source located on the z-axis at $z = z_f$, and the patch array is symmetrically centered at the origin. These are depicted in Fig. 4-5. As such, the phase delay, ψ_i, corresponding to Fig. 4-5 is formulated as

$$\psi_i = k_o L_o (sec\theta_n - 1); \quad \text{for} \quad 0 \le \theta_n < \Theta_{s'} , \tag{4-4}$$

where k_o is the free-space propagation constant, θ_n is the subtended angle from the feed location $z = z_f$ on the z-axis to the n-th patch on the y-axis and is assumed as $\theta_n = \theta_i$ in the analysis, $\Theta_{s'}$ is the maximum feed subtended angle of the patch array, and L_o is the path length from the feed location to the patch element at the origin. In this case, L_o is also the focal length, F, of the reflectarray, that is, $F = L_o = z_f$. The phase of the scat-

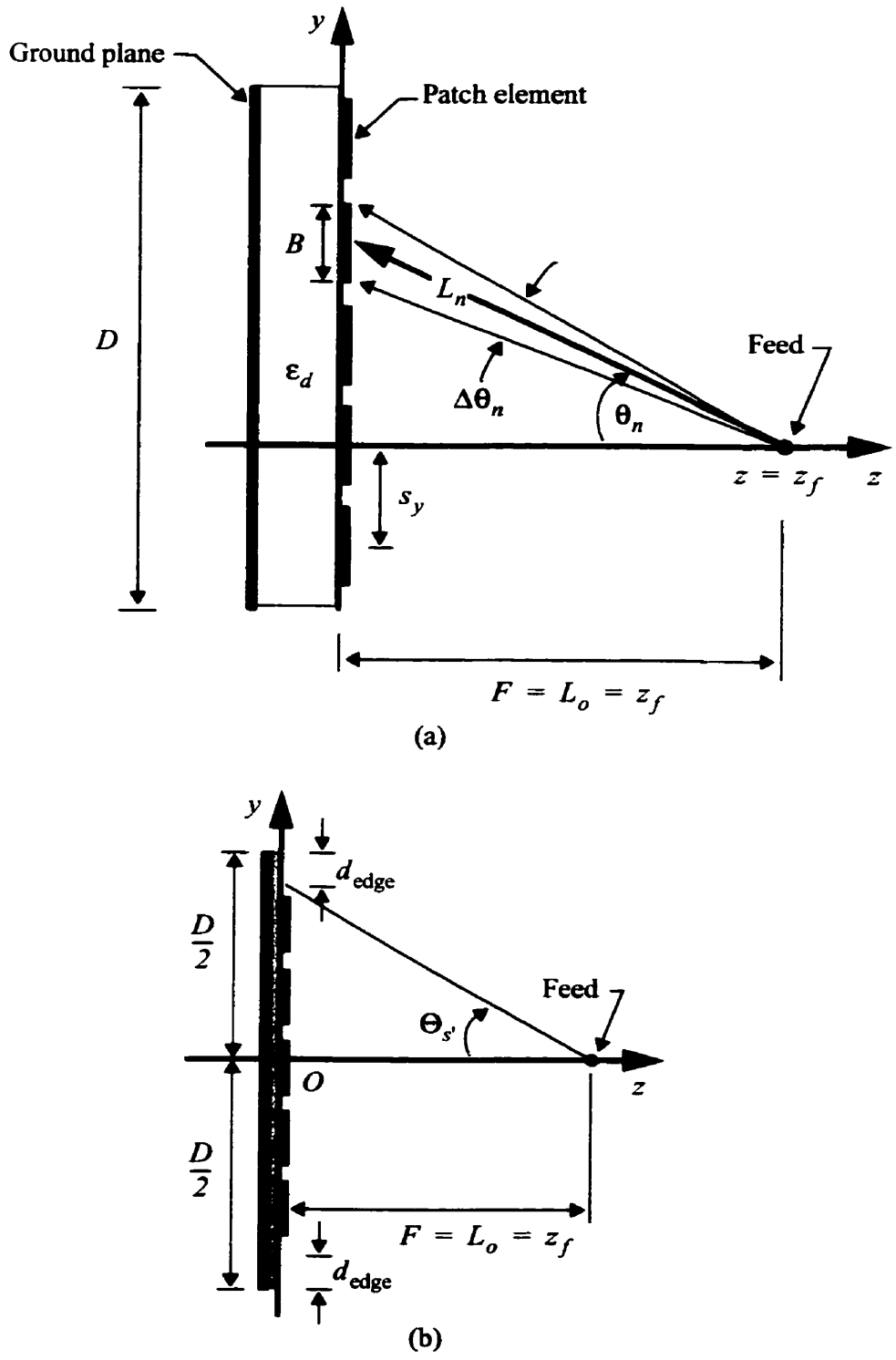

Fig. 4-5: Cross section schematics of a microstrip reflectarray: (a) illustrations of various geometric parameters, and (b) for defining the maximum subtended feed angle, $\Theta_{s'}$.

tered wave ψ_R, is computed from the infinite periodic array modelling discussed in Chapter 3.

Using (4-4), the rate of change of the phase delay ψ_i with respect to the incident angle at $\theta_i = \Theta_{s'}$ for a given F/D ratio and d_{edge}, is $(d\psi_i / d\theta_i)\big|_{\theta_i = \Theta_{s'}}$, as given by

$$\frac{2}{k_o \tilde{D}_N}\left(\frac{d\psi_i}{d\theta_i}\right)\bigg|_{\theta_i = \Theta_{s'}} = \frac{\sqrt{[1 - N^{-1}]^2 + [2(F/\tilde{D}_N)]^2}}{2(F/\tilde{D}_N)}, \tag{4-5a}$$

where

$$\tilde{D}_N = D - 2d_{\text{edge}}, \tag{4-6b}$$

$$0 \le \frac{d\psi_i}{d\theta_i}\bigg|_{\theta_i < \Theta_{s'}} < \frac{d\psi_i}{d\theta_i}\bigg|_{\theta_i = \Theta_{s'}} \tag{4-6c}$$

for $0 \le \theta_i \le \Theta_{s'}$, D is the ground plane dimension, in the y-direction, of the patch array, d_{edge} is the extension length, in the y-direction, of the ground plane edge from the patch array edge, and N is the total number of patch elements along the y-axis of the patch array.

It follows from (4-5), and the assumption of $d_{\text{edge}} = 0$, that the rate of change of the phase delay at $\theta_i = \Theta_{s'}$ with respect to the F/D ratio is $[d\psi_i / d(F/D)]\big|_{\theta_i = \Theta_{s'}}$, as described by

$$\frac{1}{k_o D}\left[\frac{d\psi_i}{d(F/D)}\bigg|_{\theta_i=\Theta_{s'}}\right] = \left[\frac{2}{k_o D}\left(\frac{d\psi_i}{d\theta_i}\right)\bigg|_{\theta_i=\Theta_{s'}}\right]^{-1} - 1, \qquad (4\text{-}7)$$

Equations (4-5) and (4-7) represent the sensitivities of the phase delay to change in θ_i and F/D ratio at $\theta_i = \Theta_{s'}$, respectively.

The geometrical parameter B shown in Fig. 4-5(a) represents the finite patch dimension that spans an angle $\Delta\theta_n$. Some patch geometries for a microstrip reflectarray, which were studied in [81], are illustrated in Fig. 4-6 with the dimensional parameter B defined for each geometry.

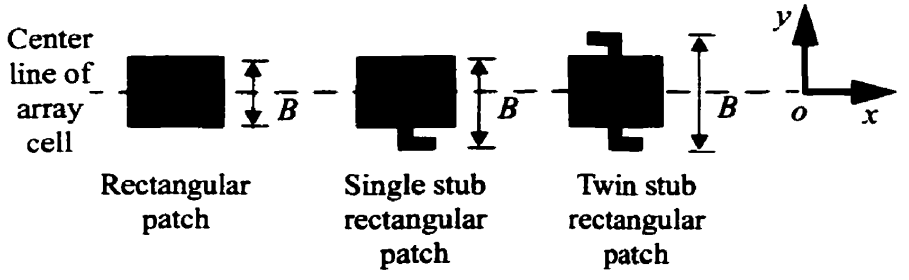

Fig. 4-6: Definitions of dimension parameter B for patches for a microstrip reflectarray.

4.2.2 Examples for Discussion

The phase delay curve for $F = z_f = 15\text{cm}$, evaluated at frequency $f = 11.761\text{GHz}$ using (4-4), is depicted in Fig. 4-7. This curve indicates that the phase delay ψ_i is highly sensitive to changes in the incident angle θ_i, when θ_i is large. Hence, for a given patch at a subtended angle θ_n, a difference in phase delay exists across the patch due to its finite size B shown in Fig. 4-6. This difference in phase delay is denoted as $\Delta\psi_i$. A large $\Delta\psi_i$ produces a large phase error that results in degradation of the reflectarray performance.

Fig. 4-8(a) illustrates $\Delta\psi_i$ for different patch sizes over a range of subtended angle θ_n. Given F/D ratios *0.293* and *0.488* for reflectarray configurations similar to Fig. 4-5(b),

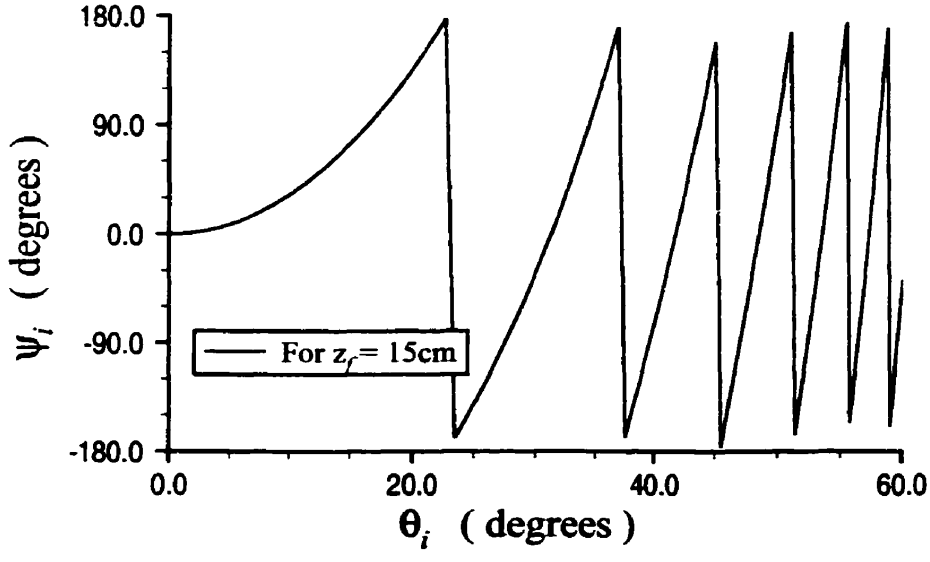

Fig. 4-7: The phase delay curve for $F = z_f = 15\text{cm}$, evaluated at frequency $f = 11.761\text{GHz}$.

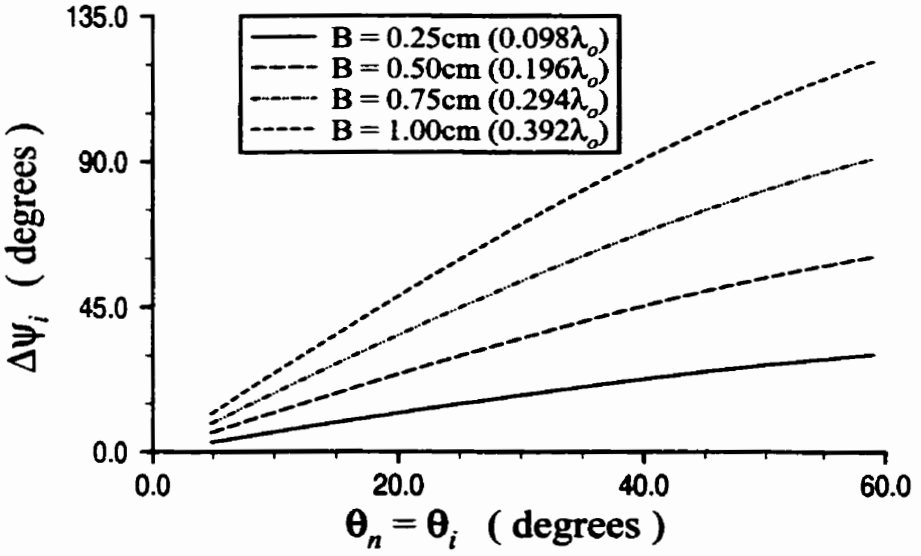

(a)

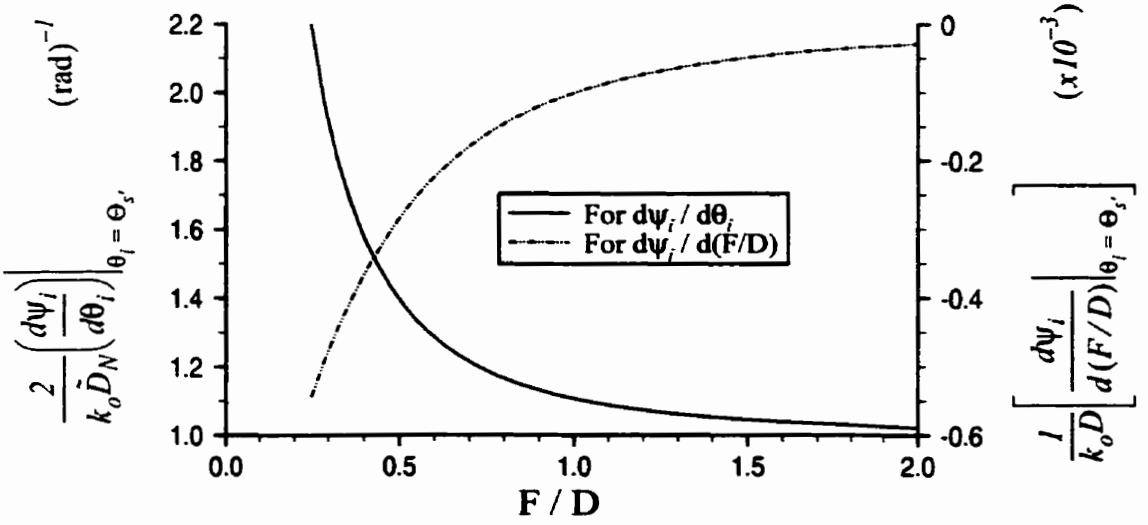

(b)

Fig. 4-8: Phase quantization errors: (a) difference in phase delays across a patch width, $\Delta\psi_i$, due to the finite sizes of patches for a microstrip reflectarray, evaluated at the frequency $f = 11.761$GHz with its wavelength being $\lambda_o = 2.5508$cm, and (b) phase delay sensitivity at $\theta_i = \Theta_{s'}$, evaluated from (4-5) and (4-7) for $N = 41$.

and assumming that $d_{edge} = 0$, the corresponding $\Theta_{s'}$ are $59.66°$ and $45.71°$, respectively. For $B = 0.75$cm, these correspond to maximum $\Delta\psi_i$ as $91.43°$ and $75.82°$, respectively.

The phase delay sensitivity plots are shown in Fig. 4-8(b), which are obtained through (4-5) and (4-7), for $N = 41$. For small F/D ratios, the phase delay at $\Theta_{s'}$ is highly sensitive to θ_i, and becomes relatively insensitive as F/D ratios increase, as indicated by the first curve in the figure. Similar observations are also made of the phase delay sensitivity to changes in F/D ratios at $\Theta_{s'}$, as shown by the second curve.

Therefore, for small F/D ratios, the $\Delta\psi_i$ at the $\Theta_{s'}$ angles would be very large and small patch dimensions B should be employed as much as possible in such cases.

4.3 RECTANGULAR AND NARROW STRIP PATCHES

A rectangular microstrip patch with an aspect ratio $b/a > 0.25$ possesses a wider bandwidth than that of a narrower patch, such as a narrow strip patch with $b/a < 0.25$, but at the cost of a larger unattainable reflection phase range [7]. Consequently, due to its less sensitive phase curve at near-resonant patch lengths a, as discussed in Chapter 3, the rectangular patch array can provide a better phase correction within its attainable reflection phase range, compared to that of the strip patch array.

Nevertheless, since its width dimension B is larger, the phase quantization error at a large subtended angle θ_n for the rectangular patch is greater, compared to that of the strip patch. Hence, this may result in a poorer reflectarray phase collimation for the rectangular patch array.

In Chapter 5, due to their very small unattainable reflection phase ranges, strip patches would be utilized in the combination patch array for an offset-fed reflectarray configuration.

4.4 SUBSTRATE THICKNESS AND HIGHER-ORDER MODES

For a low permittivity thick substrate microstrip reflectarray, the maximum subtended angle of the patch array $\Theta_{s'}$, depicted in Fig. 4-5(b), may be restricted by the onset of propagating higher-order modes. Hence, this issue is investigated for the rectangular patch array in this section.

Similar to Chapter 3, a TE-to-z incident plane wave at $\phi_i = 90°$, with $\hat{E}$ x-directed, is utilized as a modelling approximation, where $\theta_n = \theta_i$ is assumed. Rectangular patch dimensions are $a = b = 0.75$cm, element separations in the x- and y- directions are $s_x = s_y = 1.25$cm, respectively, and $\varepsilon_r = 1.03$ for a foam substrate.

From Fig. 4-9, for $\varepsilon_r = 2.5$, the resonant frequency f_o decreases as the substrate thickness z_a increases. Consequently, the frequency bandwidth around f_o increases, agreeing with [7]. Similar behavior can also be observed for $\varepsilon_r = 1.03$.

In general, the critical incident angle θ_{ic} at the onset of propagating higher-order modes is dependent on frequency, but independent of substrate thickness z_a, as represented by the discontinuities illustrated in Fig. 4-10 for $\varepsilon_r = 1.03$. In fact, the patch arrays for these satisfy the well-known phased array grating lobe criterion $|sin\theta_{ic}| \leq \lambda/s_y - 1$, where, in this case, θ_{ic} is the maximum scan angle and s_y is the element separation [100].

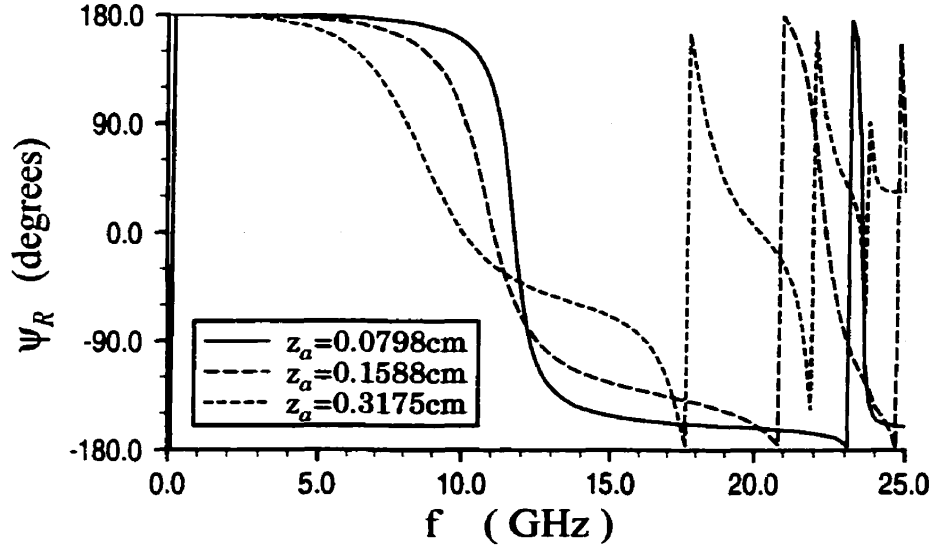

Fig. 4-9: TE-to-z reflection coefficient phases at normal incidence ($\theta_i = 0^o$) and $\phi_i = 90°$, due to frequency f, for different substrate thicknesses z_a. $\varepsilon_r = 2.5$, $a = b = 0.75$cm, $s_x = s_y = 1.25$cm and $\hat{E}$ is x-directed. Resonant frequencies $f_o = 11.761$GHz, 11.109GHz and 10.110GHz, for $z_a = 0.0798$cm, 0.1588cm and 0.3175cm, respectively.

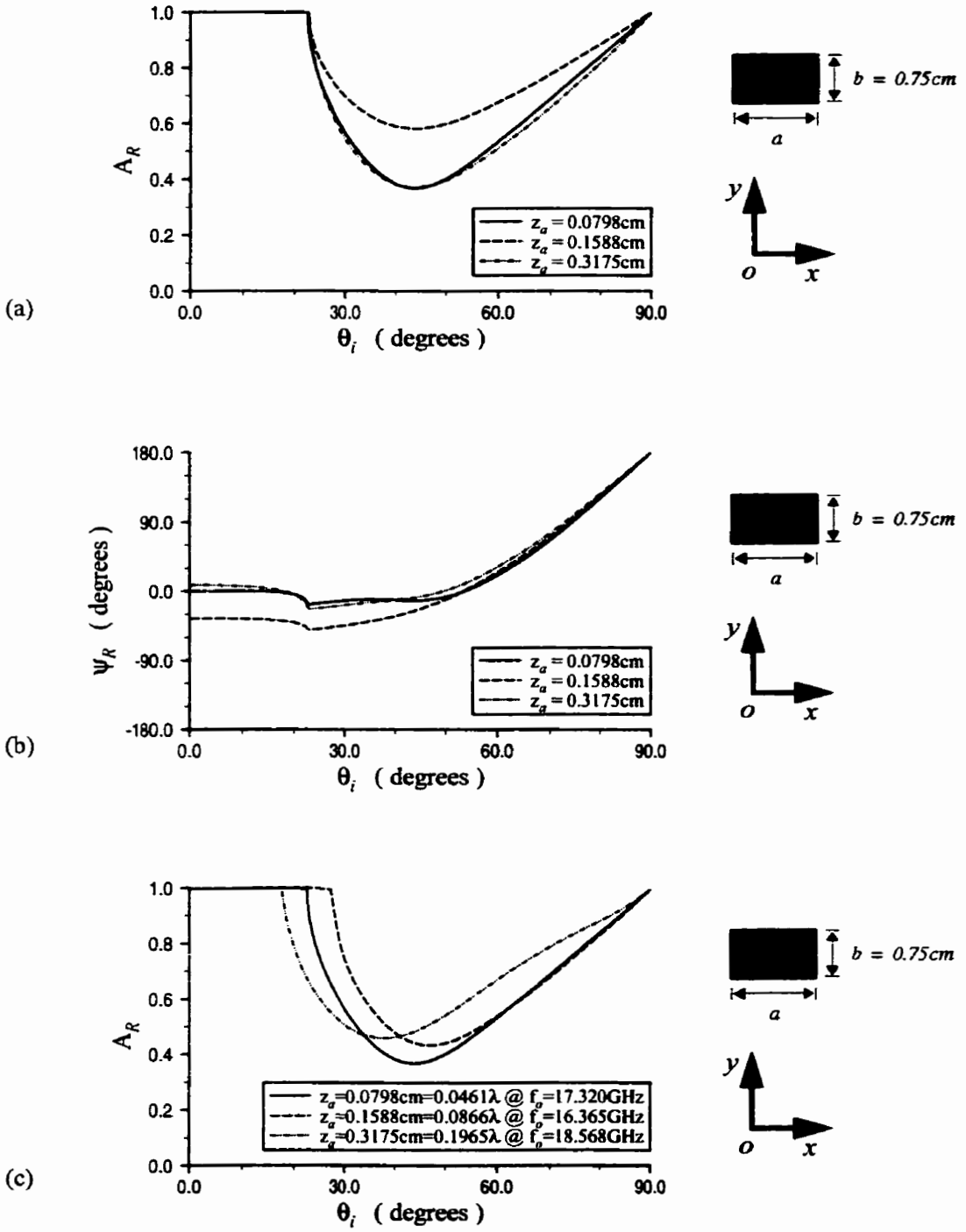

Fig. 4-10: TE-to-z reflection coefficients due to incident angle θ_i, for different substrate thicknesses z_a: (a) magnitudes A_R at $f = 17.320$GHz, (b) phases ψ_R at $f = 17.320$GHz, and (c) magnitudes A_R at different f_o. $\varepsilon_r = 1.03$, $a = b = 0.75$cm, $s_x = s_y = 1.25$cm, $\phi_i = 90°$ and $\hat{E}$ is x-directed.

At $f = 17.320$GHz, $\theta_{ic} \approx 22.69^{o}$ for all the substrate thicknesses shown in Fig. 4-10(a) and (b). For $\theta_i > \theta_{ic}$, both first-order (*00*-th, or specular) and *01*-th Floquet modes propagate, thus resulting in a large magnitude attenuation illustrated in Fig. 4-10(a) for the first-order mode. Hence, if the first-order reflection coefficient was to be utilized for reflectarray applications, Θ_s, must be less than θ_{ic}, so that power loss due to propagating higher-order modes is negligible.

Fig. 4-10(a) and (b) shows a resonance at $f = 17.320$GHz, for the substrate thickness $z_a = 0.0798$cm (i.e. $z_a = 0.0461\lambda$). Furthermore, Fig. 4-10(c) demonstrates that θ_{ic} decreases with increasing resonant frequency f_o. In general, however, Fig. 4-11 indicates that θ_{ic} decreases with increasing frequency f, as governed by the grating lobe criterion.

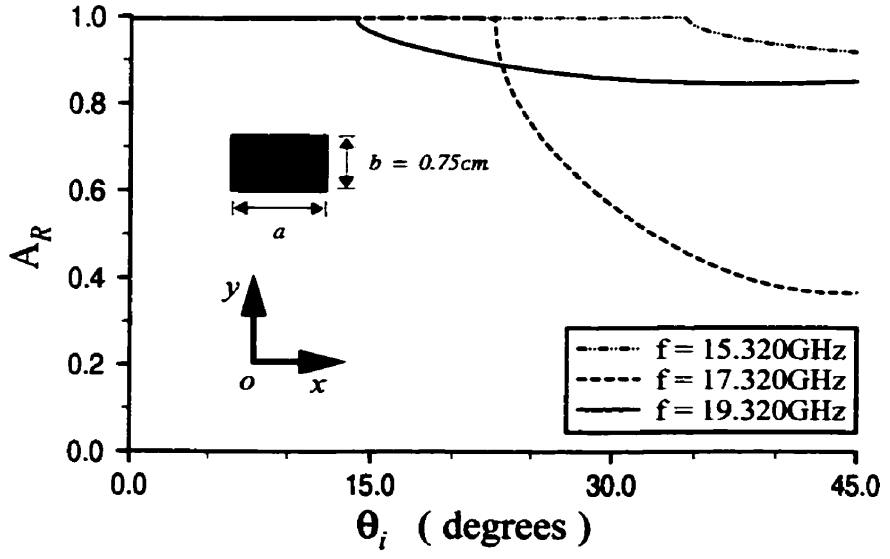

Fig. 4-11: TE-to-z reflection coefficient magnitudes A_R at different frequencies f, due to incident angle θ_i, for $z_a = 0.0798$cm. $\varepsilon_r = 1.03$, $a = b = 0.75$cm, $s_x = s_y = 1.25$cm, $\phi_i = 90°$ and $\vec{E}$ is x-directed.

Therefore, substrate permittivity and thickness, patch array dimensions, and operation frequency, must be chosen such that θ_{ic} is adequately large, so that no propagating higher-order modes is produced for a given θ_s. That is, the reflectarray F/D ratio is generally made sufficiently large.

4.5 VARIABLE-STUB-LENGTH MICROSTRIP PATCH ARRAYS

Fig. 4-12, illustrates three types of microstrip patches for this study, namely,

(i) rectangular patch,

(ii) single-stub patch, and

(iii) twin-stub patch.

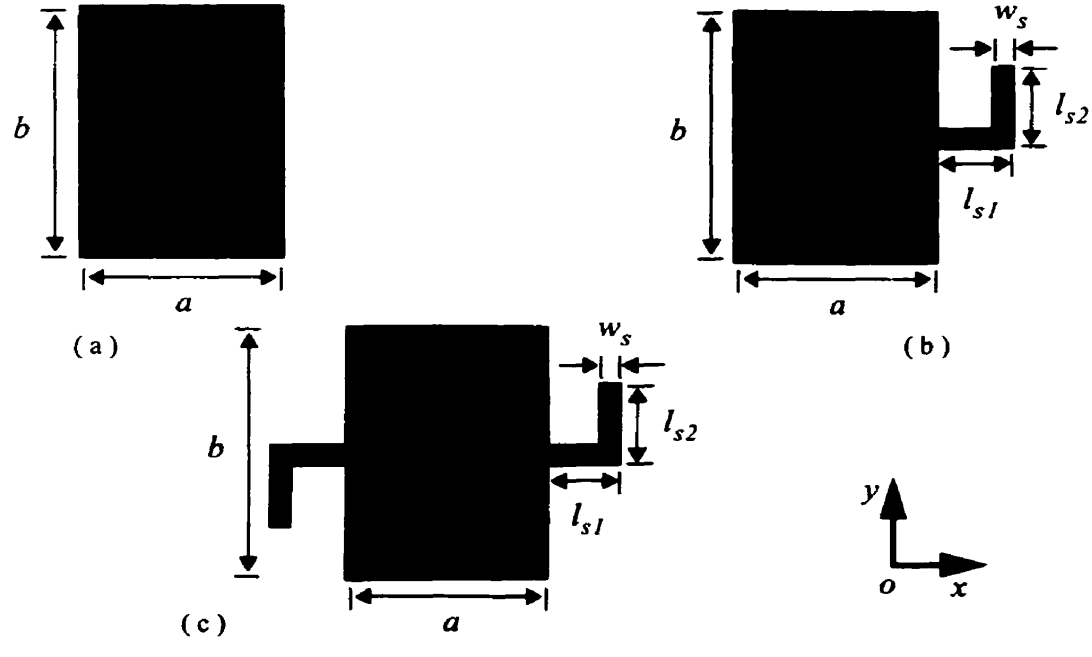

Fig. 4-12: Microstrip patches for a reflectarray: (a) rectangular patch, (b) single-stub patch, and (c) twin-stub patch.

A reflectarray with a variable-patch-length patch array employs the patch length for reflection phase control [7][80], as discussed in Chapter 3. On the other hand, a reflectarray with a variable-stub-length patch array utilizes stub length for reflection phase control [9][101]. That is, the stub attachments are phase delay transmission lines employed to correct the reflection phase of the reflectarray so that a co-phasal aperture plane is achieved, satisfying (3-19).

For single- and twin- stub microstrip patch arrays, the element spacings for the x- and y-directions are $s_x = s_y = 1.25\text{cm}$, respectively. A TE-to-z incident plane wave is assumed, with $\hat{E}$ x-polarized. The reflection reference plane for the infinite periodic array simulations is at $z = z_p = 0.5\lambda_o$, where λ_o is the free space wavelength for a center frequency $f = 11.761\text{GHz}$.

The objective of this study is to demonstrate that the TE-to-z reflection coefficient phases of the single- and twin- stub patches are linearly dependent on stub length, and thus, their bandwidth are not restricted by their reflection phase characteristics. For the purpose of this study, however, the vertical stub length l_{s2} is assumed to be zero. Thus, the length deviations from the resonant patch length a_o are defined as

(i) $\delta = a - a_o$ for a rectangular patch, as described in Chapter 3,

(ii) $\delta = l_{s1}$ for a single-stub patch, and

(iii) $\delta = 2l_{s1}$ for a twin-stub patch,

where l_{s1} is defined in Fig. 4-12.

4.5.1 Single-Stub Microstrip Patch Array

The resonant rectangular patch for $f = 11.761$GHz, as presented in Chapter 3, is utilized for this stubbed patch geometry, where $\varepsilon_r = 2.5$, $z_a = 0.0798$cm and $a_o = a = b = 0.75$cm. For the single-stub patch illustrated in Fig. 4-12(b), a stub width $w_s = 0.01$cm is attached onto the patch.

For the rectangular patch array discussed in Chapter 3, the TE-to-z reflection coefficient phase ψ_R varies nonlinearly with patch length, and is highly sensitive to patch length near resonance. However, the single-stub patch array is generally more wideband. In Fig. 4-13, where straight stubs (without the $90°$ bends) are utilized, i.e. with $l_{s2} = 0$, the phase curves are relatively linear, agreeing well with [101].

4.5.2 Twin-Stub Microstrip Patch Array

Fig. 4-13 shows the wideband characteristics of the twin-stub patch array, similar to that of the single-stub patch array. Moerover, with an additional 0.2cm of total stub length, the twin-stub patch has an extended TE-to-z reflection coefficient phase range of approximately $45°$ more at $f = 11.761$GHz.

4.5.3 Comparisons of Single- and Twin- Stub Microstrip Patch Arrays

At short stub lengths, Fig. 4-13 indicates minor differences in ψ_R between the phase curves. These are attributed to the relatively high sensitivity of ψ_R to stub length near resonance, because of a discontinuous structure. Such a problem may be mitigated using the Boundary Integral - Resonant Mode Expansion (BI-RME) method described in [70][71].

From Fig. 4-14, ψ_R for both single- and twin- stub patches increase with increasing incident angle θ_i. This behavior is similar to those observed and discusseed in Chapter 3 for rectangular patch arrays.

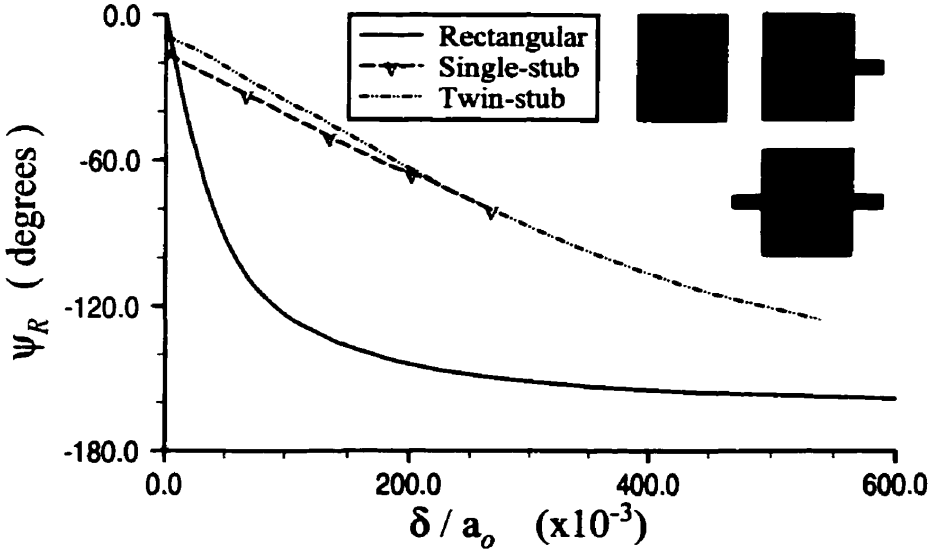

Fig. 4-13: Comparisons of TE-to-z reflection phase curves at normal incidence for rectangular, single-stub and twin-stub patch arrays, with $f = 11.761$GHz, $\varepsilon_r = 2.5$, $z_a = 0.0798$cm, $s_x = s_y = 1.25$cm, $a_o = a = b = 0.75$cm and $l_{s2} = 0$.

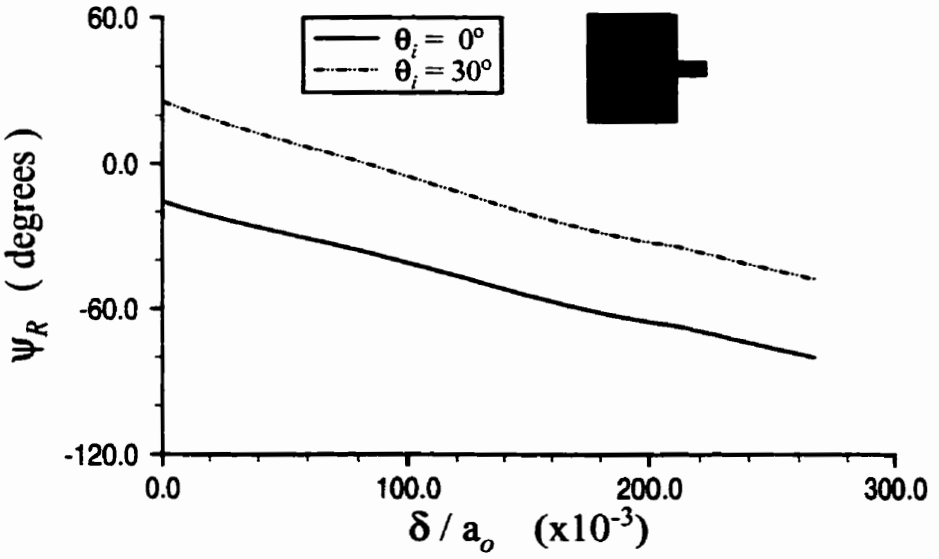

(a)

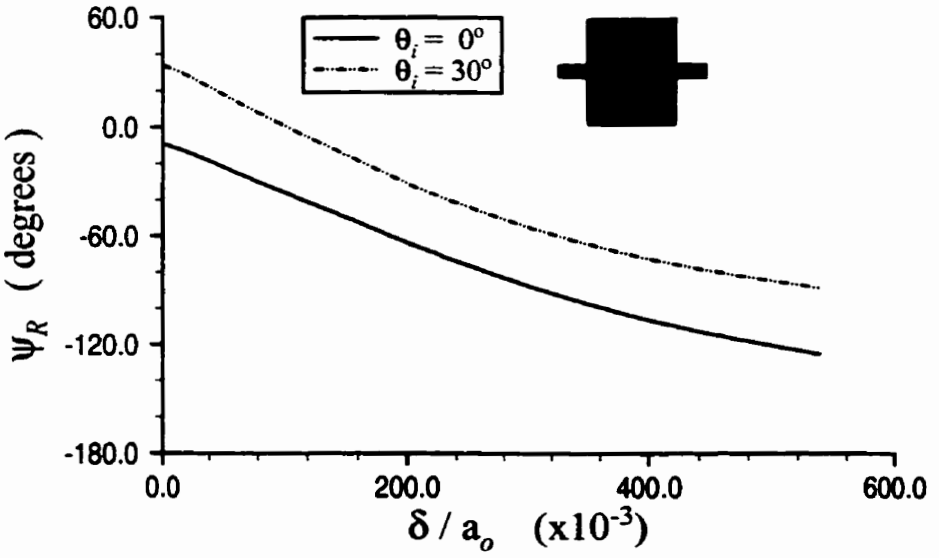

(b)

Fig. 4-14: TE-to-z reflection phase curves for different incident angles θ_i: (a) single-stub patch array, and (b) twin-stub patch array, with the same parameters as in Fig. 4-13.

4.6 TAPERED LINE-SOURCE DISTRIBUTIONS

For the line-source described in Chapter 3, near-field uniformity along the x-direction was assumed. However, due to Gibb's phenomenon in a finite line-source, the actual computed near-field is oscillatory [94]. Although this oscillatory amplitude is generally not substantial, its effect on the resulting phase correction error is sometimes significant.

For the reflectarray considered in this investigation, the rectangular microstrip patch arrays of Chapter 3 are utilized. Reflectarray radiation characteristics, illuminated by line-sources with different tapered distributions, are then compared to that of the uniform distribution.

4.6.1 Near-Field Feed Analysis

The tapered source distributions employed are cosine-pedestal, Chebyshev and Taylor distributions, of which the normalized source excitations at $f = 11.761$GHz are presented in Fig. 4-15. The cosine-pedestal distribution is determined from $P + (1 - P)\cos(\pi x/L)$ [102], where P is the pedestal level in negative dB, and L is the length of the line-source.

Compared to the uniform distribution, these tapered distributions generate lower field intensities near array edges, as depicted in Fig. 4-16. Hence, both the uniform and Chebyshev distributions provide the largest oscillation amplitudes, and the cosine-pedestal and

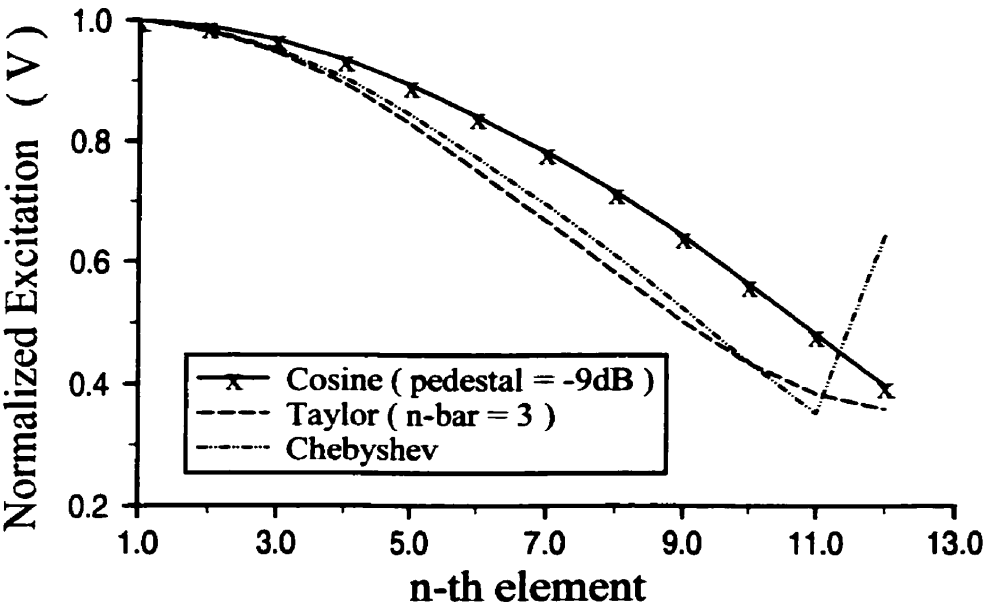

Fig. 4-15: Source excitations for tapered distributions at $f = 11.761$GHz, due to the line-source described in Chapter 3. SLL=-25dB for both Taylor and Chebyshev distributions.

Taylor distributions produce the smallest, as depicted in the figure. Similar characteristics are observed for the near-field phases as well.

Furthermore, when compared to the cosine-pedestal distributions of different pedestal tapering levels, the uniform distribution produces the largest oscillation amplitudes, as illustrated in Fig. 4-17. On the other hand, the cosine-pedestal distribution, with pedestal = -9dB, and the Taylor distribution, yield the least oscillation amplitudes.

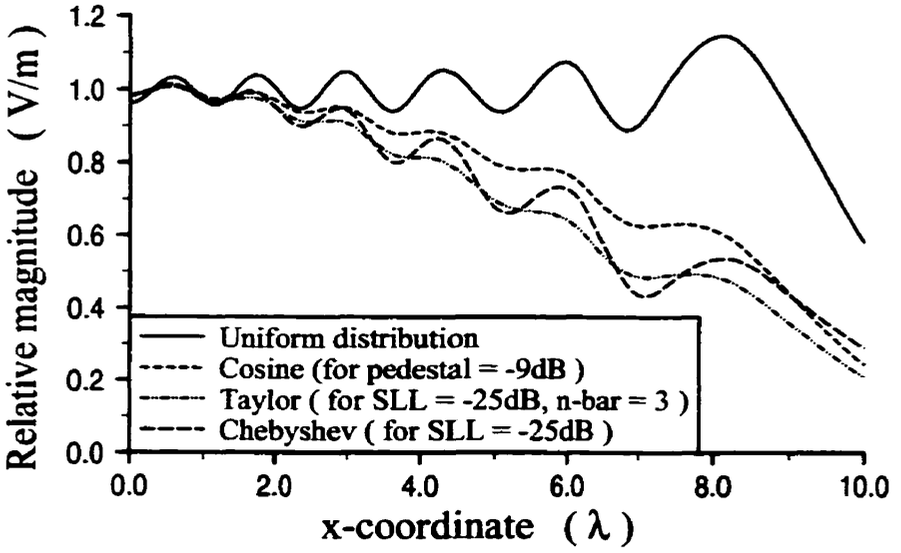

(a)

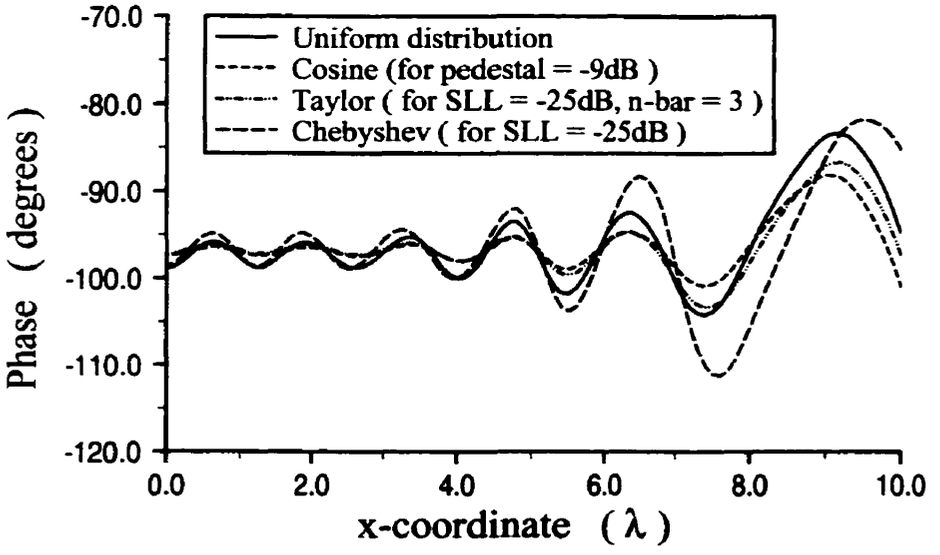

(b)

Fig. 4-16: x-polarized $\hat{E}$ fields in the near-field (Fresnel) zone along the x-axis on the patch array, due to different line-source distributions, for $f = 11.761$GHz: (a) relative magnitudes, and (b) phases. The last patch column on the array is at $x = 9.801\lambda$, where λ is the wavelength, and $z_f = 15$cm.

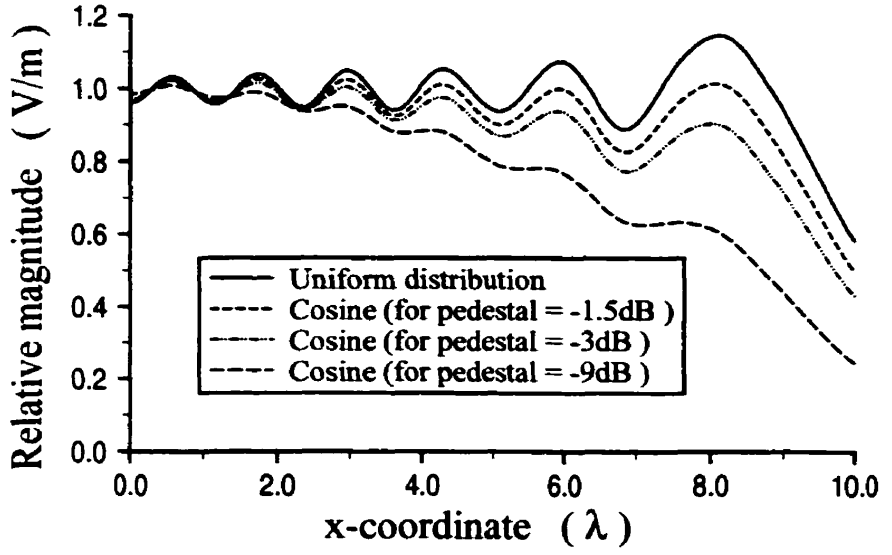

(a)

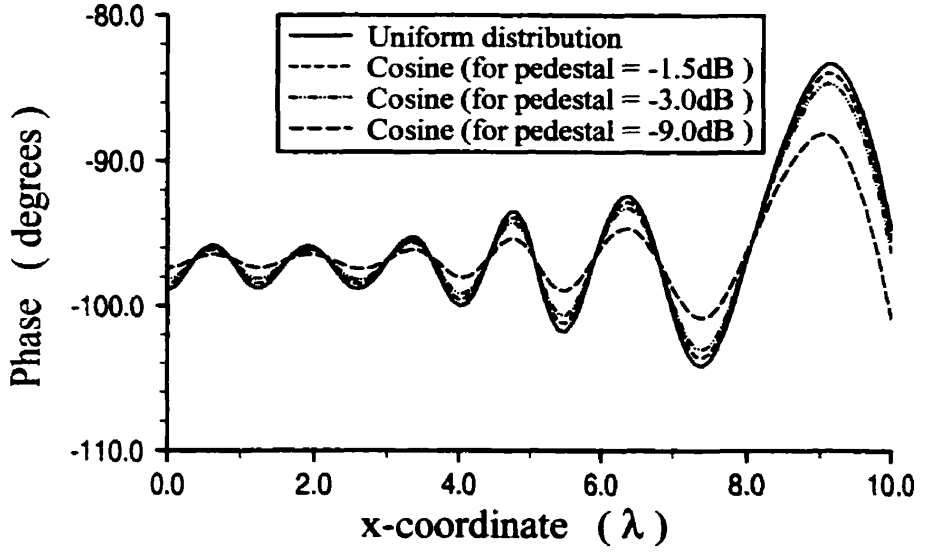

(b)

Fig. 4-17: x-polarized $\hat{E}$ fields in the near-field (Fresnel) zone along the x-axis on the patch array, due to uniform and cosine-pedestal line-source distributions, for $f = 11.761$GHz: (a) relative magnitudes, and (b) phases. The last patch column on the array is at $x = 9.801\lambda$, where λ is the wavelength, and $z_f = 15$cm.

4.6.2 Reflectarray Far-Field Characteristics

In general, large near-field oscillations of the uniform and tapered line-source distributions contribute to the increase in phase correction errors. Consequently, the loss in reflectarray directivity D_o is increased, as indicated in Table 4-2.

Significant effects are further observed from the table for spillover efficiencies and sidelobe levels (SLL) in the E-plane ($\phi = 0^o$). Very low first SLL in the E-plane ($\phi = 0^o$) and good spillover efficiencies are typical for large distribution taperings. However, they yield larger HPBWs in the E-plane ($\phi = 0^o$) and lower directivities D_o.

Fig. 4-18 illustrates the reflectarray directive gain patterns D_g in the E- and H- planes ($\phi = 0^o$ and $\phi = 90^o$, respectively) for the reflectarray fed using these line-source distributions. Since the line-source is oriented parallel to the x-axis, its source distribution has negligible effect on the reflectarray directive gain pattern in the H-plane ($\phi = 90^o$), which is mainly governed by column elements of the patch array.

Table 4-2: Radiation properties of a microstrip reflectarray fed using different line-source distributions at $f = 11.761$GHz, with the line-source at feed distance $z_f = 15$cm. The line-source near-field oscillation amplitude is included in the computations, and there is no phase error in the ideal patch array. Patch array parameters are the same as in Fig. 3-8.

Radiation properties	Line-source distributions					
	Uniform distribution	Taylor (SLL=−25dB, $\bar{n} = 3$)	Chebyshev (SLL=−25dB)	Cosine-pedestal distributions		
				Pedestal=−1.5dB	Pedestal=−3dB	Pedestal=−9dB
D_o (dBi) (ideal patch array)	35.28	34.96	34.97	35.29	35.28	35.13
D_o (dBi) (actual patch array)	35.02	34.72	34.71	35.04	35.04	34.90
HPBW ($\phi = 0^o$)	2.58^o	3.07^o	2.99^o	2.73^o	2.70^o	2.93^o
First SLL (dB) ($\phi = 0^o$)	−13.32	−24.05	−23.10	−14.79	−15.29	−19.04
Loss in directivity (dB)	0.26	0.23	0.26	0.25	0.24	0.23
Spillover (percent)	10.41	7.52	9.20	9.69	9.12	7.58

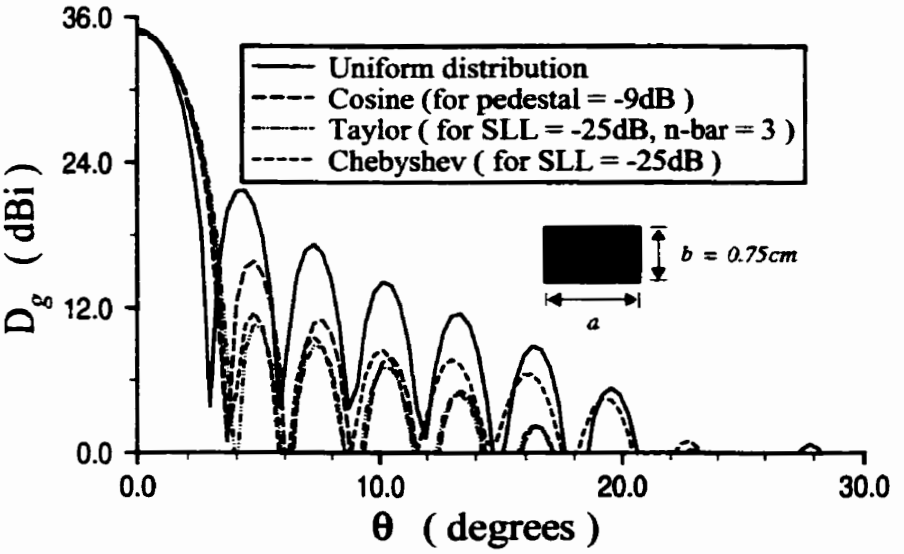

(a)

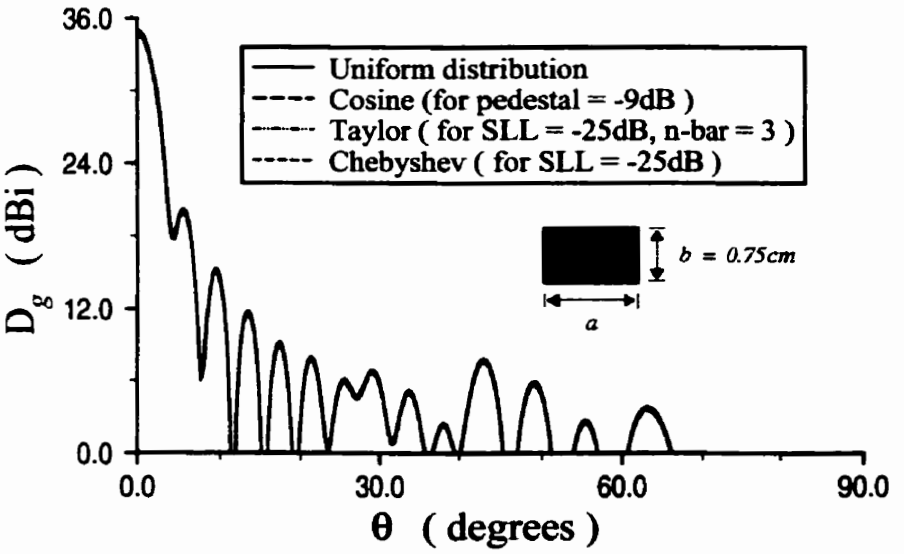

(b)

Fig. 4-18: Reflectarray directive gain patterns, D_g, at $f = 11.761$GHz: (a) E-plane ($\phi = 0^o$), and (b) H-plane ($\phi = 90^o$). Other parameters are the same as in Table 4-2.

4.7 CONCLUSION

For the analysis of infinite periodic arrays of single-layer rectangular microstrip patches, an empirical expression is obtained and verified for calculating the phase of the TE-to-z reflection coefficient. It requires only three parameter determinations using the full wave analysis, which reduces computational times significantly. It is also relatively accurate.

Phase quantization errors, attributed to finite patch sizes, is generally significant at large subtended feed angles θ_n. That is, it increases with the patch size. Nevertheless, it can be reduced by increasing the F/D ratio.

A microstrip reflectarray designed using low permittivity and thick substrate can experience limitations due to propagating higher-order modes, especially for a small F/D ratio. However, a thick substrate increases the frequency bandwidth.

Stubbed microstrip patch geometries are also investigated. Their TE-to-z reflection coefficient phases are observed to be linearly dependent on stub lengths. Also, a twin-stub patch offers an extended reflection phase range, as compared to a single-stub patch.

The effect of tapered line-source distributions on the reflectarray performance is investigated. They generally improve the reflectarray far-field characteristics, such as, spillover losses and SLL in the E-plane ($\phi = 0^o$), but at the cost of lower directivities.

5 Offset-Fed Configuration

To further verify the results in Chapter 3, offset-fed microstrip reflectarrays for rectangular and combination of rectangular, strip and hat-shaped patch geometries are investigated. This chapter provides their rigorous analysis. Properties of a multiple-geometry patch array are analyzed and compared to those of a rectangular patch array. Some reflectarray properties, such as, phase errors, radiation patterns, directivities and spillover efficiencies, are also discussed.

The offset-fed configuration decreases the feed blockage inherent in the center-fed configuration. The offset-fed configuration, however, is more complex since it involves additional geometrical parameters. Included in the analysis, for the purpose of this study, are near-field oscillations due to the finite line-source feed, similar to those discussed in Chapter 4.

5.1 An Offset-Fed Configuration

An offset-fed reflectarray is realized through the determination of its feed location in the yz-plane. Details of its parameters are presented in this section. It is assumed that the line-source feed utilized is the same as those employed in the center-fed configurations, mentioned in Chapter 3 and Chapter 4.

5.1.1 Geometrical Description

Referring to Fig. 5-1, the upper and lower edge subtended angles are Θ_s and θ_c, respectively, where $0° < \theta_c \leq \Theta_s < 90°$. The beamwidth of feed illumination onto the patch

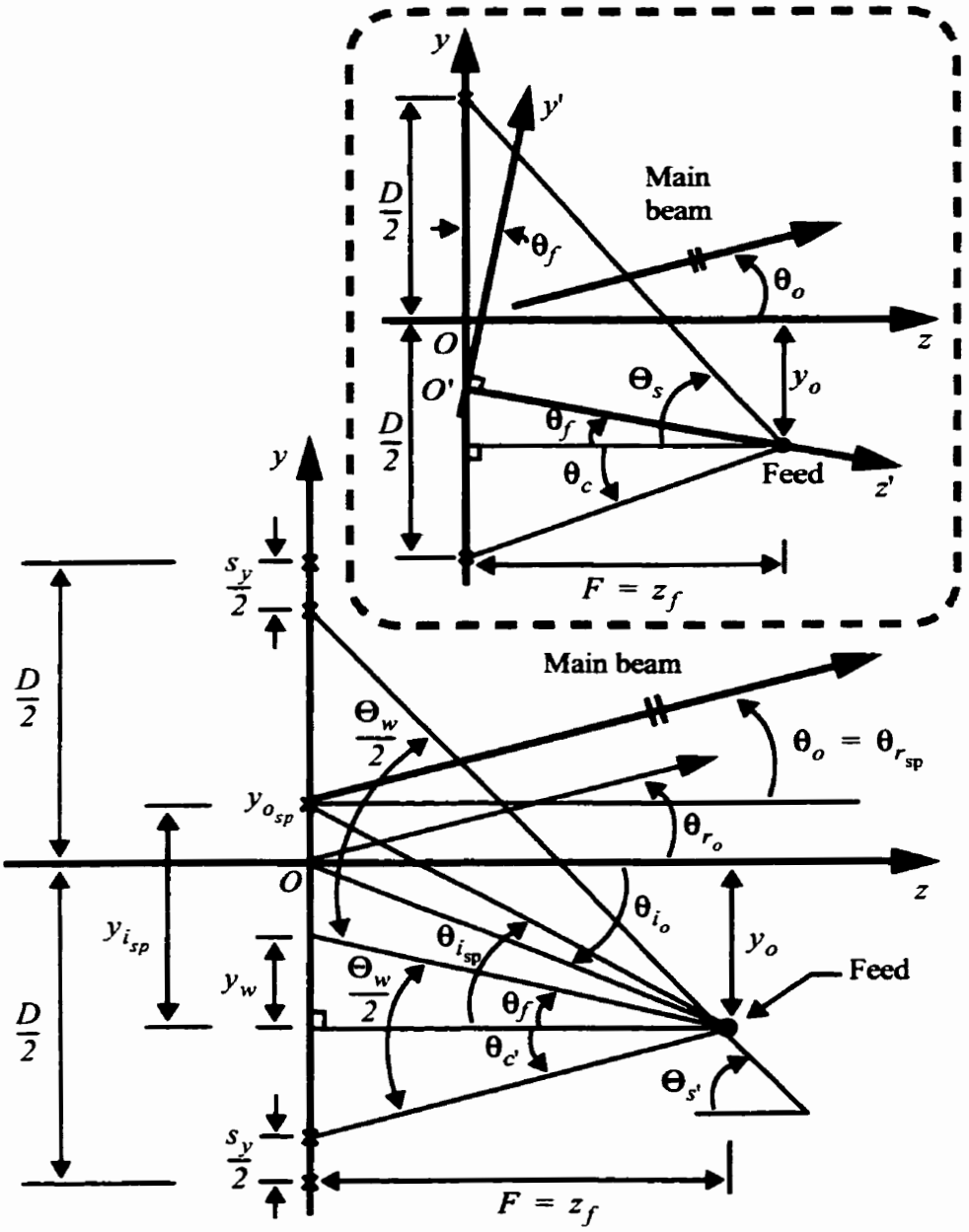

Fig. 5-1: yz-plane geometrical configurations of an offset-fed microstrip reflectarray, with an x-polarized $\hat{E}$ field from the line-source feed.

array in the y-direction is defined as

$$\Theta_w = \Theta_{s'} + \theta_{c'}, \tag{5-1}$$

where

$$tan\Theta_{s'} = \frac{(D - s_y)/2 + y_o}{z_f}, \tag{5-2a}$$

$$tan\theta_{c'} = \frac{(D - s_y)/2 - y_o}{z_f}, \tag{5-2b}$$

$0° < \Theta_w < 180°$, $0° \le \theta_n < \Theta_{s'}$ for patches at locations $y \ge -y_o$ on the microstrip patch array, $0° \le \theta_n < \theta_{c'}$ for patches at locations $y < -y_o$ on the patch array, and y_o is the feed offset distance below the z-axis. Parameters θ_n, D, s_y and z_f are as previously defined in Chapter 3.

The feed is aimed at an angle $\Theta_w/2$ onto a location on the patch array which is at y_w distance above the feed in the y-direction. The feed tilt angle is then given as

$$\theta_f = \frac{\Theta_w}{2} - \theta_{c'}, \tag{5-3}$$

such that,

$$tan\theta_f = \frac{y_w}{z_f}, \tag{5-4}$$

where $0° \leq \theta_f < 90°$.

It is assumed, that, at a location $y = y_{o_{sp}}$ on the patch array, there is a specular reflection angle $\theta_{r_{sp}}$ which equals the reflectarray main beam angle θ_o, where $0° < \theta_o < 90°$ and $y_{o_{sp}}$ is the y-coordinate of the location. Then, $\theta_{i_{sp}} = \theta_{r_{sp}} = \theta_o$, where $0° \leq \theta_{i_{sp}} < 90°$, $0° \leq \theta_{r_{sp}} < 90°$ and $\theta_{i_{sp}}$ is the corresponding incidence angle of feed illumination onto $y = y_{o_{sp}}$ on the array. This gives

$$tan\theta_{i_{sp}} = tan\theta_{r_{sp}} = \frac{y_{i_{sp}}}{z_f} \tag{5-5}$$

and

$$y_{o_{sp}} = y_{i_{sp}} - y_o, \tag{5-6}$$

where $y_{i_{sp}}$ is the offset distance of the location above the feed.

5.1.2 Feed Position, Orientation and Near-Field Characteristics

Referring to Fig. 5-1, for the given dimensions $D = 38.75$cm and $s_y = 1.25$cm, and by arbitrarily selecting $\Theta_s = 48°$ and $\theta_c = 20°$ for the offset-fed configuration, the feed is repositioned to a newly calculated location in the near-field region, at $(x, y, z) = (0, -9.810, 26.279)$cm, from its previous position discussed in Chapter 3.

This provides a $y_o = 9.810$cm offset below the z-axis and $z_f = 26.279$cm. Hence, $F/D = 1.475$. Fig. 5-2 depicts this new feed position, with $\Theta_{s'} = 47.38°$ and $\theta_{c'} = 18.79°$, as evaluated from (5-2a) and (5-2b), respectively.

From (5-3), the feed is aimed at $\theta_f = 14°$. This feed direction is along the z'-axis which intercepts the microstrip patch array at $y = -3.258$cm, as determined from (5-4), where the $y'z'$-axes constitute the coordinate system for near-field feed computations.

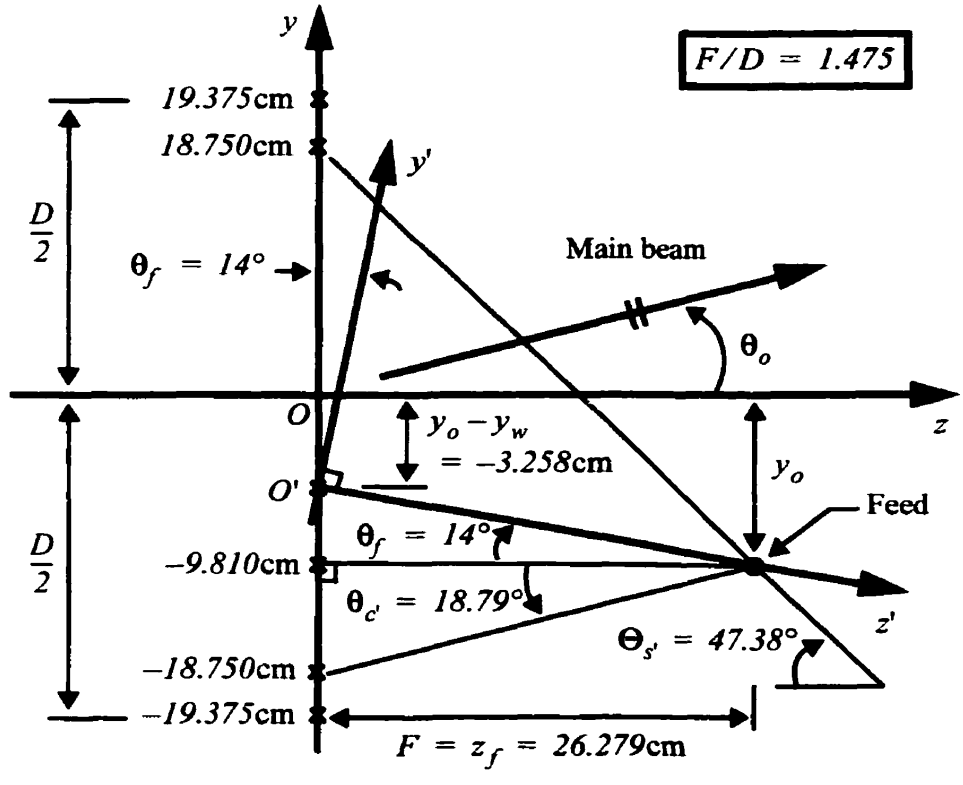

Fig. 5-2: A simplified yz-plane geometrical configuration of an offset-fed microstrip reflectarray, illustrating some important y-coordinate positions on the microstrip patch array.

Since the reflectarray F/D ratio is large, the large H-plane ($\phi = \pm 90^o$) single line-source beamwidth must be reduced so that the spillover loss is small. As such, a double line-source feed is considered, which generates a more directive H-plane ($\phi = \pm 90^o$) feed beam, if the line-source separation in the y'-direction, $d_{y'}$, is properly chosen.

To ensure that $d_{y'}$ provides a single main-lobe for the double line-source, so that the spill-over loss due to side-lobes is minimized, the restriction $d_{y'} \leq 0.5\lambda$ is enforced. The near-fields of both single and double line-sources for a center frequency $f_o = 11.761$GHz, at patch locations along the y-direction of the patch array, are plotted in Fig. 5-3 for a uni-

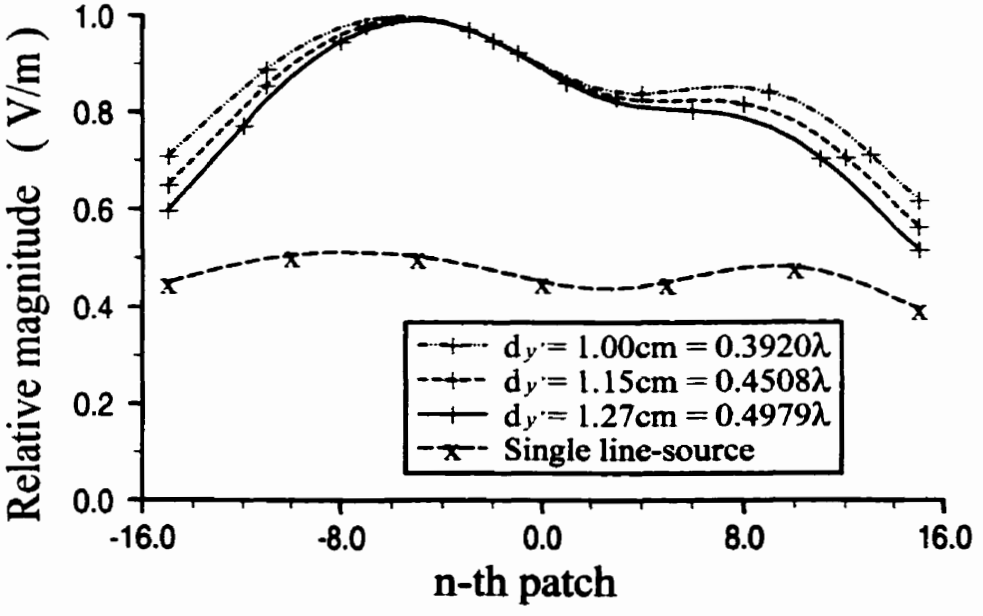

Fig. 5-3: Comparisons of near-field relative magnitudes along the y-axis for the offset-fed configuration, due to single and double line-source feeds, with $f = 11.761$GHz, $s_y = 1.25$cm and uniform line-source distributions.

form line-source distribution. Near-field oscillations due to these line-sources are included in subsequent reflectarray simulations.

5.1.3 Main Beam Direction

The required phase corrections, to be produced by the microstrip patches in the array, are given as

$$\psi_n = \psi_i - \beta_o, \tag{5-7}$$

where ψ_i and β_o are as previously defined for (3-19) in Chapter 3.

By scanning the reflectarray beam away from the feed to decrease blockage, the variation of ψ_n with θ_n, and consequently with y, can be reduced. This phase sensitivity behavior is attributed to ψ_n having exponential increments, because of its dependency on the phase delay ψ_i, as given in (5-7).

Associated with phase delay ψ_i is a phasal local minimum which coincides with the location of the shortest path length, in the yz-plane, between the patch array and the feed. Consequently, associated with ψ_n is a phasal local minimum that is dependent on β_o, and thus, main beam angle θ_o. For $\theta_o = 0^o$, $\beta_o = 0$, and thus, $\psi_n = \psi_i$, which certainly produces a local minimum that coincides with the shortest path length location mentioned above.

To determine the location of this minimum, the assumption $\theta_o = \theta_{r_{sp}} = \theta_{i_{sp}}$ is employed. Since near-field oscillations due to the line-source are included into the analysis, the $m = 6$ column of a 41×31-element microstrip patch array (i.e. with 41 columns and 31 rows) is arbitrarily selected for illustration. For this patch column, local minima for $\theta_o = 0^o, 25^o$ and 34^o are computed from (5-5) and (5-6), to be positioned at $y = y_{o_{sp}} = -9.810$cm, 2.444cm and 7.915cm, respectively. This demonstrates, that, for this specified configuration, the minimum point shifts in the direction of increasing y for increasing θ_o, as illustrated in Fig. 5-4.

For a quantitative phase sensitivity analysis, (4-5) of Chapter 4 is modified for the offset-fed configuration of Fig. 5-1. The rate of change of ψ_n with respect to θ_i at $\theta_i = \theta_n$ for a given "focal" length F, i.e. $(d\psi_n / d\theta_i)\big|_{\theta_i = \theta_n}$, is

$$\frac{2}{k_o \tilde{D}_N}\left(\frac{d\psi_n}{d\theta_i}\right)\bigg|_{\theta_i = \theta_n} = \frac{\sqrt{[1-(2\tilde{Y}_N)^{-1}]^2 + [2(F/\tilde{D}_N)]^2}}{2(F/\tilde{D}_N)}, \tag{5-8a}$$

where

$$0 \le \frac{d\psi_n}{d\theta_i}\bigg|_{\theta_i < \theta_n} < \frac{d\psi_n}{d\theta_i}\bigg|_{\theta_i = \theta_n}, \tag{5-8b}$$

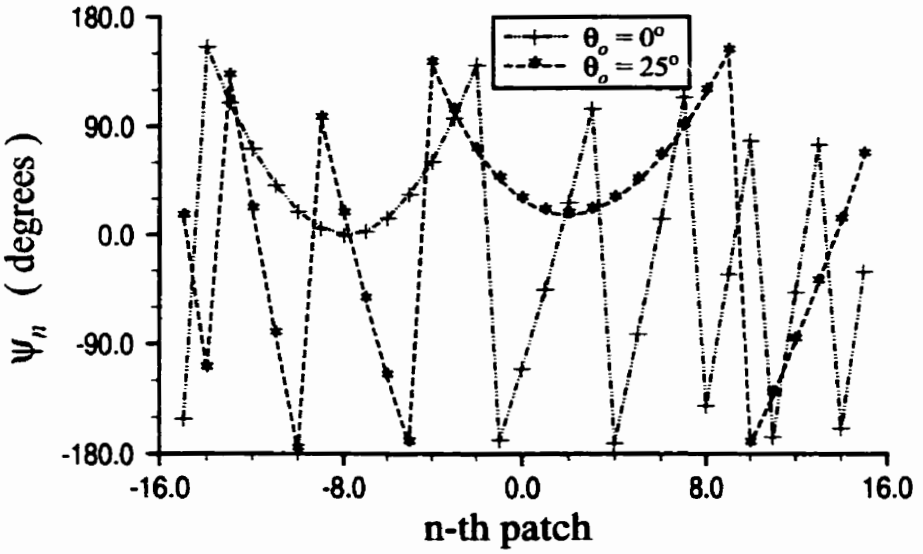

(a)

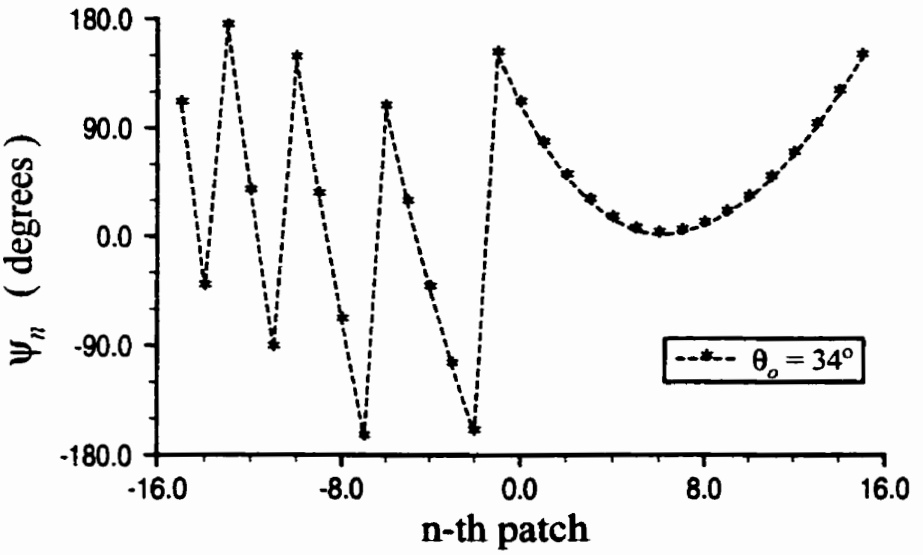

(b)

Fig. 5-4: Required phase correction ψ_n, due to the n-th patch, along the $m = 6$ column of a 41×31-element microstrip patch array: (a) $\theta_o = 0^o$ and 25^o, and (b) $\theta_o = 34^o$. $f = 11.761$GHz and $s_y = 1.25$cm.

$$\frac{\tilde{D}_N}{2} = \begin{cases} |y| - y_{o_{sp}} ; & \text{for} \quad y \geq y_{o_{sp}} \\ |y| + y_{o_{sp}} ; & \text{for} \quad y < y_{o_{sp}} \end{cases} \tag{5-8c}$$

and

$$\tilde{Y}_N \; s_y = \begin{cases} y - y_{o_{sp}} ; & \text{for} \quad y \geq y_{o_{sp}} \\ -y + y_{o_{sp}} ; & \text{for} \quad y < y_{o_{sp}} \end{cases} . \tag{5-8d}$$

Since

$$\lim_{F \to \infty} \left[\frac{2}{k_o \tilde{D}_N} (d\psi_n / d\theta_i) \Big|_{\theta_i = \theta_n} \right] = 1 , \tag{5-9}$$

the phase sensitivity $\frac{2}{k_o \tilde{D}_N} (d\psi_n / d\theta_i) \Big|_{\theta_i = \theta_n}$ is evaluated as percentage error

$$\wp = \left[\frac{2}{k_o \tilde{D}_N} (d\psi_n / d\theta_i) \Big|_{\theta_i = \theta_n} - 1 \right] \cdot 100\% . \tag{5-10}$$

Table 5-1: Phase sensitivities at selected locations along the $m = 6$ column of the patch array for the offset-fed configuration, with $F = z_f = 26.279$cm, $D = 38.750$cm, $s_y = 1.250$cm and $y_o = 9.810$cm.

Main beam angle, θ_o	Position of local minimum, $y = y_{o_{sp}}$ (cm)	Phase sensitivity, $\wp$ (percent) †		
		At $n = 15$ ($y = 18.750$cm)	At $n = 0$ ($y = 0$cm)	At $n = -15$ ($y = -18.750$cm)
0^o	-9.810	3.4712	0.3811	0.3124
25^o	2.444	1.1067	0.0150	1.8965
34^o	7.915	0.4706	0.2402	3.0228

† *For the center-fed configuration of Chapter 3, $\wp = 60.0781\%$ at $n = \pm 15$ along the $m = 6$ column.*

Table 5-1 shows the computed phase sensitivities $\wp$ for different θ_o at selected locations on the patch array. As expected, edge elements farthest from the minimum locations generally exhibit the highest phase sensitivities. These are also graphically illustrated in Fig. 5-4 for $\theta_o = 0^o$ and $\theta_o = 25^o$.

For minimum phase error in the offset-fed configuration, the local minimum should be positioned at $y = 0$ for the offset-fed configuration. With reference to Fig. 5-1, and as

determined from (5-5) and (5-6), this necessitates that $\theta_o = \theta_{r_{sp}} = \theta_{r_o} = \theta_{i_o} = 20.47°$. This criterion also minimizes beam squint effects in the main beam when the frequency is scanned [39][40].

But, since $\theta_{c'} = 18.79°$, as determined from (5-2b), utilizing $\theta_o = 20.47°$ in the design, may not provide adequate clearance for avoiding significant feed blockage in the near-field zone, which requires that $\theta_o \gg \theta_c$. Resolving these issues, $\theta_o = 25^o$ is selected.

For $\theta_o = 25^o$, the required phase correction ψ_n in Fig. 5-4, due to the n-th patch, is replotted as a phase curve due to θ_n in Fig. 5-5(a). In the new figure, $\phi_i = 90^o$ corresponds to locations on the patch array above the feed, i.e. for $y > -3.258$cm, while $\phi_i = -90^o$ corresponds to locations on the patch array below the feed, i.e. for $y < -3.258$cm, where θ_i and ϕ_i are previously defined in Chapter 3 for the infinite periodic array modelling.

Since $\theta_{i_{sp}} = \theta_{r_{sp}} = \theta_o$, a phasal local minimum occurs at $\theta_n = \theta_i = 25^o$ in Fig. 5-5(a). That is, for a given θ_o, in general, the phasal local minimum occurs at $\theta_n = \theta_i = \theta_o$.

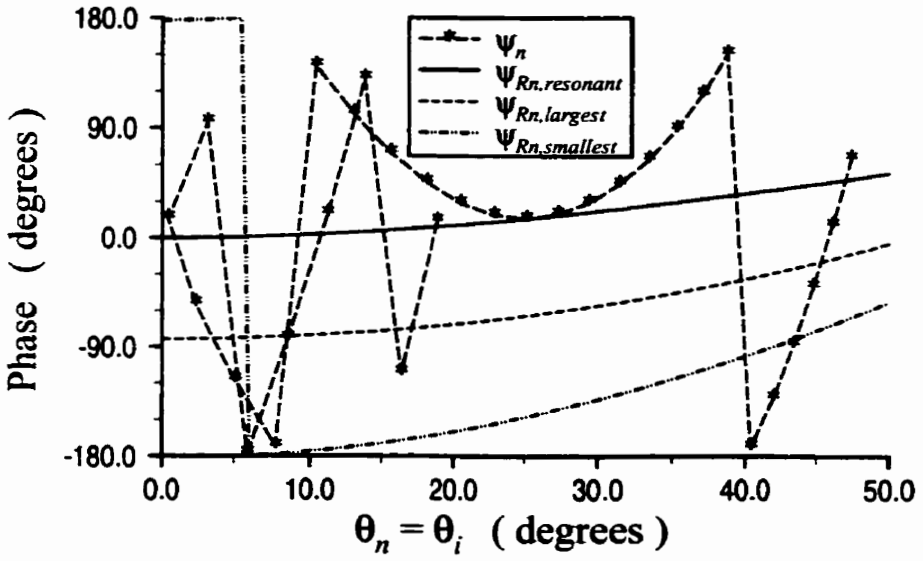

(a)

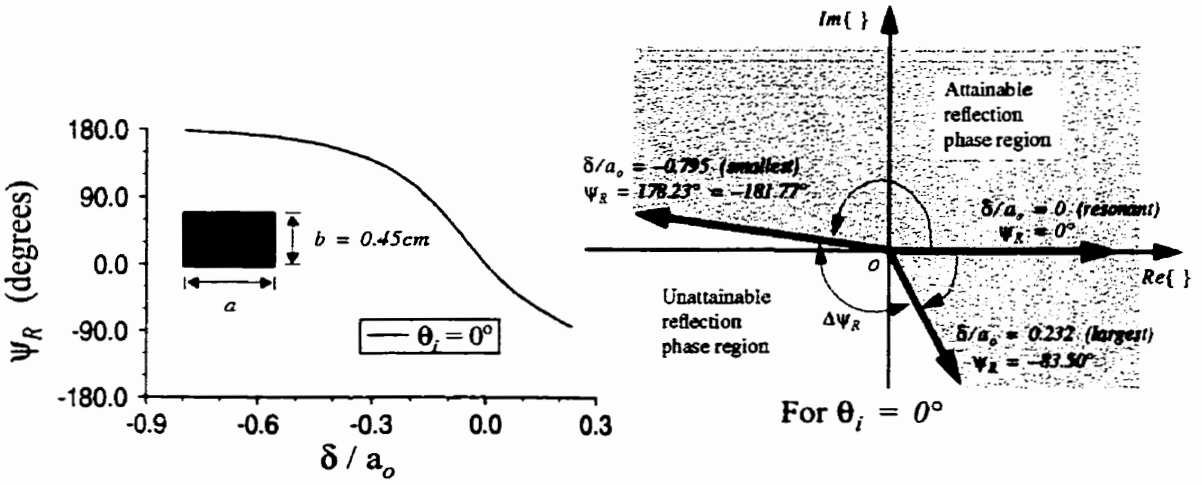

(b)

Fig. 5-5: Phase curves for the offset-fed microstrip reflectarray at $f = 11.761$GHz, for rectangular patches: (a) phase curves ψ_n and TE-to-z reflection phase curves ($\psi_{Rn,\text{ resonant}}$ for $a = a_o = 0.974$cm, $\psi_{Rn,\text{ largest}}$ for $a = 1.200$cm, and $\psi_{Rn,\text{ smallest}}$ for $a = 0.200$cm), due to incident angle $\theta_n = \theta_i$ along the $m = 6$ column of the patch array, and (b) TE-to-z reflection phase due to δ/a_o, and its corresponding phase diagram, for normal incidence ($\theta_i = 0°$). $\varepsilon_r = 1.03$, $z_a = 0.317$cm, $a_o = 0.974$cm and $b = 0.45$cm.

5.2 PATCH ARRAY AND FAR-FIELD RADIATION ANALYSES

A substrate thickness $z_a = 0.317\text{cm}$, with $\varepsilon_r = 1.03$, is chosen for an offset-fed single-layer microstrip reflectarray having its main beam directed at $\theta_o = 25^o$ for a center frequency $f_o = 11.761\text{GHz}$. It is consist of a 41×31-element microstrip patch array. For both rectangular and combination patch arrays considered, the widths of all the rectangular patches are $b = 0.45\text{cm}$, while the dimensions of all other patch geometries remain the same as those in the center-fed configurations, as in Chapter 3 and Chapter 4. Only patch length a are varied to obtain field collimation for the desired main beam direction.

5.2.1 Patch Array Symmetry

For an offset-fed configuration, computations are necessary only for a half section of the $M \times N$-element patch array due to symmetry, so that computation speed and efficiency are enhanced. M and N represent the number of elements in each column and row in the array, respectively.

Because of (3-23) in Chapter 3, (3-21) in that chapter, as applied to the offset-fed configuration, is simplified to

$$E_{MN}^{(ap)}(\theta, \phi) = \sum_{m=0}^{M} \sum_{n=-N}^{N} I_{mn} f_m g_n, \tag{5-11}$$

where

$$f_m = \begin{cases} e^{j\psi_m(\theta,\phi)} & ; \quad \text{for } m = 0 \\ 2\cos[\psi_m(\theta,\phi)] & ; \quad \text{for } m = 1, 2, 3, \ldots \end{cases} \tag{5-12a}$$

$$g_n = e^{j\psi_n(\theta,\phi)} \quad ; \quad \text{for n} = 0, \pm 1, \pm 2, \ldots \tag{5-12b}$$

$$I_{mn} = R_n E_{mn}^{(fd)} e^{j\beta_o} \quad ; \quad \text{for } m = 0, 1, 2, \ldots \text{ and } n = 0, \pm 1, \pm 2, \ldots \tag{5-12c}$$

These formulations are then utilized for the far-field radiation analysis of an offset-fed configuration consisting of a 41×31 -element microstrip patch array.

5.2.2 Rectangular Patch Array

The TE-to-z reflection phase curve $\psi_{Rn,\,\text{resonant}}$ in Fig. 5-5(a), for the resonant microstrip patch where $a = a_o = 0.974$cm, indicates that the patch produces the required phase correction at $\theta_n = \theta_i \approx 25^o$ for $\theta_o = 25^o$. Thus, the patches in the vicinity of the local minimum are generally consist of near-resonant patches.

Furthermore, the phase curves $\psi_{Rn,\,\text{largest}}$ and $\psi_{Rn,\,\text{smallest}}$ in the figure, for the largest and smallest microstrip patches, i.e. $a = 1.200$cm and $a = 0.200$cm, respectively, define the unattainable reflection phase range of the microstrip patch array, while their corresponding phase diagram is depicted in Fig. 5-5(b), similar to those in Chapter 3.

The empirical formulations (4-1)-(4-3), presented in Chapter 4, are utilized to determine the required patch lengths $a_{n,\,emp}$ for the 41×31 -element array, as a quick first-pass solution. Although this solution is relatively accurate, as proven in Chapter 4, a further optimization of the solution is easily performed using the full wave analysis and through minor tuning of the patch lengths individually.

With near-field oscillations due to the line-source feed included, resulting patch lengths a_n for the $m = 6$ column of the array are illustrated in Fig. 5-6(a). Their corresponding achieved reflection phases ψ_{Rn} are depicted in Fig. 5-6(b).

The percentage errors for $a_{n,\,emp}$, obtained through the empirical formulation, are presented in Fig. 5-7(a), which shows good accuracy of the patch lengths, especially for the near-resonant patch lengths. A comparison of the reflectarray directive gain patterns, provided in Fig. 5-7(b) for the single line-source feed configuration, also exhibits excellent accuracy of the empirical results.

5.2.3 Double Line-Source Feed

To decrease the spillover loss for an offset-fed reflectarray, the uniform distribution double line-source feed, previously discussed in Section 5.1.2 of this chapter, is utilized. The line-source separation $d_y = 0.5\lambda$ is selected, where λ is the wavelength, since it pro-

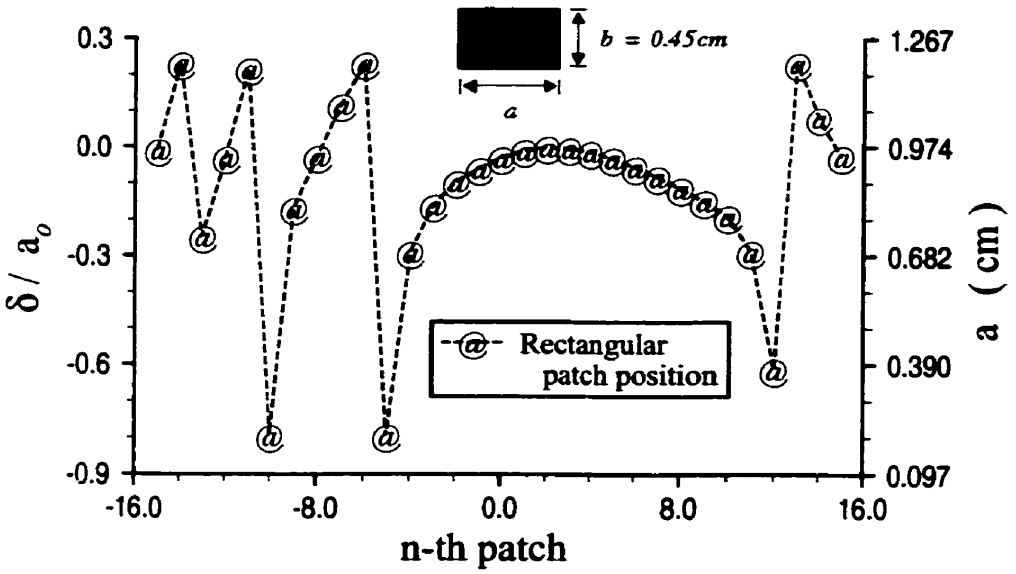

(a)

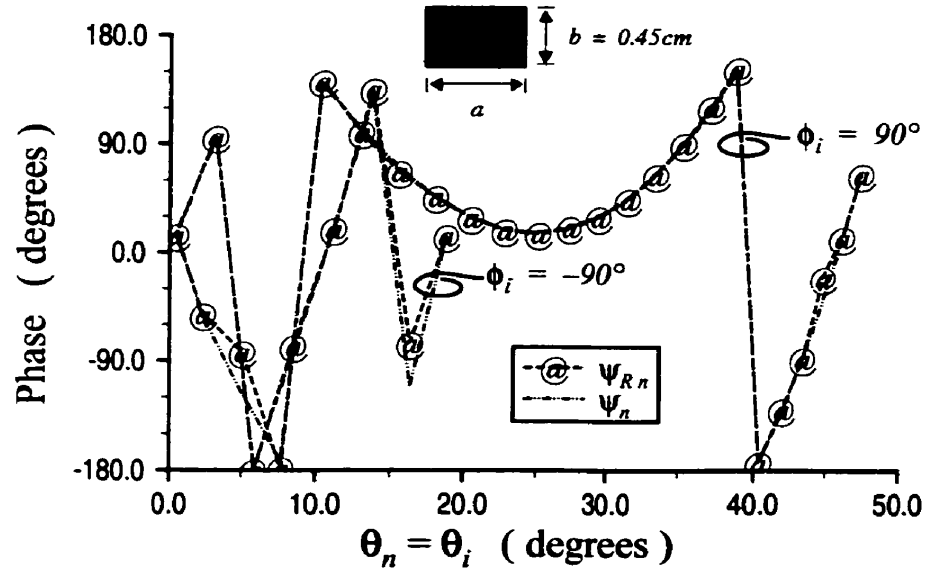

(b)

Fig. 5-6: Phase correction along the $m = 6$ column of a 41×31-element rectangular microstrip patch array at $f = 11.761$GHz: (a) patch lengths a_n for the array column, and (b) achieved reflection and required phases, ψ_{Rn} and ψ_n, respectively. $\varepsilon_r = 1.03$, $z_a = 0.317$cm, $a_o = 0.974$cm and $b = 0.45$cm.

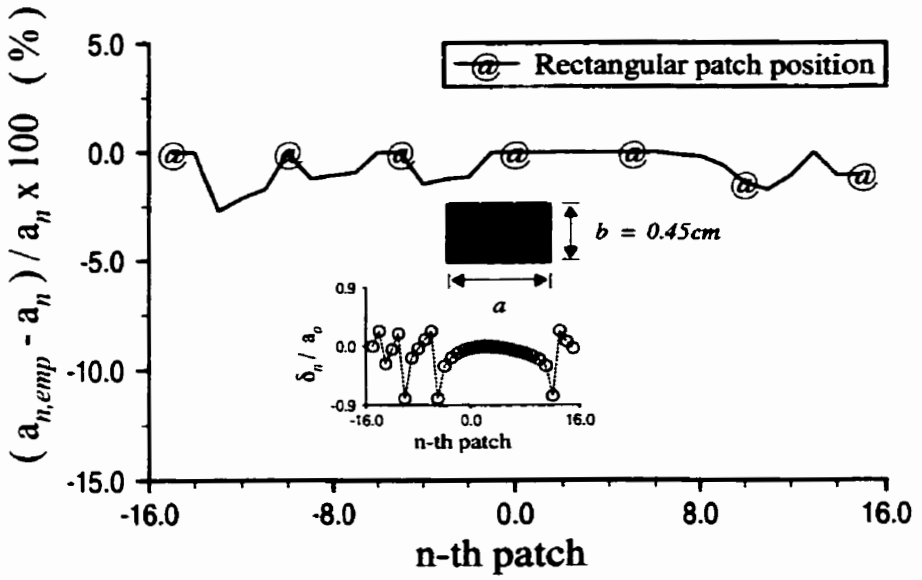

(a)

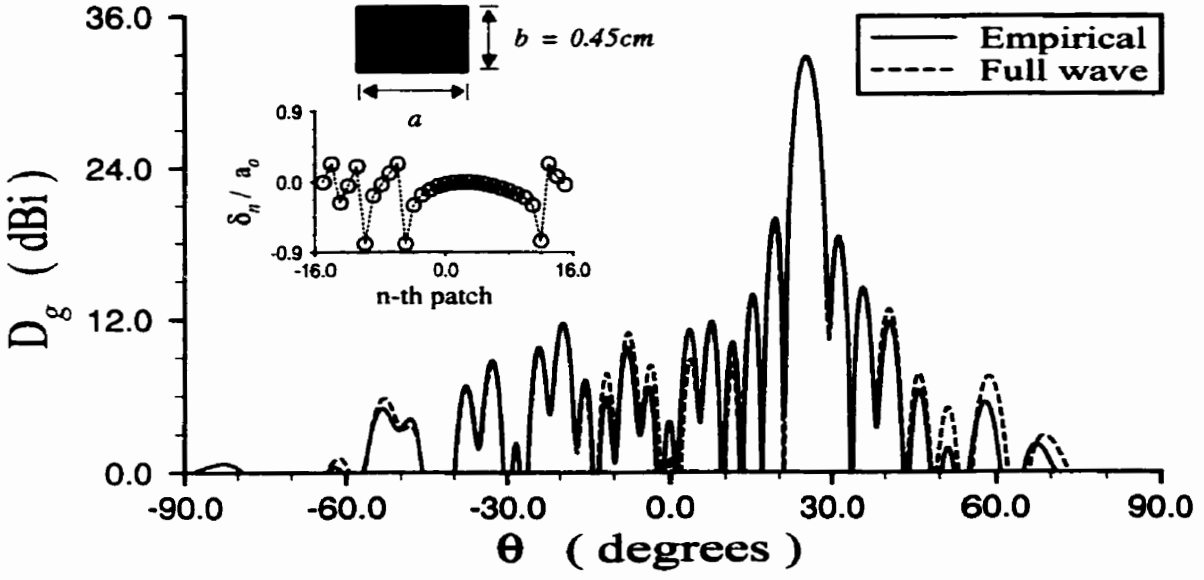

(b)

Fig. 5-7: Solutions from empirical formulations and full wave analysis evaluated at $f = 11.761$GHz, for an offset-fed microstrip reflectarray with a single line-source feed and a 41×31-element rectangular patch array: (a) percentage errors of patch lengths $a_{n,\,emp}$ along the $m = 6$ column of the array, due to empirical formulations, and (b) reflectarray H-plane ($\phi = \pm 90^{o}$) directive gain patterns D_g. $\varepsilon_r = 1.03$, $z_a = 0.317$cm, $a_o = 0.974$cm and $b = 0.45$cm.

duces the most directive H-plane ($\phi = \pm 90^o$) feed beam for no side-lobes, as is evident in Fig. 5-3.

For the double line-source feed at $f = 11.761$GHz, the patch array edge illuminations along the y-axis are -4.40dB and -5.66dB at $n = -15$ and $n = 15$, respectively. Consequently, given that the patch array lengths along the x- and y- directions are $41s_x = 21.117\lambda$ and $31s_y = 15.708\lambda$, respectively, the reflectarray spillover loss is significantly reduced from that of the single line-source feed, as indicated in Table 5-2.

Table 5-2: Performance of offset-fed microstrip reflectarrays with single and double line-source feeds, 41×31-element rectangular patch arrays and uniform line-source distributions. $f = 11.761$GHz, $\varepsilon_r = 1.03$, $z_a = 0.3170$cm, $z_f = 26.279$cm, $\theta_o = 25^o$, $a_o = 0.974$cm and $b = 0.45$cm. Values in brackets are for the ideal patch array having no phase correction error.

Properties	Single line-source	Double line-source ($d_y = 1.27$cm)
D_o (dBi)	32.83 [33.04]	34.55 [34.75]
θ_o	24.97^o [24.98^o]	24.97^o [24.97^o]
HPBW ($\phi = 90^o$)	3.77^o [3.75^o]	4.03^o [4.01^o]
Max. SLL ($\phi = 90^o$) (dB)	-13.42 [-13.69]	-16.24 [-16.56]
Loss in directivity (dB)	0.21	0.20
Spillover (percent)	41.94	11.56

Comparing reflectarray far-field radiation characteristics between configurations with single and double line-source feeds, and with reference to Table 5-2 and Fig. 5-8, the directivity D_o for the reflectarray with a double line-source feed is improved by *1.72*dB. Furthermore, its initial SLL are also decreased, but at the expense of increased SLL at observation angles far from the main-lobe.

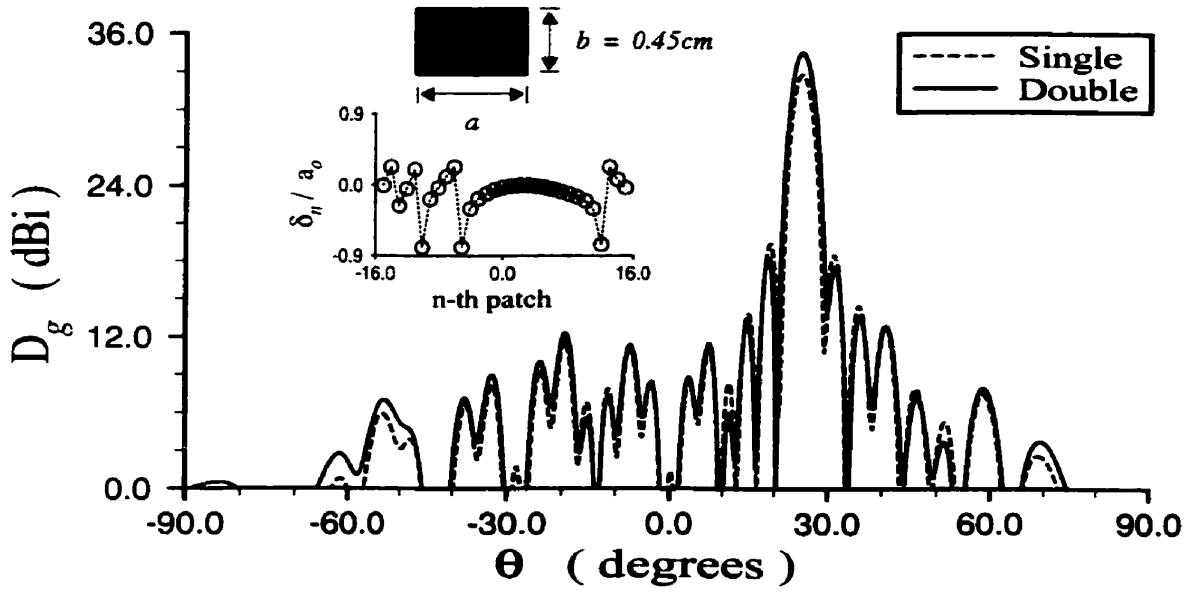

Fig. 5-8: Reflectarray H-plane ($\phi = \pm 90^o$) directive gain patterns D_g at $f = 11.761$GHz, for offset-fed microstrip reflectarrays with single and double line-source-feeds, and 41×31-element rectangular patch arrays. $\varepsilon_r = 1.03$, $z_a = 0.317$cm, $a_o = 0.974$cm and $b = 0.45$cm.

5.2.4 Combination Patch Array Fed by A Double Line-Source

Fig. 5-9 illustrates the TE-to-z reflection coefficient phases at normal incidence for different microstrip patch geometries, evaluated at $f = 11.761$GHz, with $\varepsilon_r = 1.03$,

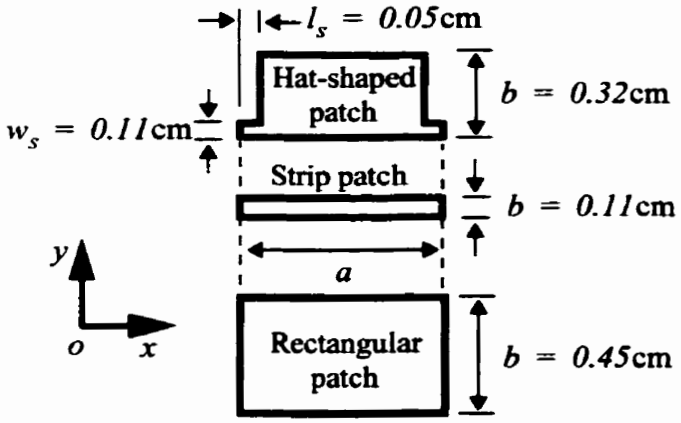

(a)

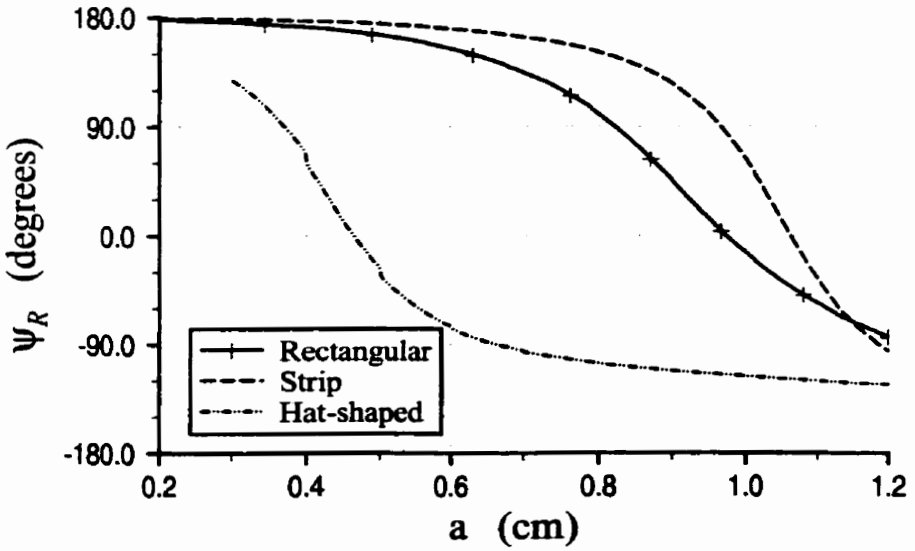

(b)

Fig. 5-9: Comparisons between different microstrip patch geometries at $f = 11.761$GHz: (a) patch geometry schematics, and (b) corresponding TE-to-z reflection phase curves at normal incidence ($\theta_i = 0^o$). $\varepsilon_r = 1.03$ and $z_a = 0.317$cm.

$z_a = 0.317$cm and varying a. The reflection phases of the hat-shaped and strip patches extend into the unattainable phase range of the rectangular patch, similar to those in Chapter 3.

Thus, in the single-layer microstrip reflectarray, the hat-shaped and strip patches can substitute rectangular patches at locations where the required reflection phase corrections coincide with the unattainable phase ranges of the rectangular patches [85], as discussed in Chapter 3. However, mutual coupling between patches of different geometrical shapes are not accurately accounted, because of the infinite periodic array modelling utilized. Comparisons for the best phase corrections between different patch geometries are tabulated in Table 5-3.

To improve phase corrections of the patch array, rectangular, strip and hat-shaped patches are implemented into the array as a combination patch array. Patch lengths for the $m = 6$ column of the 41×31 -element rectangular and combination arrays are shown in Fig. 5-10(a).

5.2.5 Far-Field Radiation at Center Frequency

Assuming that the double line-source possesses adequate impedance band, the reflectarray radiation patterns and spillover losses are affected by its feed. Furthermore, near-field oscillations, due to the double line-source feed, are also included in the far-field computations.

Table 5-3: Comparisons for the best phase corrections between rectangular, strip and hat-shaped patches in the offset-fed design. $\psi_n = \psi_i - \beta_o$ is the required phase correction, $|\Delta\psi_{Rn}| = |\psi_{Rn} - \psi_n|$ is the phase correction error and $f = 11.761$GHz.

n-th patch	$\theta_n = \theta_i$	ψ_n	$\varepsilon_r = 1.03$ with $z_a = 0.3170$cm								
			Rectangular patches, $b = 0.45$cm			Strip patches, $b = 0.11$cm			Hat-shaped patches, $b = 0.32$cm, $w_s = 0.11$cm and $l_s = 0.05$cm		
			ψ_{Rn}	a_n (cm)	$\lvert\Delta\psi_{Rn}\rvert$	ψ_{Rn}	a_n (cm)	$\lvert\Delta\psi_{Rn}\rvert$	ψ_{Rn}	a_n (cm)	$\lvert\Delta\psi_{Rn}\rvert$
−14	*16.31°* ($\phi_i = -90°$)	*−111.60°*	*−75.34°* (Not utilized)	*1.2000*	*36.26°*	*−85.64°* (Not utilized)	*1.2000*	*25.96°*	*−111.58°* (Utilized)	*1.1490*	*0.02°*
−11	*8.53°* ($\phi_i = -90°$)	*−83.02°*	*−81.27°* (Not utilized)	*1.2000*	*1.75°*	*−83.10°* (Not utilized)	*1.1780*	*0.08°*	*−82.98°* (Utilized)	*0.6270*	*0.04°*
−10	*5.84°* ($\phi_i = -90°$)	*−177.94°*	*−179.90°* (Not utilized)	*0.2000*	*1.96°*	*−179.00°* (Utilized)	*0.2000*	*1.06°*	*129.26°* (Not utilized)	*0.3000*	*52.80°*
−6	*5.02°* ($\phi_i = -90°$)	*−117.47°*	*−82.72°* (Not utilized)	*1.2000*	*34.75°*	*−94.40°* (Not utilized)	*1.2000*	*23.07°*	*−117.52°* (Utilized)	*1.0660*	*0.05°*
−5	*7.72°* ($\phi_i = -90°$)	*−172.31°*	*−178.51°* (Not utilized)	*0.2000*	*6.2°*	*−177.61°* (Utilized)	*0.2000*	*5.3°*	*132.69°* (Not utilized)	*0.3000*	*55.00°*
13	*44.76°* ($\phi_i = 90°$)	*−39.97°*	*−20.67°* (Not utilized)	*1.2000*	*19.30°*	*−22.32°* (Not utilized)	*1.2000*	*17.65°*	*−39.92°* (Utilized)	*1.2000*	*0.05°*

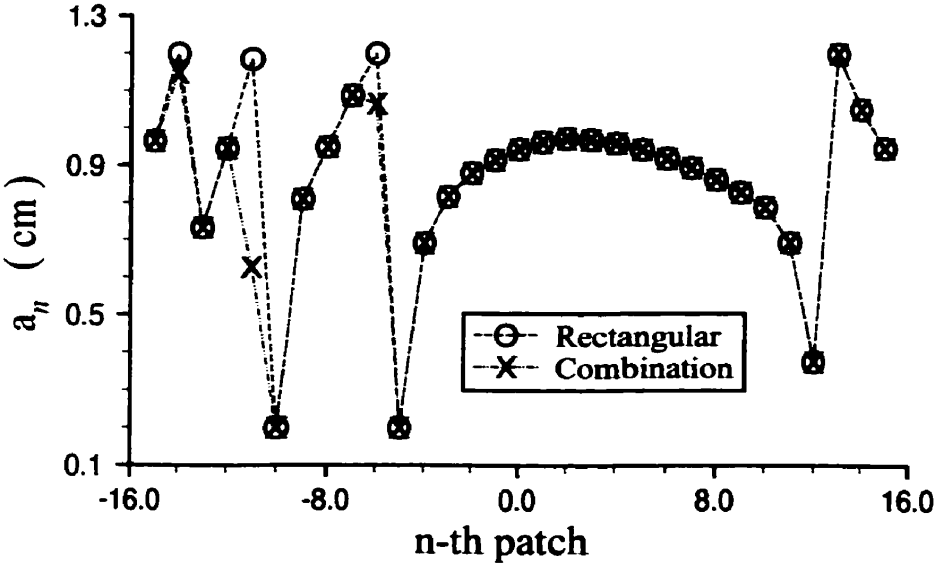

(a)

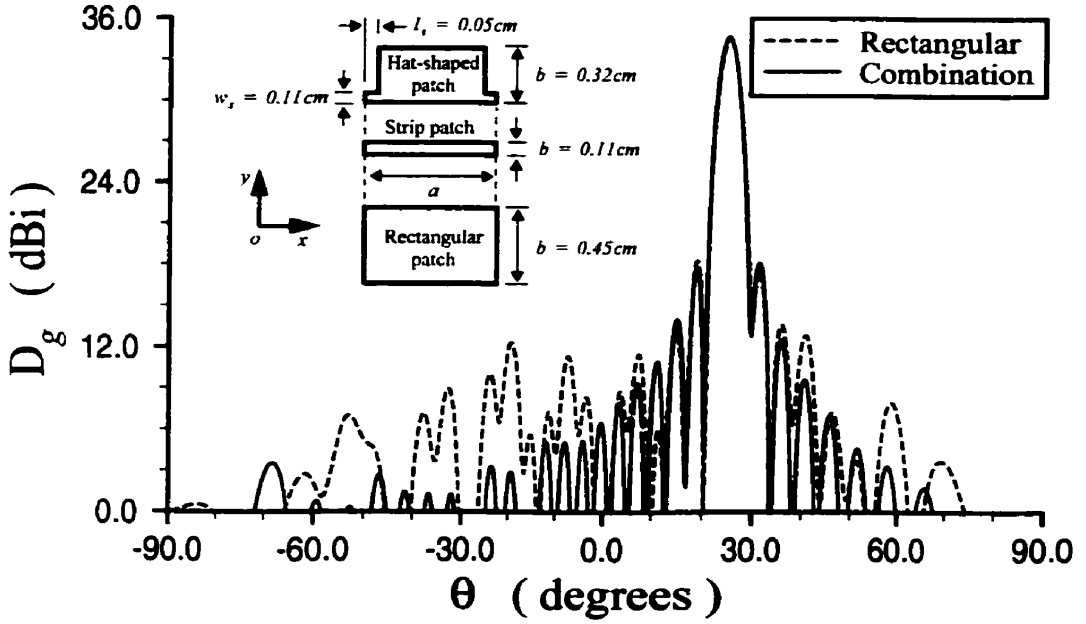

(b)

Fig. 5-10: Comparisons between rectangular and combination microstrip patch arrays for offset-fed configurations with a double line-source feed, evaluated at $f = 11.761$GHz: (a) patch lengths a_n along the $m = 6$ columns of the arrays, and (b) reflectarray H-plane ($\phi = \pm 90^o$) directive gain patterns D_g. $\varepsilon_r = 1.03$ $z_a = 0.317$cm and patch arrays are consist of 41×31 elements. The combination array is consist of rectangular, strip and hat-shaped patches mentioned in Table 5-3.

The reflectarray H-plane ($\phi = \pm 90^o$) directive gain patterns D_g at center frequency $f_o = 11.761$GHz , for rectangular and combination patch arrays with a double line-source feed, are illustrated in Fig. 5-10(b), where $\theta \geq 90^o$ corresponds to $\phi = 90^o$, and $\theta < -90^o$ to $\phi = -90^o$. In the figure, both main beams are directed at $\theta = \theta_o = 25^o$ with approximately equal directivities D_o. However, the side-lobe levels (SLL) at observation angles far from the main-lobes are improved in the combination patch array, at the expense of slightly higher initial SLL, as compared to that of the rectangular case. These observations reflect similarities to those for center-fed configurations in Chapter 3.

In general, because of the line-source feeds, differences in the reflectarray far-field radiation patterns between rectangular and combination patch arrays are significant in the H-plane ($\phi = \pm 90^o$), but are negligible in the E-plane ($\phi = \pm 0^o$). Additional reflectarray radiation characteristics are tabulated in Table 5-4.

Table 5-4: H-plane ($\phi = 90^o$) radiation properties of offset-fed microstrip reflectarrays with double line-source feeds, designed using rectangular, strip and hat-shaped patches and illuminated by uniform line-source distributions, over a *10.2%* frequency bandwidth. The patch arrays are consist of 41×31 elements, and the ideal patch array for no phase error is at $f = 11.761$GHz.

Substrate case	Radiation properties	Ideal patch array	Frequency, f (GHz)				
			11.161	*11.561*	*11.761*	*11.961*	*12.361*
$\varepsilon_r = 1.03$ $z_a = 0.3170$cm (rectangular patches only, offset-fed with $z_f = 26.279$cm, desired $\theta_o = 25^o$ and $b = 0.45$cm)	D_o (dBi)	*34.75*	*33.80*	*34.37*	*34.55*	*34.67*	*34.74*
	θ_o	24.97^o	25.15^o	25.03^o	24.97^o	24.91^o	24.79^o
	HPBW ($\phi = 90^o$)	4.01^o	4.24^o	4.11^o	4.03^o	3.96^o	3.86^o
	Max. SLL ($\phi = 90^o$) (dB)	*−16.56*	*−12.37*	*−15.17*	*−16.24*	*−14.96*	*−12.81*
	Loss in directivity (dB)	*0.00*	*0.44*	*0.22*	*0.20*	*0.24*	*0.45*
$\varepsilon_r = 1.03$ $z_a = 0.3170$cm (combination of rectangular, strip and hat-shaped patches mentioned in Table 5-3, off-set-fed with $z_f = 26.279$cm and desired $\theta_o = 25^o$)	D_o (dBi)	*34.75*	*33.88*	*34.39*	*34.67*	*34.81*	*34.88*
	θ_o	24.97^o	25.07^o	24.90^o	24.89^o	24.83^o	24.71^o
	HPBW ($\phi = 90^o$)	4.01^o	4.30^o	4.12^o	4.01^o	3.95^o	3.85^o
	Max. SLL ($\phi = 90^o$) (dB)	*−16.56*	*−12.22*	*−15.28*	*−16.51*	*−15.23*	*−12.64*
	Loss in directivity (dB)	*0.00*	*0.36*	*0.20*	*0.08*	*0.10*	*0.31*

5.2.6 Wideband Performance

Reflectarray directive gain patterns over a *10.2%* frequency bandwidth for the rectangular patch array, shown in Fig. 5-11(a), are compared with the array implemented using a combination of rectangular, strip and hat-shaped patches, depicted in Fig. 5-11(b). For the combination patch array, low SLL at observation angles far from the main-lobe are observed over the *10.2%* bandwidth.

Fig. 5-12(a) indicates a narrowband characteristic for the thin substrate center-fed configuration of Fig. 3-8(a) in Chapter 3, but a wideband characteristic for the offset-fed configuration of Fig. 5-11(a). The difference in ideal directivity D_o between the center- and offset- fed configurations over the *10.2%* bandwidth represents the difference in the amount of power received from the feed (or power loss due to spillover) between the two configurations.

Subsequently, Fig. 5-12(b) reveals a generally higher D_o over the *10.2%* bandwidth, for the combination patch array due to its better phase corrections over the bandwidth. Further confirmation is provided through Fig. 5-13, which illustrates a lower directivity loss (due to minimal phase correction errors) for combination patch array.

In addition, the loss in D_o due to phase correction errors, in Fig. 5-13, are relatively symmetrical about the center frequency $f_o = 11.761$GHz , suggesting that phase corrections deteriorate as the frequency is scanned away from f_o. However, SLL for the combina-

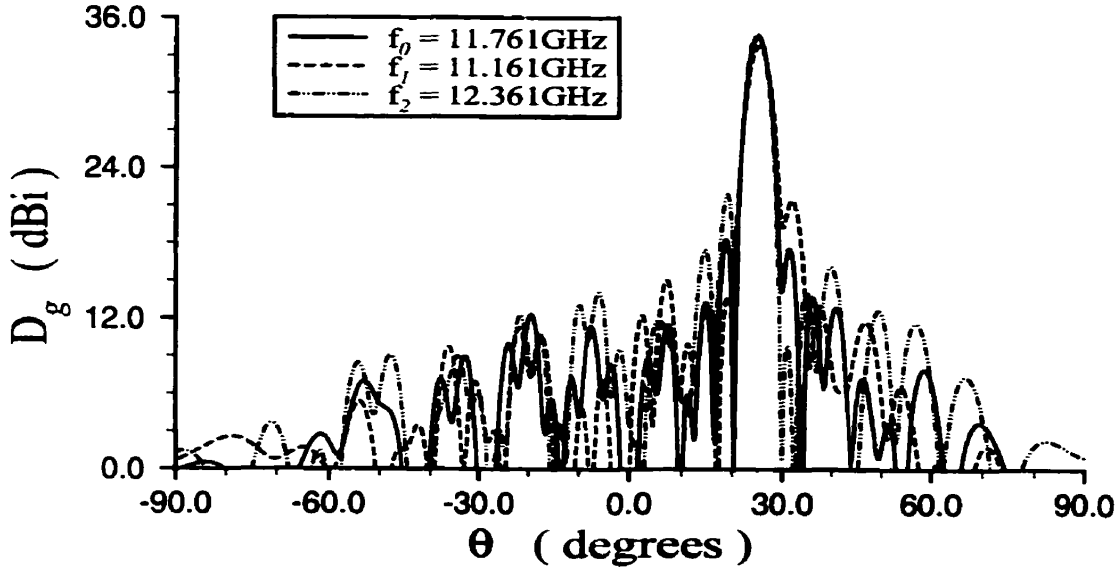

(a)

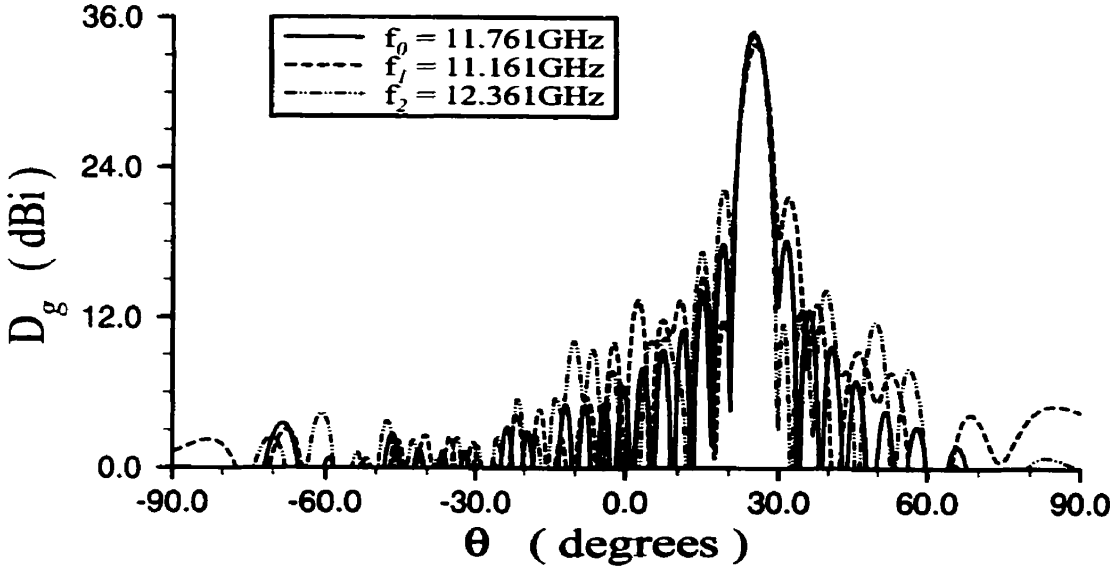

(b)

Fig. 5-11: Reflectarray H-plane ($\phi = \pm 90^o$) directive gain patterns D_g over a *10.2%* frequency bandwidth, for offset-fed microstrip reflectarrays with double line-source feeds: (a) rectangular patch array, with $a_o = 0.974$cm and $b = 0.45$cm, and (b) combination patch array, consisting of rectangular, strip and hat-shaped patches mentioned in Table 5-3. $\varepsilon_r = 1.03$, $z_a = 0.317$cm, and the patch arrays are consist of 41×31 elements.

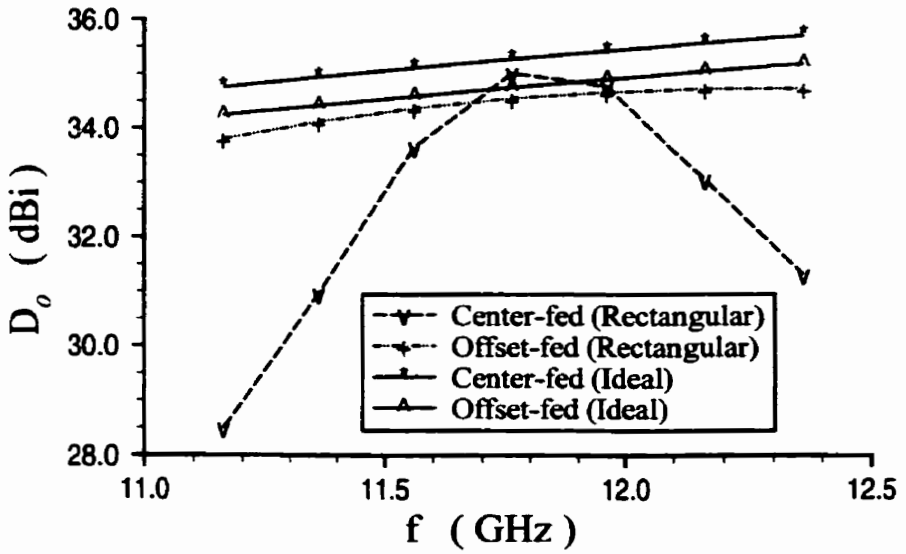

(a)

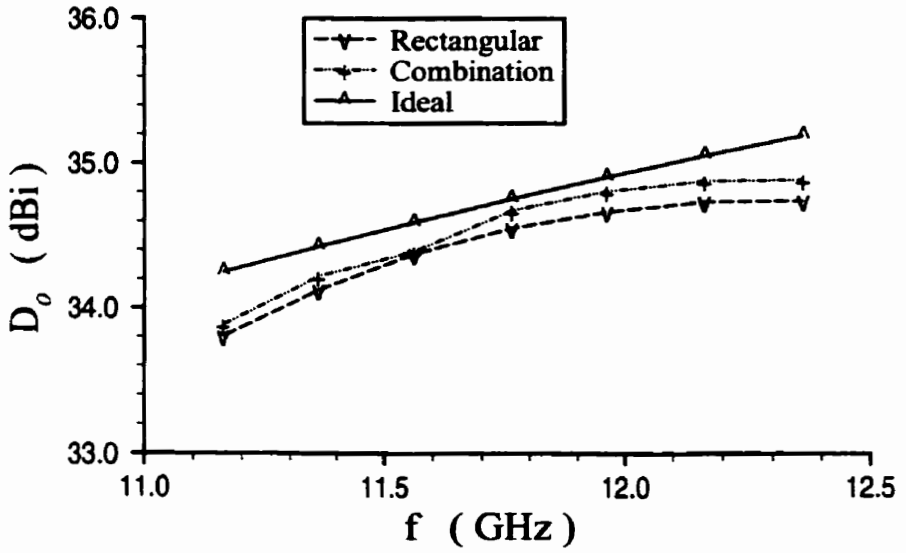

(b)

Fig. 5-12: Comparisons of reflectarray directivities D_o over a *10.2%* frequency bandwidth: (a) between the center-fed configuration of Fig. 3-8(a) and the offset-fed configuration of Fig. 5-11(a), and (b) between rectangular, combination and ideal patch arrays for offset-fed configurations with double line-source feeds and the same reflectarray parameters as in Fig. 5-11. The patch arrays are consist of 41×31 elements, and the ideal patch array has no phase correction error.

tion patch array increases more rapidly with frequency, as compared to the rectangular patch array. These behaviors are evident in Table 5-4.

From Table 3-4, Table 5-4 and Fig. 5-12, to within a *3.4%* bandwidth around the center frequency $f_o = 11.761$GHz , the rectangular patch array for the offset-fed configuration yields lower D_o, as compared to that of the thin substrate center-fed configuration of Chapter 3. This is because, due to its large F/D ratio, the spillover loss of the offset-fed configuration is larger than that of the center-fed configuration, in spite of its more directive double line-source feed.

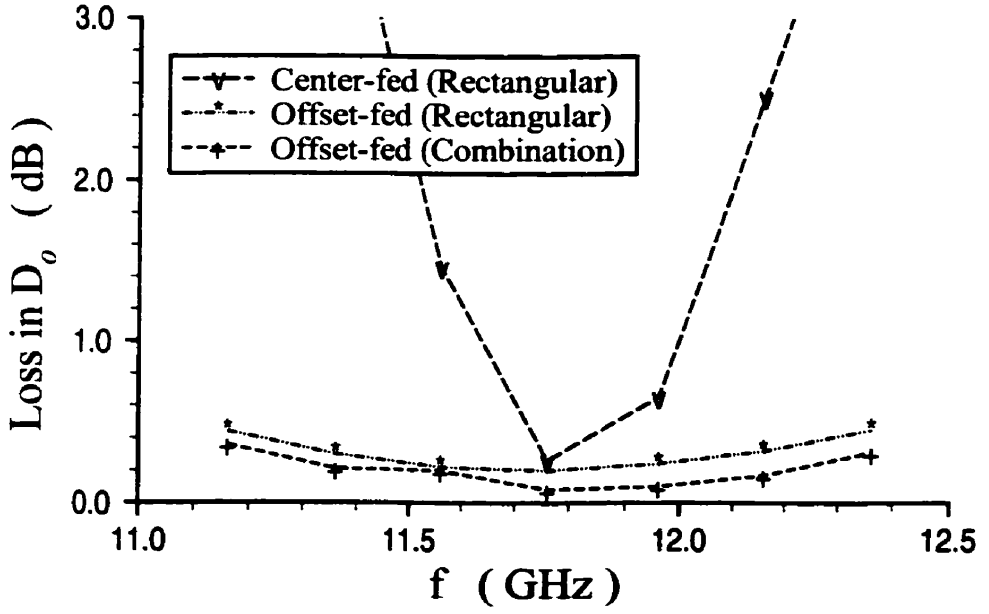

Fig. 5-13: Comparisons of reflectarray losses in directivity due to phase correction errors, over a *10.2%* frequency bandwidth, between the center-fed configuration of Fig. 3-8(a) and the offset-fed configurations of Fig. 5-11(a) and (b).

However, for a larger bandwidth of *10.2%*, the offset-fed configuration generates relatively stable radiation characteristics over the bandwidth, because of its thick substrate and large F/D ratio which decrease the reflectarray phase sensitivity. Variation in D_o is therefore smaller, and its SLL is also lower.

Table 5-4 also indicates that the beam squint effect on the main-lobe is constrained to within $\pm 0.3°$ from the intended design specification of $\theta_o = 25^o$, over the *10.2%* bandwidth, agreeing well with [39][40]. Hence, a relatively stable pencil-beam is generated from the reflectarray over the bandwidth.

5.3 COSINE-PEDESTAL LINE-SOURCE DISTRIBUTION

Instead of a uniform distribution for the double line-source feed, the cosine-pedestal distribution with pedestal $= -9$dB, discussed in Chapter 4, is implemented for this reflectarray. The primary purpose for using a tapered line-source distribution here is to further improve the reflectarray spillover loss, as demonstrated in Fig. 5-14.

The cosine-pedestal distribution with pedestal $= -9$dB is selected over other tapered distributions of Chapter 4, due to its smaller near-field oscillations which permits better phase corrections for a patch array that varies only in the y-direction. Furthermore, the cosine-pedestal distribution is also simpler to compute.

For the tapered line-source distribution reflectarray, the near-field due to the double line-source feed is more concentrated towards the center of the patch array because of the double line-source feed and its tapered distribution. Hence, as compared to that of the uniform distribution feeds, the spillover loss of the tapered distribution double line-source feed is less affected by the frequency scan over the *10.2%* bandwidth, for the given constant feed size, as shown in Fig. 5-14.

As expected, reflectarray SLL in the θ_o-plane, containing the main-lobe for $\theta_o = 25^o$ (graphically defined in Fig. 5-15(a)), are improved, and HPBW is also increased, as illus-

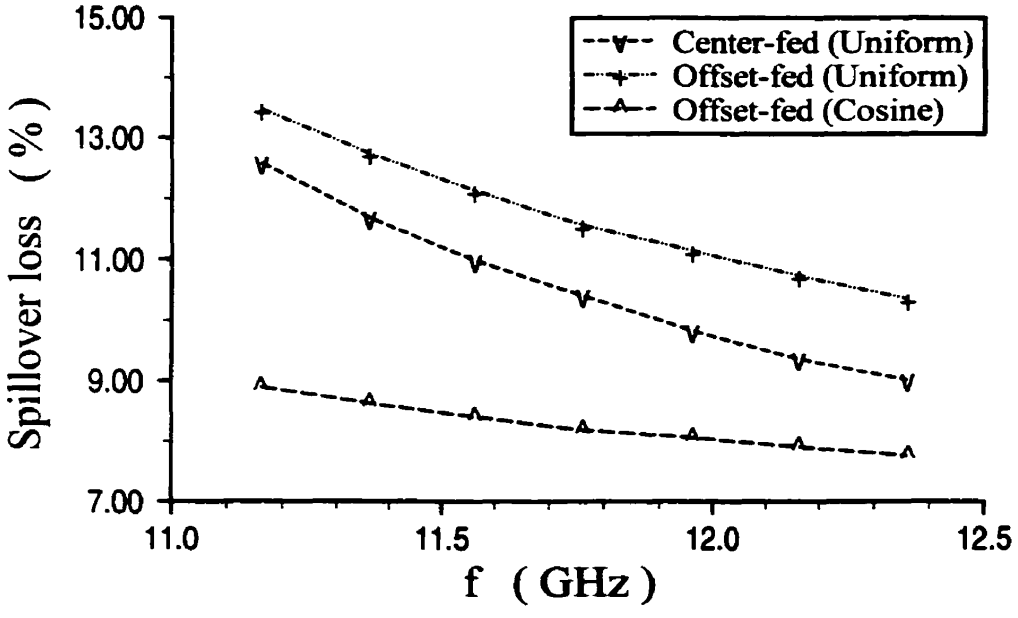

Fig. 5-14: Comparisons of reflectarray spillover losses, over a *10.2%* frequency bandwidth, between the center-fed configuration of Fig. 3-8(a) and the offset-fed configuration of Fig. 5-11(a), illuminated using uniform and cosine-pedestal line-source distributions described in Section 4.6. For the cosine-pedestal distribution, pedestal = -9dB.

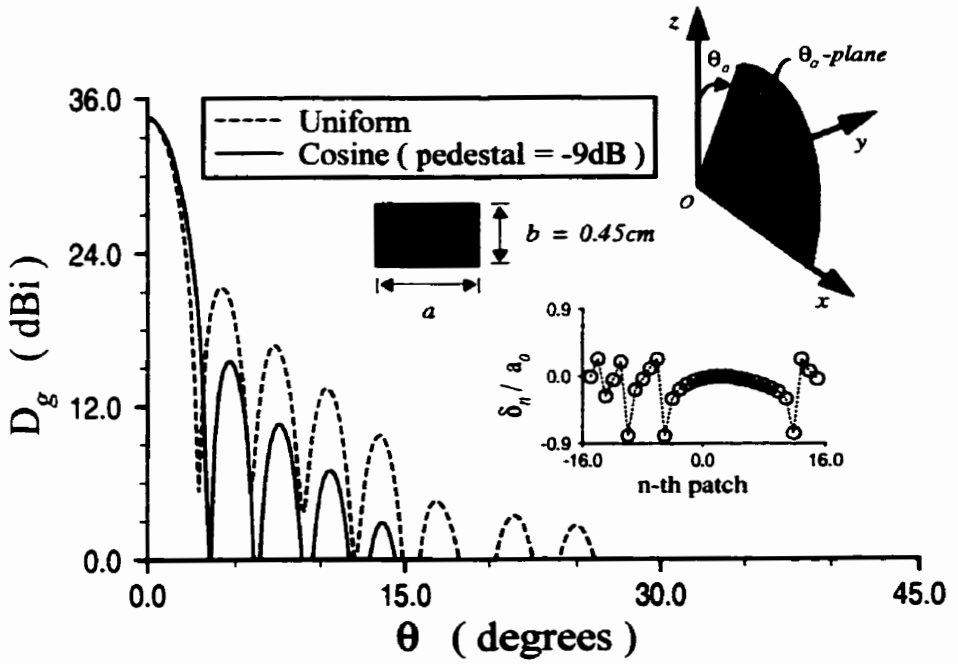

(a)

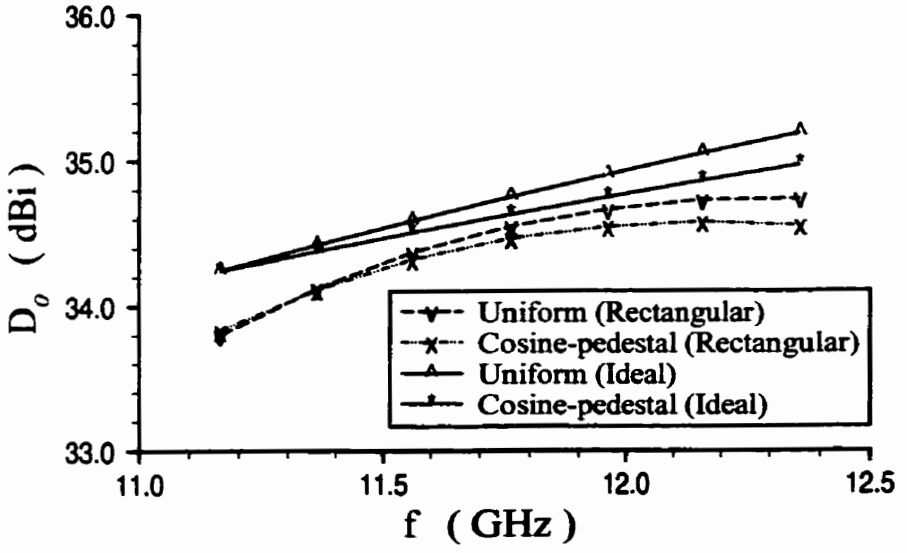

(b)

Fig. 5-15: Reflectarray far-field radiation characteristics for the offset-fed configuration of Fig. 5-11(a), illuminated using uniform and cosine-pedestal line-source distributions described in Section 4.6: (a) directive gain D_g patterns in the θ_o-plane, and (b) directivities D_o over a *10.2%* frequency bandwidth. Pedestal = *−9*dB for the cosine-pedestal distribution, and the ideal patch array has no phase correction error.

trated in Fig. 5-15(a). Consequently, its D_o is generally lower over the *10.2%* bandwidth, and its ideal counterpart is less sensitive to frequency (has a smaller gradient), as depicted in Fig. 5-15 (b). These characteristics are also presented in Table 5-5.

Table 5-5: Properties of an offset-fed microstrip reflectarray with a double line-source feed and a 41×31 -element rectangular patch array, and illuminated by a cosine-pedestal (with pedestal = -9dB) line-source distribution over a *10.2%* frequency bandwidth. $\varepsilon_r = 1.03$, $z_a = 0.3170$cm, $z_f = 26.279$cm, $\theta_o = 25^o$, $a_o = 0.974$cm $b = 0.45$cm and $d_y = 0.4979\lambda$, where λ is the wavelength. Values in brackets represent those for the uniform distribution.

Properties	Frequency, f (GHz)				
	11.161	*11.561*	*11.761*	*11.961*	*12.361*
D_o (dBi)	*33.83*	*34.33*	*34.47*	*34.55*	*34.56*
θ_o	25.17^o	25.03^o	24.97^o	24.91^o	24.79^o
HPBW (θ_o-plane)	3.01^o [2.63^o]	2.96^o [2.63^o]	2.94^o [2.60^o]	2.92^o [2.58^o]	2.87^o [2.52^o]
Max. SLL (θ_o-plane) (dB)	*−18.32* [*−13.11*]	*−18.71* [*−13.14*]	*−18.93* [*−13.21*]	*−19.18* [*−13.30*]	*−19.57* [*−13.41*]
Loss in directivity (dB)	*0.41*	*0.18*	*0.17*	*0.20*	*0.42*
Patch array length along the x-direction, $41s_x$ (λ)	*19.067*	*19.750*	*20.092*	*20.433*	*21.117*
Patch array length along the y-direction, $31s_y$ (λ)	*14.933*	*14.675*	*15.191*	*15.450*	*15.708*
Spillover (percent)	*8.90* [*13.47*]	*8.41* [*12.13*]	*8.19* [*11.56*]	*8.06* [*11.14*]	*7.76* [*10.36*]

5.4 CONCLUSION

For the offset-fed configuration, due to reduced phase correction errors, an off-broadside main beam provides improved phase corrections over that of a broadside main beam, with the feed blockage neglected. To minimize the phase correction errors for an off-broadside beam, the main beam angle θ_o is selected to equal the angle θ_{r_o} of the specular reflection in the yz-plane, at the center of the microstrip patch array. This also minimizes the beam squint effect due to frequency scanning.

For the infinite periodic array modelling, patch length errors from the empirical formulations of Chapter 4 for the patch array are proven to be minimal. Hence, these formulations are employed to obtain a quick first-pass solution, prior to executing the more rigorous infinite periodic array full wave analysis.

To significantly decrease the reflectarray spillover loss, a double line-source feed is implemented, which also results in improved reflectarray directivity and SLL in the H-plane ($\phi = \pm 90^o$). With this feed, a thick substrate offset-fed configuration is utilized as a design example, in addition to the thin substrate center-fed configuration of Chapter 3. Their far-field radiation characteristics are compared to those of ideal patch array counterparts. Also, the array geometrical symmetry is utilized for enhancing computation speed and efficiency of their far-field radiation calculations.

The thin substrate center-fed configuration yields good narrowband radiation characteristics, while the thick substrate offset-fed configuration is excellent for wideband applications. When implemented with the combination microstrip patch array consisting of rectangular, strip and hat-shaped patches, the offset-fed configuration demonstrates improvements in reflectarray far-field radiation characteristics over the microstrip rectangular patch array. That is, it suffers less directivity loss due to phase correction errors, and yields lower SLL in the H-plane ($\phi = \pm 90^{o}$). Thus, the hat-shaped patch geometry offers excellent promises for improving the reflectarray far-field radiation performance.

The cosine-pedestal line-source distribution, with pedestal $= -9$dB, for the reflectarray feed is used to further improve its spillover loss. Compared to the uniform line-source distribution, in both center-fed and offset-fed configurations, the cosine-pedestal distribution yields the lowest reflectarray spillover loss, but generally, at the cost of decreased reflectarray directivity. It also produces reduced SLL in the θ_o-plane.

6 Summary and Future Research

The infinite periodic array modelling was employed for the analysis of line-source-fed single-layer microstrip reflectarrays. A software package, consisting of *ARCOF* and *EFEL* codes, were developed for this study. Utilizing this software package, the effects of patch geometries and substrate permittivity and thickness on the performance of microstrip reflectarrays were investigated. Two feed configurations and some design concepts were also studied.

6.1 SUMMARY

Research contributions from this thesis are summarized as follow:

- A rigorous analysis of the unattainable phase range, inherent to infinite periodic arrays of single-layer rectangular microstrip patches, was performed. Subsequently, a combination microstrip patch array consisting of rectangular/strip and hat-shaped patches was proposed to rectify this problem.
- The hat-shaped microstrip patch is a novel geometry in microstrip reflectarray designs, and its reflection phase properties were investigated and discussed in detail. It offers

promising future in microstrip reflectarray applications because of its complementary reflection phase properties.

- Numerically efficient empirical formulations for the TE-to-z reflection coefficient phase was proposed. This is an important tool in the analysis of the reflectarray since it requires negligible computation time and memory.
- A rigorous phase error analysis for line-source-fed single-layer microstrip reflectarrays was performed, addressing the phase errors.
- The formulation for reflectarray far-field radiation, due to a line-source feed, was developed using the infinite periodic array and aperture field theories.
- A rigorous phase analysis of the offset-fed configuration was performed, and a condition for minimum phase correction error was proposed, which is also the condition for minimum beam squint effect.
- The far-field radiation characteristics of line-source-fed single-layer microstrip reflectarrays, for both center-fed and offset-fed configurations, were rigorously analyzed and discussed.
- Tapered line-source distributions were investigated for reducing reflectarray spillover loss and SLL in the E-plane ($\phi = 0^o$) of the center-fed configuration, or the θ_o-plane of the offset-fed configuration.
- A software package, consisting of *ARCOF* and *EFEL* codes, was created for the analysis of line-source-fed single-layer microstrip reflectarrays.

6.2 FUTURE RESEARCH

Some recommendations for further research are:

- An implementation to refine the infinite periodic array modelling in terms of computational speed and efficiency, using improved numerical techniques in [57][58][63]-[71].
- A replacement of the co-linear dipole array feed with other antennas, such as a co-linear microstrip patch or slot array.
- An investigation into the feasibility of employing other patch geometries as array elements, or other array lattice geometries, to enhance the reflectarray bandwidth performance, and to enable circularly-polarized or dual-band operation, as presented in [11][29] [31]-[34] [73][103][104].
- An extension of analysis to include multilayer arrays, so as to enhance the reflectarray bandwidth performance and to enable dual-band operation [34][73].
- An implementation of the triangular basis function expansion to model arbitrary geometries [2][53].
- A development of electronic beam-scanning antennas using line-source-fed microstrip reflectarrays.

A Equation Parameter Definitions

A.1 Parameters Relevant to Integral Equation (2-10) of Chapter 2

Notations used in the derivation of the integral equation (2-10) are:

$\vec{J}_s(\vec{r}_T)$ = unknown current density on patch element ($r_T \in A'$)

A' = area of patch element (thin perfectly conducting patch element of arbitrary shape)

s_x, s_y = dimensions of rectangular cell along x- and y- directions, respectively

A = area of rectangular cell, $s_x s_y$

(θ_l, ϕ_l) = spherical coordinates in medium l

$l = 1, 2, 3$ = index for layered media

$m = 1, 2$ = index for transverse field modes (TM and TE modes, respectively)

$p, q = 0, \pm 1, \pm 2, \ldots$ = indices for Floquet modes along x- and y- directions, respectively

Coordinate vector of the point of observation is:

$$\vec{\rho}_T = x\,\hat{x} + y\,\hat{y} \tag{A-1}$$

Transverse Floquet modal propagation unit vectors are:

$$\hat{\kappa}_{lpq}^{(l)} = \hat{\kappa}_{lpq_x}^{(l)} + \hat{\kappa}_{lpq_y}^{(l)} = \frac{k_{Tpq_x}^{(l)}\hat{x} + k_{Tpq_y}^{(l)}\hat{y}}{k_{Tpq}^{(l)}} \;; \qquad \text{For TM incident plane wave} \tag{A-2}$$

$$\hat{\kappa}_{2pq}^{(l)} = \hat{\kappa}_{2pq_x}^{(l)} + \hat{\kappa}_{2pq_y}^{(l)} = \frac{k_{Tpq_y}^{(l)}\hat{x} - k_{Tpq_x}^{(l)}\hat{y}}{k_{Tpq}^{(l)}} \;; \qquad \text{For TE incident plane wave} \tag{A-3}$$

where

$$\vec{k}_{Tpq}^{(l)} = \vec{k}_{Tpq_x}^{(l)} + \vec{k}_{Tpq_y}^{(l)} = \vec{k}_T^{(l)} \mp p\frac{2\pi}{s_x}\hat{x} \mp q\frac{2\pi}{s_y}\hat{y} \tag{A-4}$$

$$\vec{k}_T^{(l)} = k^{(l)}\vec{T}^{(l)} \tag{A-5}$$

$$\vec{T}^{(l)} = \vec{T}_x^{(l)} + \vec{T}_y^{(l)} = \sin\theta_l\,(\cos\phi\,\hat{x} + \sin\phi\,\hat{y}) \;; \qquad \sin\theta_l \neq 0 \tag{A-6}$$

$$k^{(l)} = \omega\sqrt{\mu_l\varepsilon_l} \tag{A-7}$$

Floquet modal propagation constant is:

$$\Gamma_{pq}^{(l)} = \begin{cases} \left|\Gamma_{pq}^{(l)}\right| , & k^{(l)2} \geq \hat{k}_{T_{pq}}^{(l)} \cdot \hat{k}_{T_{pq}}^{(l)} \; ; \quad \text{For propagating Floquet modes} \\ -j\left|\Gamma_{pq}^{(l)}\right| , & k^{(l)2} < \hat{k}_{T_{pq}}^{(l)} \cdot \hat{k}_{T_{pq}}^{(l)} \; ; \quad \text{For evanescent Floquet modes} \end{cases} \tag{A-8}$$

where

$$\left|\Gamma_{pq}^{(l)}\right| = \sqrt{\left|k^{(l)2} - \hat{k}_{T_{pq}}^{(l)} \cdot \hat{k}_{T_{pq}}^{(l)}\right|} = \sqrt{\left|k^{(l)2} - k_{T_{pq_x}}^{(l)2} - k_{T_{pq_y}}^{(l)2}\right|} \tag{A-9}$$

Floquet modal admittances are:

$$\zeta_{1pq}^{(l)} = \frac{k^{(l)}}{\eta^{(l)}\Gamma_{pq}^{(l)}} \; ; \quad \text{For TM incident plane wave} \tag{A-10}$$

$$\zeta_{2pq}^{(l)} = \frac{\Gamma_{pq}^{(l)}}{\eta^{(l)}k^{(l)}} \; ; \quad \text{For TE incident plane wave} \tag{A-11}$$

where

$$\eta^{(l)} = \sqrt{\frac{\mu_l}{\varepsilon_l}} \tag{A-12}$$

$$k^{(l)} = \omega\sqrt{\mu_l\varepsilon_l} \tag{A-13}$$

Floquet modal reflection coefficients are:

$$R_{mpq}^{(2)} = \frac{\zeta_{mpq}^{(1)} - \zeta_{mpq}^{(2)}\left(\frac{1 - R_{mpq}^{(3)}}{1 + R_{mpq}^{(3)}}\right)}{\zeta_{mpq}^{(1)} + \zeta_{mpq}^{(2)}\left(\frac{1 - R_{mpq}^{(3)}}{1 + R_{mpq}^{(3)}}\right)} \quad ; \text{ For reflection due to dielectric sheet} \qquad \text{(A-14)}$$

$$R_{mpq}^{(3)} = \left(\frac{\zeta_{mpq}^{(2)} - \zeta_{mpq}^{(3)}}{\zeta_{mpq}^{(2)} + \zeta_{mpq}^{(3)}}\right) e^{-j2\Gamma_{pq}^{(2)} z_a} \quad ; \text{ For reflection due to boundary at } z = -z_a \qquad \text{(A-15)}$$

Equivalent Floquet modal admittance is:

$$\zeta_{mpq}^{(eq)} = \zeta_{mpq}^{(1)} + \left(\frac{1 - R_{mpq}^{(3)}}{1 + R_{mpq}^{(3)}}\right)\zeta_{mpq}^{(2)} \qquad \text{(A-16)}$$

A.2 Parameters for Entire-Domain Basis Function Expansion of Chapter 2, Equations (2-12)-(2-14)

Notations relevant to current modal expansion equations (2-12)-(2-14) are:

$c_{m'n'}$ = unknown current modal coefficient

$\hat{h}_{m'n'}(\hat{r}_T)$ = modal basis vector

$m' = 1, 2$ = index for transverse field modes (TM and TE modes, respectively)

n' = index for modal basis vectors, to be mapped as $n' \rightarrow (n_1, n_2)$

a, b = dimensions of rectangular patch element along x- and y- directions, respectively

$n, n_1, n_2 = 0, 1, 2, \ldots$; $n_1 \neq n_2$ when $n_2 = 0$

Entire-domain sinusoidal basis functions [49] are:

$$h_{n_1 n_2 x}(x, y) = \sin\left[n_1\pi\left(\frac{x}{a}-\frac{1}{2}\right)\right]\cos\left[n_2\pi\left(\frac{y}{b}-\frac{1}{2}\right)\right] ; \text{ in the x-direction} \qquad \text{(A-17)}$$

$$h_{n_1 n_2 y}(x, y) = \cos\left[n_1\pi\left(\frac{x}{a}-\frac{1}{2}\right)\right]\sin\left[n_2\pi\left(\frac{y}{b}-\frac{1}{2}\right)\right] ; \text{ in the y-direction} \qquad \text{(A-18)}$$

Normalization factor for entire-domain basis vectors (2-14) [49] is:

$$F_{n_1 n_2} = \sqrt{\frac{\left[\frac{\varepsilon_{n_1}\varepsilon_{n_2}}{ab}\right]}{\left[\left(\frac{n_1\pi}{a}\right)^2+\left(\frac{n_2\pi}{b}\right)^2\right]}} , \qquad \text{(A-19)}$$

where

$$\varepsilon_n = \begin{cases} 1 ; & n = 0 \\ 2 ; & n \geq 1 \end{cases} \qquad \text{(A-20)}$$

A.3 PARAMETERS FOR SUBDOMAIN BASIS FUNCTION EXPANSION OF CHAPTER 2, EQUATIONS (2-16)-(2-17)

Notations relevant to current modal expansion equations (2-16)-(2-17) are:

$c_{n'_x}$, $c_{n'_y}$ = unknown current modal coefficients for x- and y- directions, respectively

$\hat{h}_{n'_x}(\hat{r}_T)$, $\hat{h}_{n'_y}(\hat{r}_T)$ = modal basis vectors in the x- and y- directions, respectively

n'_x , n'_y = indices for modal basis vectors for x- and y- directions, respectively, to be mapped as $n'_x \rightarrow (n_1, n_2, x)$ and $n'_y \rightarrow (n_1, n_2, y)$, respectively

$n, n_1, n_2 = 0, \pm 1, \pm 2, \ldots$

Similarly, subdomain roof-top basis functions [51] are:

$$h_{n_1 n_2 x}(x, y) = \Lambda_{n_1 + 1/2}(x)\Pi_{n_2}(y); \quad \text{in the x-direction} \tag{A-21}$$

$$h_{n_1 n_2 y}(x, y) = \Pi_{n_1}(x)\Lambda_{n_2 + 1/2}(y); \quad \text{in the y-direction} \tag{A-22}$$

where

$$\Lambda_n(x) = \begin{cases} 1 - \dfrac{|x - n\Delta x|}{\Delta x} & ; \ |x - n\Delta x| \le \Delta x \\ 0 & ; \ \text{elsewhere} \end{cases} \tag{A-23}$$

$$\Pi_n(x) = \begin{cases} 1 & ; \ |x - n\Delta x| \le \dfrac{\Delta x}{2} \\ 0 & ; \ \text{elsewhere} \end{cases} \tag{A-24}$$

B Simulation Software

A major effort has been primarily concentrated on developing a computer modelling software package for the analysis and design of line-source-fed single-layer microstrip reflectarrays. The software code is programmed in C language using the ANSI C standard, and may be executed using Perl script.

Algorithms for patch segmentation schemes, types of basis functions employed and solution technique are based on formulations presented in this thesis. The software code is constructed using register pointers and dynamic memory allocation functions, for faster and more efficient code execution. Its program structure is also highly modularized for future code upgrades and maintenance.

B.1 Simulation Software for Line-Source-Fed Microstrip Reflectarrays

This section presents a brief description of some important aspects of this software package. A complete graphical description of this software is provided in Fig. B-1, for a line-source-fed microstrip reflectarray with an $M \times N$-element patch array.

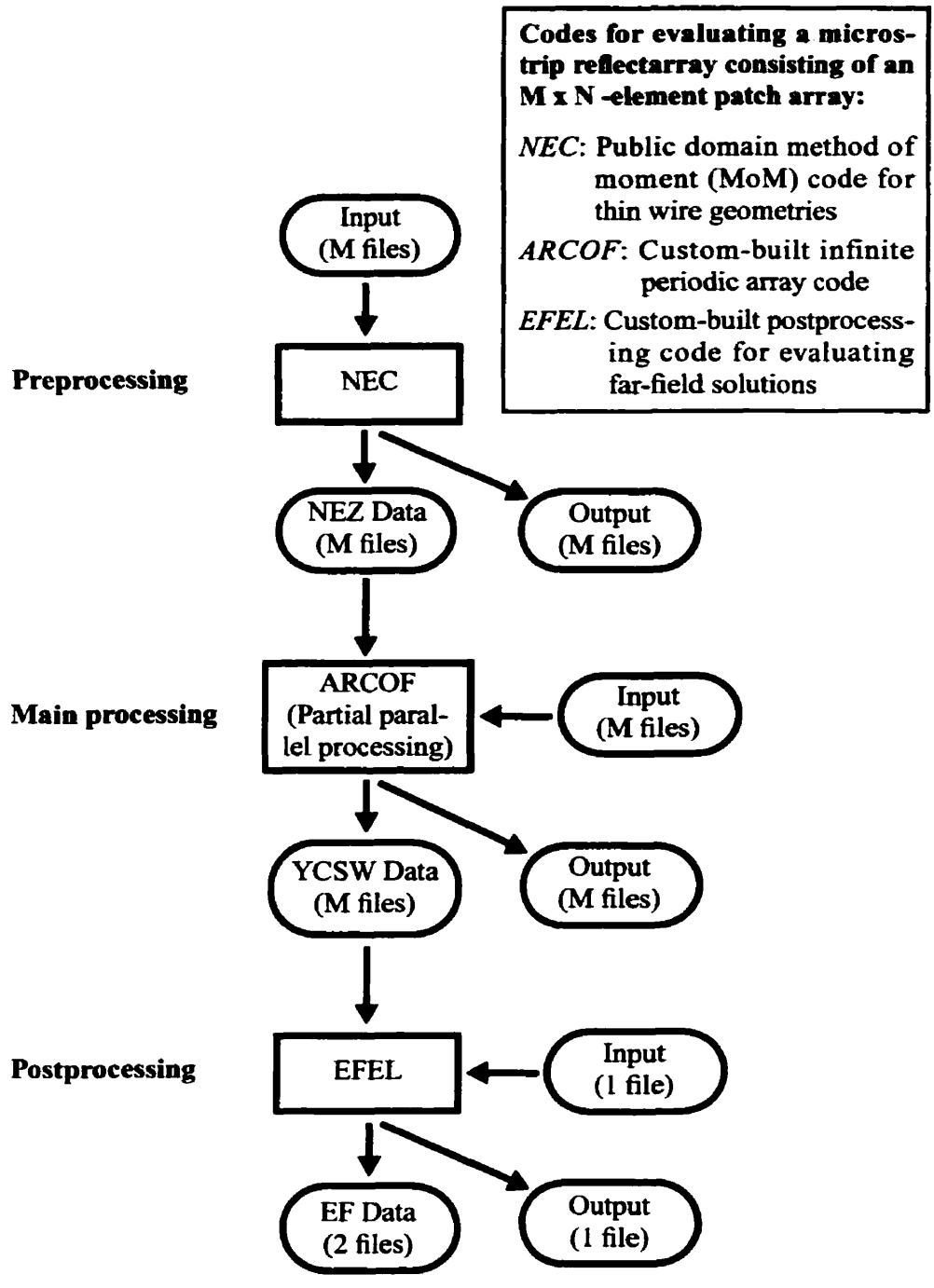

Fig. B-1: General simulation outline for a line-source-fed single-layer microstrip reflectarray consisting of an $M \times N$-element patch array, i.e. with M dissimilar columns and N dissimilar rows. *"NEZ Data"* is the line-source near-field data, *"YCSW Data"* is the reflection coefficient and patch length data for an array column, and *"EF Data"* is the reflectarray far-field radiation data. Input and output files contain input and other output information, respectively.

B.1.1 *NEC*: The Preprocessing Module

The preprocessing code, *NEC*, is a Method of Moment (MoM) code for thin wire geometries, and is a well-known public domain software. It is employed for computing the near-fields, due to a line-source consisting of a co-linear of half-wavelength dipoles that is backed by a finite ground plane, at patch locations on the microstrip patch array. These near-field data are written into the *"NEZ Data"* files, to be read by the *ARCOF* code.

B.1.2 *ARCOF*: The Main Processing Module

The main processing code, *ARCOF*, models a single-layer patch array using the infinite periodic array technique. This code is implemented for single-layer array analysis, with or without an infinite ground plane, and can be executed in two modes, i.e. infinite periodic array mode, or line-source-fed reflectarray mode. Also, either the entire-domain or sub-domain basis function expansion can be selected for use in the analysis.

In the infinite periodic array mode, *ARCOF* computes the array reflection coefficient due to either frequency, incident angle, substrate thickness or permittivity, basis function or Floquet mode truncation, patch or cell dimension, depending on the choice selected in the input file. This file contains patch array and incident angle specifications, basis function and Floquet mode truncation parameters, a choice of basis function expansion, and operation frequency.

However, in the line-source-fed reflectarray mode, the code computes reflection coefficients of patch elements along a specified column of the patch array. M input files, each representing a column of an $M \times N$-element patch array, are necessary. These input files contain parameters specifying the array columns and rows to be evaluated, in addition to the input information similar to the infinite periodic array mode.

Subsequently, M *"YCSW Data"* files are generated, containing reflection coefficient data, together with M output files containing other output information, such as, type of process run, matrix size utilized, CPU time and completion messages. The *"YCSW Data"* files are to be read by the *EFEL* code in postprocessing.

Since *ARCOF* is implemented using C language and Perl script, partial parallel processing, in combination with the traditional sequential processing, is viable for decreasing the total computation time required. This is analogous to the Single Program Multiple Data (SPMD) concept [105], but, it requires further modifications for a full SPMD implementation.

B.1.3 *EFEL*: The Postprocessing Module

The postprocessing code, *EFEL*, evaluates the reflectarray far-field radiation characteristics, such as, directive gain pattern, directivity, loss in directivity and spillover loss, based on values from the *"YCSW Data"* files generated by *ARCOF*. The code also evaluates the

same far-field radiation characteristics for the corresponding ideal patch array for no phase error.

The input file specifies frequency, observation angles for directive gain pattern, total power radiated from feed (as computed from *NEC*), main beam angle, array columns and rows to be evaluated, and array element separations. *2* *"EF Data"* files, containing directive gain patterns for the patch array and its ideal array counterpart, and an output file containing reflectarray far-field radiation characteristics, are subsequently generated.

B.2 HARDWARE REQUIREMENT AND CPU TIME

An example of a typical computational performance for a single run of an offset-fed microstrip reflectarray, having a 41×31-element patch array (i.e. with *41* dissimilar columns and *31* dissimilar rows), as performed on a typical Sun Ultra 10 workstation with *512*MB RAM and Solaris 2.7 OS is given as:

- For *ARCOF* (using sequential processing only):

  CPU time = *63.0*hours, memory = *12.0*MB and

  minimum hard disk space requirement = *8.7*MB.

- *EFEL*:

  CPU time = *19.3*hours, memory < *1.4*MB and

  minimum hard disk space requirement = *0.7*MB.

In this simulation example, there are *41* input files, *41* output files and *41* *"YCSW Data"* files for *ARCOF*, and *1* input file, *1* output file and *2* *"EF Data"* files for *EFEL*. The number of files, CPU time and memory requirements would be larger for a larger patch array simulation.

References

[1] Vishwani D. Agrawal and William A. Imbriale; "Design of a dichroic Cassegrain subreflector"; *IEEE Trans. Antennas and Propag.*, vol. AP-27, no. 4; July 1979; pp. 466-473.

[2] Raj Mittra, Chi H. Chan and Tom Cwik; "Techniques for analyzing frequency selective surfaces -- a review"; *Proc. IEEE*, vol. 76, no. 12; December 1988; pp. 1593-1615.

[3] J. Harvey, E. R. Brown, D. B. Rutledge and R. A. York; "Spatial power combining for high-power transmitters"; *IEEE Microwave Mag.*, vol. 1, no. 4; December 2000; pp. 48-59.

[4] Olof Dahlsjo; "Antenna research and development at Ericsson"; *IEEE Antennas and Propag. Mag.*, vol. 34, no. 2; April 1992; pp. 7-17.

[5] R. Orta, P. Savi and R. Tascone; "Multiple frequency-selective surfaces consisting of ring patches", *Electromagnetics*, vol. 15; 1995; pp. 417-426.

[6] D. G. Berry, R. G. Malech and W. A. Kennedy; "The reflectarray antenna"; *IEEE Trans. Antennas and Propag.*, vol. AP-11, no. 6; November 1963; pp. 645-651.

[7] David M. Pozar, Stephen D. Targonski and H. D. Syrigos; "Design of millimeter wave microstrip reflectarrays"; *IEEE Trans. on Antennas and Propag.*, vol. 45, no. 2; February 1997; pp. 287- 296.

[8] D.-C. Chang and M.-C. Huang; "Microstrip reflectarray antenna with offset feed", *Electronics Lett.*, vol. 28, no. 16; July 1992; pp. 1489-1491.

[9] Dau-Chyrh Chang and Ming-Chih Huang; "Multiple-polarization microstrip reflectarray antenna with high efficiency and low cross-polarization"; *IEEE Trans. on Antennas and Propag.*, vol. 43, no. 8; August 1995; pp. 829- 834.

[10] John Huang; "Analysis of a microstrip reflectarray antenna for microspacecraft applications", *JPL TDA Progress Report No. 42-120*; Jet Propulsion Laboratory, Pasadena, California; February 15, 1995; pp. 153-173.

[11] John Huang and Ronald J. Pogorzelski; "A Ka-band microstrip reflectarray with elements having variable rotation angles"; *IEEE Trans. Antennas and Propag.*, vol. 46, no. 5; May 1998; pp. 650-656.

[12] F. Stefan Johansson, Lars G. Josefsson and Torlid Lorentzon; "A novel frequency-scanned reflector antenna"; *IEEE Trans. Antennas and Propag.*, vol. 37, no. 8; August 1989; pp. 984-989

[13] F. Stefan Johansson; "A new planar grating-reflector antenna"; *IEEE Trans. Antennas and Propag.*, vol. 38, no. 9; September 1990; pp. 1491-1495.

[14] F. Stefan Johansson; "Frequency-scanned reflection gratings consisting of ring patches"; *IEE Proc. Pt. H*, vol. 138, no.4; August 1991; pp. 273-276.

[15] F. Stefan Johansson; "Frequency-scanning grating-reflector antenna for multibeam satellite communications"; *IEEE Trans. Antennas and Propag.*, vol. 40, no. 10; October 1992; pp. 1231-1237.

[16] Jafar Shaker and Michel Cuhaci; "A novel technique for beam squint cancellation in planar reflectors"; *1998 Symp. on Antenna Technology and Applied Electromagnetics (ANTEM '98)*, Montreal, Canada; August 1998; pp. 559-562.

[17] Y. Jay Guo and Stephen K. Barton; "Phase correcting zonal reflector incorporating rings"; *IEEE Trans. Antennas and Propag.*, vol. 43, no. 4; April 1995; pp. 350-355.

[18] C. S. Malagisi; "Microstrip disc element reflectarray"; *Electronics and Aerospace Systems Convention*; September 1978.

[19] Robert E. Munson, Hussain A. Haddad and John W. Hanlen; "Microstrip reflectarray for satellite communication and radar cross-section enhancement or reduction", *U. S. Patent No. 4684952*; U. S. Patent and Trademark Office, Washington, D. C.; August 4, 1987.

[20] H. R. Phelan; "Spiraphase reflectarray for multitarget radar"; *Microwave J.*, vol. 20; July 1977; pp. 67-73.

[21] Thomas Allan Metzler; "Design and analysis of a microstrip reflectarray"; *Ph. D. Thesis*; University of Massachusetts at Amherst, Massachusetts; February 1993.

[22] John Huang; "Microstrip reflectarray", *1991 IEEE Antennas and Propag. Society International Symp.*, vol. 2, London, Canada; June 1991; pp. 612-615.

[23] Yuan Zhuang, Ke-Li Wu, Chen Wu and John Litva; "Microstrip reflectarrays: Full-wave analysis and design scheme", *1993 IEEE Antennas and Propag. Society International Symp.*, vol. 3, Ann Arbor, MI; June 1993; pp. 1386-1389.

[24] Y. Zhuang, J. Litva, C. Wu and K.-L. Wu; "Modelling studies of microstrip reflectarrays"; *IEE Proc. Microwaves, Antennas and Propag.*, vol. 142, no. 1; February 1995; pp. 78-80.

[25] Ronald D. Javor, Xiao-Dong Wu and Kai Chang; "Design and performance of a microstrip reflectarray antenna"; *IEEE Trans. Antennas and Propag.*, vol. 43, no. 9; September 1995; pp. 932-939.

[26] Anand Kelkar; "FLAPS: Conformal phased reflecting surfaces"; *1991 IEEE National Radar Conf.*, Los Angeles, California; March 1991; pp. 58-62.

[27] D. M. Pozar and T. A. Metzler; "Analysis of a reflectarray antenna using microstrip patches of variable size", *Electronics Lett.*, vol. 29, no. 8; April 1993; pp. 657-658.

[28] S. D. Targonski and D. M. Pozar; "Analysis and design of a microstrip reflectarray using patches of variable size"; *1994 IEEE Antennas and Propag. Society International Symp.*, vol. 3, Seattle, WA; June 1994; pp. 1820-1823.

[29] David M. Pozar and Stephen D. Targonski; "A microstrip reflectarray using crossed dipoles"; *1998 IEEE Antennas and Propag. Society International Symp.*, vol. 2, Atlanta, GA; June 1998; pp. 1008-1011.

[30] M. E. Cooley, J. F. Walker, D. G. Gonzalez and G. E. Pollon; "Novel reflectarray element with variable phase characteristics"; *IEE Proc. Microwaves, Antennas and Propag.*, vol. 144, no. 2; April 1997; pp. 149-151.

[31] John Huang; "A high-gain circularly polarized Ka-band microstrip reflect array", *Microwave and Optical Technology Lett.*, vol. 14, no. 3; February 1997; pp. 163-166.

[32] John Huang and Ronald J. Pogorzelski; "Microstrip reflectarray with elements having variable rotation angles", *1997 IEEE Antennas and Propag. Society International Symp.*, vol. 2, Montreal, Canada; June 1997; pp. 1280-1283.

[33] Doris I. Wu, Richard C. Hall and John Huang; "Dual-frequency microstrip reflectarray", *1995 IEEE Antennas and Propag. Society International Symp.*, vol. 4, Newport Beach, CA; June 1995; pp. 2128-2131.

[34] J. A. Encinar; "Design of a dual frequency reflectarray using microstrip stacked patches of variable size", *Electronics Lett.*, vol. 32, no. 12; June 1996; pp. 1049-1050.

[35] E. Baruch and Y. Leviatan; "Analysis of quasiperiodic reflector antenna"; *IEE Proc. Microwaves, Antennas and Propag.*, vol. 143, no. 4; August 1996; pp. 293-297.

[36] Dietmar Pilz and Wolfgang Menzel; "Full wave analysis of a planar reflector antenna"; *1997 Asia Pacific Microwave Conf. (APMC '97)*, vol. 1, Hong Kong, PRC.; December 1997; pp. 225-227.

[37] D. Pilz and W. Menzel; "Folded reflectarray antenna", *Electronics Lett.*, vol. 34, no. 9; April 1998; pp. 832-833.

[38] Wolfgang Menzel, Dietmar Pilz and Ralf Leberer; "A 77-GHz FM/CW radar front-end with a low-profile, low-loss printed antenna", *IEEE Trans. Microwave Theory and Techn.*, vol. 47, no. 12; December 1999; pp. 2237-2241.

[39] Stephen Donald Targonski; "Two selected topics involving theory and applications of infinite arrays of microstrip elements"; *Ph. D. Thesis*; University of Massachusetts at Amherst, Massachusetts; September 1995.

[40] S. D. Targonski and D. M. Pozar; "Minimization of beam squint in microstrip reflectarrays using an offset feed"; *1996 IEEE Antennas and Propag. Society International Symp.*, vol. 2; July 1996; pp. 1326-1329.

[41] John Huang; "Bandwidth study of microstrip reflectarray and a novel phased reflectarray concept", *1995 IEEE Antennas and Propag. Society International Symp.*, vol. 1; June 1995; pp. 582-585.

[42] John Huang; "Design aspects of the microstrip reflectarray"; *1998 Symp. on Antenna Technology and Applied Electromagnetics (ANTEM '98)*, Montreal, Canada; August 1998; pp. 555-558.

[43] N. Amitay, V. Galindo and C. P. Wu; *Theory and Analysis of Phased Array Antennas*; Wiley-Interscience, New York; 1972.

[44] R. C. McPhedran, G. H. Derrick and L. C. Botten; "Theory of crossed gratings"; *Electromagnetic Theory of Gratings*, ed. R. Petit; Springer-Verlag, Berlin; 1980; pp. 227-276.

[45] G. A. Morin; "A simple circular polarization selective surface (CPSS)"; *1990 IEEE Antennas and Propag. Society International Symp.*, vol. 1, Dallas, TX; 1990; pp. 100-101.

[46] Jasmin E. Roy; "Reciprocal circular polarization selective surfaces"; *Ph. D. Thesis*; University of Manitoba, Winnipeg, Manitoba; December 1995.

[47] J. E. Roy and L. Shafai; "Reciprocal circular-polarization-selective surface"; *IEEE Antennas and Propag. Mag.*, vol. 38, no. 6; December 1996; pp. 18-33.

[48] R. H. Ott, R. G. Kouyoumjian and L. Peters, Jr.; "Scattering by a two-dimensional periodic array of narrow plates"; *Radio Sci.*, vol. 2, no. 11; November 1967; pp. 1347-1359.

[49] Chao-Chun Chen; "Scattering by a two-dimensional periodic array of conducting plates"; *IEEE Trans. on Antennas and Propag.*, vol. AP-18, no. 5; September 1970; pp. 660-665.

[50] James P. Montgomery; "Scattering by an infinite periodic array of thin conductors on a dielectric sheet"; *IEEE Trans. on Antennas and Propag.*, vol. AP-23, no. 1; January 1975; pp. 70- 75.

[51] Barry J. Rubin and Henry L. Bertoni; "Reflection from a periodically perforated plane using a subsectional current approximation", *IEEE Trans. Antennas and Propag.*, vol. AP-31, no.6; November 1983; pp. 829-836.

[52] Chich-Hsing Tsao and Raj Mittra; "Spectral-domain analysis of frequency selective surfaces comprised of periodic arrays of cross dipoles and Jerusalem crosses"; *IEEE Trans. on Antennas and Propag.*, vol. AP-32, no. 5; May 1984; pp. 478-486.

[53] Thomas A. Cwik and Raj Mittra; "Scattering from a periodic array of free-standing arbitrarily shaped perfectly conducting or resistive patches"; *IEEE Trans. Antennas and Propag.*, vol. AP-35, no. 11; November 1987; pp. 1226-1234.

[54] Wai L. Ko and Raj Mittra; "Scattering by a truncated periodic array"; *IEEE Trans. Antennas and Propag.*, vol. 36, no. 4; April 1988; pp. 496-503.

[55] Jian-Ming Jin and John L. Volakis; "Electromagnetic scattering by a perfectly conducting patch array on a dielectric slab", *IEEE Trans. Antennas and Propag.*, vol. 38, no. 4; April 1990; pp. 556-563.

[56] J. Shaker and L. Shafai; "Reflection properties of conducting rectangular elements printed on a dielectric slab"; *Can. J. of Phys.*, vol. 72, no. 5-6, May-June 1994, pp. 299-310.

[57] Alp Kustepeli and Anthony Q. Martin; "On the splitting parameter in the Ewald method"; *IEEE Microwave and Guided Wave Lett.*, vol. 10, no. 5; May 2000; pp. 168-170.

[58] Yongxue Yu and Chi Hou Chan; "Efficient hybrid spatial and spectral techniques in analyzing planar periodic structures with nonuniform discretizations"; *IEEE Trans. Microwave Theory and Techn.*, vol. 48, no. 10; October 2000; pp. 1623-1627.

[59] Wen-Jiunn Tsay and David M. Pozar; "Application of the FDTD technique to periodic problems in scattering and radiation"; *IEEE Microwave and Guided Wave Lett.*, vol. 3, no. 8; August 1993; pp. 250-252.

[60] J. Ren, O. P. Gandhi, L. R. Walker, J. Fraschilla and C. R. Boerman; "Floquet-based FDTD analysis of two-dimensional phased array antennas"; *IEEE Microwave and Guided Wave Lett.*, vol. 4, no. 4; April 1994; pp. 109-111.

[61] Deane T. Prescott and N. V. Shuley; "Extensions to the FDTD method for the analysis of infinitely periodic arrays"; *IEEE Microwave and Guided Wave Lett.*, vol. 4, no. 10; October 1994; pp. 352-354.

[62] A. Alexanian, N. J. Kolias, R. C. Compton and R. A. York; "Three-dimensional FDTD analysis of quasi-optical arrays using Floquet boundary conditions and Berenger's PML"; *IEEE Microwave and Guided Wave Letters*, vol. 6, no. 3; March 1996; pp. 138-140.

[63] Eric W. Lucas and Thomas P. Fontana; "A 3-D hybrid finite element/boundary element method for the unified radiation and scattering analysis of general infinite periodic arrays", *IEEE Trans. Antennas and Propag.*, vol. 43, no. 2; February 1995; pp. 145-153.

[64] X.-Q. Sheng, J.-M. Jin, J. Song, C.-C. Lu and W. C. Chew; "On the formulation of hybrid finite-element and boundary-integral methods for 3-D scattering"; *IEEE Trans. on Antennas and Propag.*, vol. 46, no. 3; March 1998; pp. 303-311.

[65] Thomas F. Eibert and John L. Volakis; "Adaptive integral method for hybrid FE/BI modelling of 3-D doubly periodic structures"; *IEE Proc. Microwaves, Antennas and Propag.*, vol. 146, no. 1; February 1999; pp. 17-22.

[66] Thomas F. Eibert, John L. Volakis, Donald R. Wilton and David R. Jackson; "Hybrid FE/BI modeling of 3-D doubly periodic structures utilizing triangular prismatic elements and an MPIE formulation accelerated by the Ewald transformation"; *IEEE Trans. Antennas and Propag.*, vol. 47, no. 5; May 1999; pp. 843-850.

[67] Thomas F. Eibert and Volkert W. Hansen; "Comments on 'On the formulation of hybrid finite-element and boundary-integral methods for 3-D scattering' "; *IEEE Trans. on Antennas and Propag.*, vol. 48, no. 1; January 2000; pp. 129-130.

[68] Dejan S. Filipovic, Lars S. Anderson and John L. Volakis; "A multiresolution method for simulating infinite periodic arrays"; *IEEE Trans. on Antennas and Propag.*, vol. 48, no. 11; November 2000; pp. 1784-1786.

[69] Jeffrey A. Reed and Dale M. Byrne; "Frequency-selective surfaces with multiple apertures within a periodic cell", *J. Opt. Soc. Am. A*, vol. 15, no. 3; March 1998; pp. 660-668.

[70] Maurizio Bozzi and Luca Perregrini; "Analysis of FSS with multiple, arbitrarily shaped elements within a periodic cell", *2000 IEEE Antennas and Propag. Society International Symp.*, vol. 2, Salt Lake City, UT; July 2000; pp. 838-841.

[71] G. Conciauro, M. Guglielmi and R. Sorrentino; *Advanced Modal Analysis: CAD Techniques for Waveguide Components and Filters*; John Wiley and Sons, Ltd., Chichester, England; 2000.

[72] Jafar Shaker; "Analysis of multilayer double periodic structures and their performance"; *Ph. D. Thesis*; University of Manitoba, Winnipeg, Manitoba; April 1995.

[73] Jose A. Encinar and J. Agustin Zornoza; "Design and development of multilayer printed reflectarrays for dual polarisation and bandwidth enhancement"; *ESA SP-444: Millennium Conf. on Antennas and Propag. (AP 2000)*, Davos, Switzerland; April 2000; Paper no. 0236.

[74] D. M. Pozar, S. D. Targonski and R. Pokuls; "A shaped-beam microstrip patch reflectarray"; *IEEE Trans. on Antennas and Propag.*, vol. 47, no. 7; July 1999; pp. 1167-1173.

[75] K. Y. Sze and L. Shafai; "Reflection properties of infinite periodic arrays of perfectly conducting plates"; *1996 Symposium on Antenna Technology and Applied Electromagnetics (ANTEM '96)*, Montreal, Quebec, August 1996; pp. 781-784.

[76] K. Y. Sze and L. Shafai; "Reflection properties of infinite periodic arrays of rectangular conducting patches"; *Can. J. Elect. and Comp. Eng.*, vol. 24, no. 1; January 1999; pp.27-34.

[77] K. Y. Sze and L. Shafai; "Analysis of infinite periodic patch arrays using entire domain and subdomain basis functions"; *International Wireless and Telecommunications Symposium/Exhibition (IWTS '97)*, vol. 3, Shah Alam, Malaysia, May 1997; pp. 58-63.

[78] K. Y. Sze and L. Shafai; "Numerical convergences of infinite periodic patch arrays using subdomain basis functions"; *IEEE WESCANEX '97 Conference on Communications, Power and Computing*, Winnipeg, Manitoba, May 1997; pp. 252-257.

[79] K. Y. Sze and L. Shafai; "Analysis of phase variation due to varying patch length in a microstrip reflectarray"; *1998 IEEE Antennas and Propag. Society International Symp.*, vol. 2, Atlanta, GA; June 1998; pp. 1134-1137.

[80] K. Y. Sze and L. Shafai; "Phase properties of a variable-patch-size microstrip reflectarray"; *1998 Symp. on Antenna Technology and Applied Electromagnetics (ANTEM '98)*, Ottawa, Canada; August 1998; pp. 551-554.

[81] K. Y. Sze and L. Shafai; "Microstrip patches for a reflectarray"; *1999 IEEE Antennas and Propag. Society International Symp.*, vol. 3, Orlando, FL; July 1999, pp. 1666-1669.

[82] K. Y. Sze and L. Shafai; "Substrate thickness in a microstrip reflectarray"; *1999 Asia Pacific Microwave Conf. (APMC '99)*, vol. 1, Singapore; November/December 1999; pp. 146-149.

[83] K. Y. Sze and L. Shafai; "Reflectarray phase errors due to finite patch size"; *2000 Symp. on Antenna Technology and Applied Electromagnetics (ANTEM 2000)*, Winnipeg, Canada; August 2000; pp. 205-208.

[84] K. Y. Sze and L. Shafai; "Some concepts for a line-source-fed microstrip reflectarray"; *2000 Symp. on Antenna Technology and Applied Electromagnetics (ANTEM 2000)*, Winnipeg, Canada; August 2000; pp. 295-298.

[85] K. Y. Sze and L. Shafai; "Reflection phase properties and microstrip reflectarray performance"; *2000 Symp. on Antenna Technology and Applied Electromagnetics (ANTEM 2000)*, Winnipeg, Canada; August 2000; pp. 303-306.

[86] K. Y. Sze and L. Shafai; "A formulation for reflection coefficient phase of an infinite periodic array of microstrip patches"; *Electronics Lett.*, vol. 37, no. 3; February 2001; pp. 142-143.

[87] Roger F. Harrington; *Field Computation by Moment Methods*; Robert E. Krieger Publishing Company, Malabar, Florida; 1968.

[88] F. S. Johansson; "Convergence phenomenon in the solution of dichroic scattering problems by Galerkin's method"; *IEE Proc. Pt. H*, vol. 134, no. 1; February 1987; pp. 87-92.

[89] M. Leroy; "On the convergence of numerical results in modal analysis", *IEEE Trans. Antennas and Propag.*, vol. AP-31, no. 4; July 1983; pp. 655-659.

[90] Raj Mittra, Tatsuo Itoh and Ti-Shu Li; "Analytical and numerical studies of the relative convergence phenomenon arising in the solution of an integral equation by the moment method"; *IEEE Trans. Microwave Theory and Techn.*, vol. MTT-20, no. 2; February 1972; pp. 96-104.

[91] James P. Montgomery; "Scattering by an infinite periodic array of microstrip elements"; *IEEE Trans. on Antennas and Propag.*, vol. AP-26, no. 6; November 1978; pp. 850- 854.

[92] David K. Cheng; *Field and Wave Electromagnetics*, 2nd. ed.; Addison-Wesley Publishing Company, Inc., Reading, MA; 1989.

[93] Xian Hua Yang; "A study of multilayer printed transmission lines and antennas"; *Ph.D. Thesis*; University of Manitoba, Winnipeg, Manitoba; January 1994.

[94] Samuel Silver, ed.; *Microwave Antenna Theory and Design*; Boston Technical Lithographers, Inc., Lexington, MA; 1963.

[95] Ashley W. Robinson, Marek E. Bialkowski and Hyok J. Song; "An X-band passive reflect-array using dual-feed aperture-coupled patch antennas"; *1999 Asia Pacific Microwave Conf. (APMC '99)*, vol. 3, Singapore; November/December 1999; pp. 906-909.

[96] *Zeland IE3D* is a trademark of Zeland Software, Inc., Fremont, CA.

[97] Hervé Legay and Lotfollah Shafai; "Parametric analysis of an EMC patch surrounded by parasitic elements"; *Archiv Electron. Übertragungstech (AEÜ)*, vol. 48, no. 4; 1994; pp. 184-190.

[98] C. K. Aanandan, P. Mohanan and K. G. Nair; "Broad-band gap coupled microstrip antenna"; *IEEE Trans. Antennas and Propag.*, vol. 38, no. 10; October 1990; pp. 1581-1586.

[99] M. Clenet and L. Shafai; "Wideband single layer microstrip array at 28 GHz"; *1999 IEEE Antennas and Propag. Society International Symp.*, vol. 3, Orlando, FL; July 1999, pp. 2106-2109.

[100] Robert J. Mailloux; *Phased Array Antenna Handbook*; Artech House, Norwood, MA; 1994.

[101] T. A. Metzler; "Stub loaded microstrip reflectarrays"; *1995 IEEE Antennas and Propag. Society International Symp.*, vol. 1; June 1995; pp. 574-577.

[102] Constantine A. Balanis; *Advanced Engineering Electromagnetics*; John Wiley and Sons, New York; 1989.

[103] David D. Morabito; "The characterization of a 34-meter beam-waveguide antenna at Ka band (32.0 GHz) and X band (8.4 GHz)"; *IEEE Antennas and Propag. Mag.*, vol. 41, no. 4; August 1999; pp. 23-34.

[104] Jafar Shaker, Corey Pike and Michel Cuhaci; "A dual orthogonal cassegrain flat reflector for Ka-band application", *Microwave and Optical Technology Lett.*, vol. 24, no. 1; February 2000; pp. 7-11.

[105] Barry Wilkinson and Michael Allen; *Parallel Programming: Techniques and Applications Using Networked Workstations and Parallel Computers*; Prentice-Hall, Upper Saddle River, NJ; 1999